Highly scalable femtosecond coherent beam combining system of high power fiber amplifiers

Anke Heilmann

université PARIS-SACLAY

NNT : 2018SACLX112

Highly Scalable Femtosecond Coherent Beam Combining System of High Power Fiber Amplifiers

Thèse de doctorat de l'Université Paris-Saclay
préparée à l'Ecole Polytechnique

École doctorale n°572 : ondes et matières (EDOM)
Spécialité de doctorat: optique et photonique

Thèse présentée et soutenue à Palaiseau, le 18/12/2018, par

Anke Heilmann

Composition du Jury :

Gérard Mourou Professeur, Ecole Polytechnique (IZEST)	Président
Agnès Desfarges-Berthelemot Professeur, Université de Limoges (XLIM)	Rapporteur
Aurélie Jullien Chargée de recherches, Université Côte d'Azur (IPN)	Rapporteur
Marc Hanna Chargé de recherches, IOGS (LCF)	Examinateur
Arnaud Brignon Responsable de laboratoire, Thales (TRT)	Examinateur
Louis Daniault Ingénieur de recherche, Ecole Polytechnique (LULI)	Examinateur
Jean-Christophe Chanteloup Chargé de recherches, Ecole Polytechnique (LULI)	Directeur de thèse
Philippe Adam Ingénieur, DGA (MRIS)	Invité

Thèse de doctorat

Acknowledgments

I am very lucky that I have been given the opportunity to perform my PhD studies on a cutting-edge research project at one of the most renowned educational institutions of France.

Within the more than three years which I spent on the XCAN project at the Ecole Polytechnique, I saw, heard and learned a lot, not only about physics, but also for life. I am highly grateful to everybody who took part in this experience, and in particular I would like to thank

- Jean-Christophe Chanteloup, my thesis' advisor, who first off all accepted me as his PhD student. I highly appreciated his constant availability and the help he provided on any kind of question, in particular when it came to dealing with French administration. Also, he gave me the opportunity to travel to Japan and the USA, two journeys which were highly enjoyable not only from a professional, but also from a personal point of view.

- Louis Daniault, my co-advisor, who gave me countless private lessons on everything related to femtosecond lasers, fiber amplifiers and coherent beam combining. He never got tired of answering my endless questions, and I prefer not to imagine what our laser system would look like without his expertise.

- Gérard Mourou, who initiated the XCAN project and who gave me the honor of presiding over my thesis defense.

- Agnès Desfarges-Berthelemot and Aurélie Jullien, who accepted to be the rapporteurs of this thesis, provided valuable comments on the initial manuscript, and who traveled through have France for attending my thesis defense.

- Marc Hanna and Arnaud Brignon, who accepted to be examiners at my thesis defense. They traveled less far, but still carefully read the more than 100 pages of this thesis.

- Philippe Adam from the Direction générale de l'armement (DGA, French ministry of defense), for being part of the jury of this thesis. Also, I'd like to thank the DGA for financially supporting my work.

- Ihsan Fsaifes and Séverine Bellanger, the other members of the XCAN team at the Ecole Polytechnique, for taking their part in the project and always advancing the work, and for providing an additional pair of hands whenever needed.

- Marie Antier, Jérémy Le Dortz, Jérôme Bourderionnet, Arnaud Brignon, Christian Larat, Eric Lallier and Christophe Simon-Boisson, who are part of the XCAN team at Thales TRT

and Thales LAS France, who provided the phase matching devices and willingly shared their experience in all questions related to coherent beam combining.

- The LULI lab, where our project was hosted. In spite of the delicate political situation, I always felt welcome at the lab, and took great pleasure in participating in numerous barbecues, three soccer tournaments and a sailing regatta.
- My family and friends, for their never-ending support, encouragements and understanding.
- My boyfriend, for choosing me as his girlfriend and sticking to me throughout everything it takes to finish a PhD thesis.

Contents

Introduction

Ultrafast lasers are nowadays used in a wide range of disciplines such as material processing, medical treatments, microscopic imaging and fundamental science [1, 2]. Most of these applications make use of the high peak powers and intensities which can be obtained when a femtosecond laser pulse is strongly focused.

For instance, in material processing applications such as laser drilling, the energy of the laser pulse can be used to vaporize material so that a hole is created. The advantage of using femtosecond pulses for this process is that due to the short pulse duration the energy transfer to the surrounding material is largely suppressed. Hence, very clean and neat holes can be obtained [3].

The same principle applies to laser-based surgery, where the energy of the focused laser is used to create very neat and accurate cuts. Thanks to the short pulse duration, the surrounding tissue remains largely undamaged, which has a positive impact on the subsequent healing processes. Moreover, as some organic tissues such as the human eye are transparent to certain wavelengths, the laser can be focused to deeper layers of the tissue. Thus, these layers can be treated while the rest of the tissue remains intact [4].

Several nonlinear microscopy techniques make use of the high intensities obtained when a femtosecond laser pulse is strongly focused in the interior of a sample. In this case, the material is not destroyed as in the previous examples, but a nonlinear process such as two-photon fluorescence is excited. By scanning the position of the focal spot in all three spatial dimensions, a three-dimensional picture of the sample can be obtained [5].

Last but not least, femtosecond lasers are used in different areas of fundamental science, for instance in ultrafast spectroscopy techniques [6] or for the generation of frequency combs for high precision metrology experiments [7]. Another point of interest is the use of secondary sources, that is, the generation of radiation based on the interaction of a light pulse with matter. Examples include the generation of coherent light at wavelengths not accessible with classical lasers. For instance, high harmonic generation makes use of the very high peak power of femtosecond pulses to generate extremely short laser pulse bursts in the extreme ultraviolet (EUV) or soft-X-ray wavelength region [8]. In contrast, coherent light in the terahertz regime can be obtained i.e. by optical rectification of the femtosecond pulses in a second order nonlinear crystal [9]. Such coherent light sources can be used in a variety of research fields ranging from the fundamental understanding of atom or molecule dynamics to exploring spectroscopic imaging methods operating in the range of the newly generated wavelengths.

It is also possible to generate high energy electron beams via laser wakefield acceleration, where a plasma wave is created in the wake of the laser pulse. The strong electric fields associated with this wave can then be used to accelerate previously injected electron beams to very high energies.

Besides, protons and ions can be accelerated by focusing laser pulses on a foil target, so that charged particles are expelled from this foil and accelerated by the electric fields created when the laser impinges on the target [10].

The peak powers required by some of these applications are typically obtained at the expense of the average power of the laser system in use. However, the different applications would also benefit from an increase in pulse repetition rate at a given peak power. For example, this could decrease the measurement times by increasing the signal-to-noise ratio of microscopic imaging applications which rely on ultrashort pulses provided by a secondary source.

Furthermore, there are other potential applications which are not accessible with the performances of current state-of-the-art ultrafast laser systems. A field of particular interest is particle acceleration, where the advantages of laser-based techniques with respect to conventional accelerators are a better efficiency and a reduced size and, potentially, cost, which could increase the accelerator's availability. However, even the peak powers and pulse repetition rates of state-of-the-art large-scale ultrafast laser facilities are not sufficient to produce particle beams which exhibit an energy and intensity high enough to be used for applications such as cancer therapy or nuclear waste transmutation [11].

Even more ambitious studies investigate the tracking and remediation of space debris with ultrafast lasers. Indeed, the ablation caused by a laser incident on a piece of debris could change its orbit such that it re-enters earth's atmosphere and burns up. However, this would require a laser system operating in the kilohertz regime and emitting pulse energies of at least some joule [12].

In consequence, there is a large interest in the development of ultrafast laser sources which could deliver both high peak and average powers. Current systems are limited in one of these two parameters due to the architecture in use: typical high peak power laser systems rely on Ti:Sapphire crystals as active laser medium, and are limited in average power and therefore repetition rate due to the heating of the crystal. In contrast, fiber lasers benefit from a very good heat removal thanks to the high surface-to-volume ratio of the fiber and can therefore operate at very high repetition rates. However, as the light is confined in the small core of the fiber, the beam reaches very high intensities. Due to the long interaction lengths within the fiber, this favors the occurrence of nonlinear effects. These can in the worst case damage the fiber itself and set thus a limit to the accessible peak powers.

There are several techniques to mitigate these problems by reducing the peak power of the beam in the fiber. The most famous one is chirped pulse amplification (CPA, [13]), which consists in the temporal stretching of the pulses prior to amplification, and the subsequent recompression of the amplified pulses. This technique is nowadays routinely used in ultrafast laser systems and has allowed to increase the available peak powers by several orders of magnitude. Another option is the use of so-called large mode area fibers, whose core diameters are increased with respect to the ones of standard fibers.

However, current state-of-the-art ultrafast fiber laser systems already use the maximum peak power scaling capabilities of both of these techniques, so that new approaches need to be explored in order to allow for a further increase of peak power.

A method which has been proven to be well suited for such a power scaling is coherent beam combining (CBC, [14]). In this technique, the laser beam is spatially split into N sub-beams, each of which gets amplified independently. Afterwards, the sub-beams are coherently superposed in order to form one very powerful combined beam. If this combination shall be efficient, the spatial and spectral amplitudes and phases of all sub-beams need to be exactly matched. In this way, both the peak and the average power of the combined beam can theoretically be scaled by a factor of N with respect to what would have been possible if only a single amplifier was used.

This approach is particularly well suited for the implementation on fiber lasers, since their waveguiding properties guarantee a repeatable and very high spatial beam quality. Indeed, already the coherent combination of a moderate number of fibers has allowed to increase both the peak and average power of ultrafast fiber laser systems to new records of 35 GW and 1.83 kW, respectively [15, 16]. Furthermore, such systems have been shown to be suitable for high harmonic generation and subsequent fundamental science experiments and EUV imaging techniques [17, 18].

However, in order to access applications such as particle acceleration, the coherent combination of up to 10 000 fibers has to be considered [19]. Hence, the scalability of CBC system becomes a question of interest. Within this framework, recent calculations have shown that the phase matching of up to 10 000 parallel channels is feasible with off-the-shelf technical equipment [20].

In order to implement a first proof-of-principle demonstration of a highly scalable CBC setup, the XCAN project, a collaboration between the Ecole Polytechnique, Thales TRT and Thales LAS France SAS, has been initiated. It consists of three main points: first, the implementation of a 19-fiber low power setup in order to investigate the applicability of the aforementioned phase matching technique in the femtosecond regime [21]. Second, the setup of a seven fiber amplifier test system which is needed to analyze the impact of the amplification and the onset of nonlinear effects on both the phase matching algorithm and the characteristics of the combined beam. And finally, the CBC of 61 fiber amplifiers in order to confirm the scalability of the previously demonstrated concepts to a considerably increased number of channels. This final demonstrator is meant to deliver an average power of 750 W, at a repetition rate of 200 kHz and a pulse duration of ~ 220 fs, corresponding to a peak power of 15 GW and a pulse energy of 3.5 mJ.

In this thesis, the work performed on the second of these three points, that is, the seven fiber amplifier setup, will be presented. In a first chapter, the physical and technological fundamentals which are the basis of the laser system will be discussed. Afterwards, the principle of coherent beam combining will be explained, thus motivating our choice for a specific system architecture. In the third chapter, numerical simulations will be presented which allowed to estimate the maximum tolerable mismatches between the spatial and spectral properties of the different channels of our setup, and which played therefore an important role in the dimensioning of our laser system. In the last chapter, a complete description of the implementation of the seven fiber setup will be given, and it will be characterized both under linear and nonlinear operating conditions.

1 Fundamentals

This chapter provides an overview of the physical principles and technological developments which are the basis of this thesis. In a first section, the spatial and spectral characteristics of femtosecond laser pulses are presented. Afterwards, a short overview of optical fiber technology is provided, thus introducing the different types of fibers used in our experimental setup. Finally, the amplification of femtosecond pulses with Yb-doped fiber amplifiers is discussed.

1.1 Femtosecond Laser Beams

An intuitive picture of a train of (femtosecond) laser pulses is shown in fig. 1.1. Ultrashort pulses are emitted at a repetition rate $\nu = 1/T$ and each pulse contains a certain energy $\mathcal{E}$. The pulse duration Δt is given by the intensity full width half maximum (FWHM) of the temporal pulse profile. These parameters allow to define two characteristic powers of a pulsed laser, which are the peak power $P_{\text{peak}} = \frac{\mathcal{E}}{\Delta t}$ and the average power $P_{\text{av}} = \frac{\mathcal{E}}{T}$.

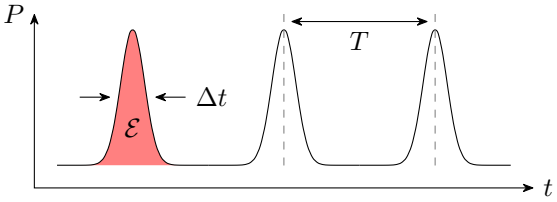

Figure 1.1: Illustration of a laser pulse train with characteristic timescales.

In the following, a more rigorous mathematical description of femtosecond laser pulses will be given. At first, the laser beam is considered in free space without dispersion, so that its spatial and temporal characteristics can be treated independently. Afterwards, the propagation in an optical fiber will be described. In this case, the spatial beam profile is imposed by the waveguide structure of the fiber, whereas the propagation in the fiber medium can induce changes to the temporal and spectral shape of the pulse.

1.1.1 Femtosecond Pulses in Free Space

Spatial Characteristics

The spatial part of the laser beam can in principal have any shape and characteristics whichever. However, in our setup, most of the beams are given as the fundamental mode of an optical fiber, and are therefore well approximated by a Gaussian beam [22], schematically shown in fig. 1.2 and mathematically described by

$$E_{\text{Gaussian}}(x,y,z) = E_0 \frac{w_0}{w(z)} \exp\left(-\frac{x^2+y^2}{w(z)^2}\right) \exp\left(-i\left(kz + k\frac{x^2+y^2}{2R(z)} - \psi(z)\right)\right). \tag{1.1}$$

In this expression, $k = \frac{2\pi}{\lambda_0}$ is the wavenumber, λ_0 the central wavelength and w denotes the radius of the beam, defined as the radial distance between the optical axis and the point where the intensity has dropped to $1/e^2$ of its on-axis value. w_0 is the minimum radius or waist of the beam. Using this waist, it is possible to define the so-called Rayleigh range z_R of the beam as $z_R = \frac{\pi w_0^2}{\lambda_0}$. It indicates the distance at which the beam radius has increased to $\sqrt{2}$ times its initial value. In a general way, the beam width evolves with z according to $w(z) = w_0\sqrt{1+\left(\frac{z}{z_R}\right)^2}$. For $z \gg z_R$ this simplifies to $w(z) = w_0 z/z_R$, so that the angle of divergence θ is given by $\theta = \frac{w(z)}{z} = \frac{\lambda_0}{\pi w_0} = \frac{w_0}{z_R}$. Finally, $R(z)$ is the radius of curvature of the wavefronts and $\psi(z)$ is the Gouy phase. Both are included here for completeness and will not be of further interest within the framework of this thesis.

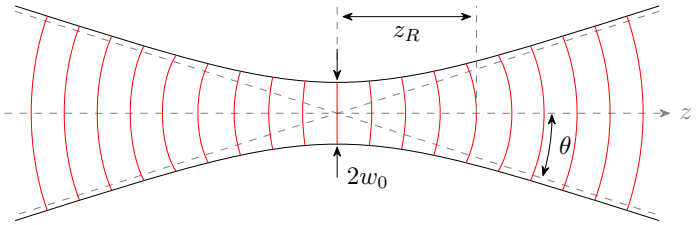

Figure 1.2: Schematic of a Gaussian beam.

Beam Quality Factor M^2

As indicated above, the Gaussian beam is only an approximation of any real beam. Moreover, a laser beam can take other shapes, which are much less well described by a Gaussian beam. For instance, in our setup the intensity profile of the spatially filtered combined beam is given by an Airy pattern clipped at the first zero, and with a different filtering configuration even a donut-shaped beam could be created (see section 2.2.1 and section 4.5.4 for more detail). It is therefore necessary to introduce a criterion applicable to arbitrary beam shapes which evaluates the spatial quality of the beam in question. This is usually done via the beam quality factor M^2, defined as the ratio of the products of waist w_0 and divergence θ of the experimental beam and an ideal Gaussian one. Hence, for a Gaussian beam, $M^2 = 1$. In practice, the closer the measured M^2 gets to one, the more the experimental beam resembles a Gaussian one.

The beam width can be evaluated in different ways. One of the simplest methods is certainly the $1/e^2$-definition given above. However, this approach is inaccurate in a sense that it does not take into account the exact shape of the beam, so that the width of a Gaussian beam could be the same as that of a top-hat one, if they have the same radius at $1/e^2$, as illustrated in fig. 1.3. Therefore, the width of arbitrarily shaped beams is better evaluated by using the 4σ- or second moment method, which weights the beam intensity with respect to its distance from the beam

center. The beam diameter in x-direction d_x is then defined as

$$d_x = 4\sqrt{\frac{\iint I(x,y)(x-\bar{x})^2\,dx\,dy}{\iint I(x,y)\,dx\,dy}}, \tag{1.2}$$

where $I(x,y)$ is the intensity distribution of the field and $\bar{x}$ is its centroid along the x-direction. The diameter in y-direction can be found analogously. The beam diameter is thus defined as four times the standard deviation of the intensity profile. For a Gaussian beam, this diameter and the $1/e^2$ one are equivalent.

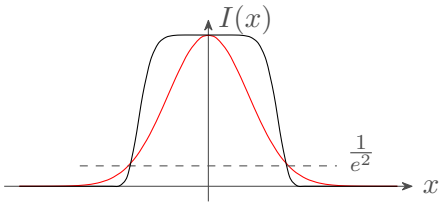

Figure 1.3: A Gaussian (red) and a top-hat (black) beam with the same $1/e^2$ beam width.

Temporal Characteristics

Since the time and the frequency domain are related via a Fourier transform, short pulses necessarily exhibit a broad spectrum. If this spectrum is given by $E(\omega)$, then the temporal shape of the pulse can be found by

$$E(t) = \mathcal{F}[E(\omega)] = \frac{1}{\sqrt{2\pi}}\int E(\omega)e^{-i\omega t}\,d\omega\,. \tag{1.3}$$

Hence, the pulse profile in the time domain can also be understood as an infinite sum of plane waves oscillating each at a frequency ω and having a complex spectral amplitude $E(\omega)$. Provided that all these plane waves are in phase at a certain time t_0, their constructive interference leads to the creation of ultrashort pulses.

In a general way, $E(\omega)$ can be expressed via a real-valued envelope centered around a central frequency ω_0 and a spectral phase, so that $E(\omega) = A(\omega-\omega_0)e^{i\varphi(\omega)}$. In the simplest case, $\varphi(\omega) = 0$, which means that the temporal pulse shape is simply given by a Fourier transform of the spectral envelope, $E(t) = \mathcal{F}[A(\omega-\omega_0)]$. The shift of the amplitude by ω_0 in the frequency domain leads to an additional phase in the time domain, as can be shown by using the substitution $\Delta\omega = \omega - \omega_0$,

$$E(t) = \frac{1}{\sqrt{2\pi}}e^{-i\omega_0 t}\int A(\Delta\omega)e^{-i\Delta\omega t}\,d\Delta\omega = e^{-i\omega_0 t}\mathcal{F}[A(\Delta\omega)]. \tag{1.4}$$

In the time domain, the shape of the pulse is thus given by the Fourier transform of its spectral envelope, which is modulated by a carrier plane wave of frequency ω_0. It should be noted that the maximum of the temporal envelope coincides with a maximum of the carrier wave, as illustrated in fig. 1.4a.

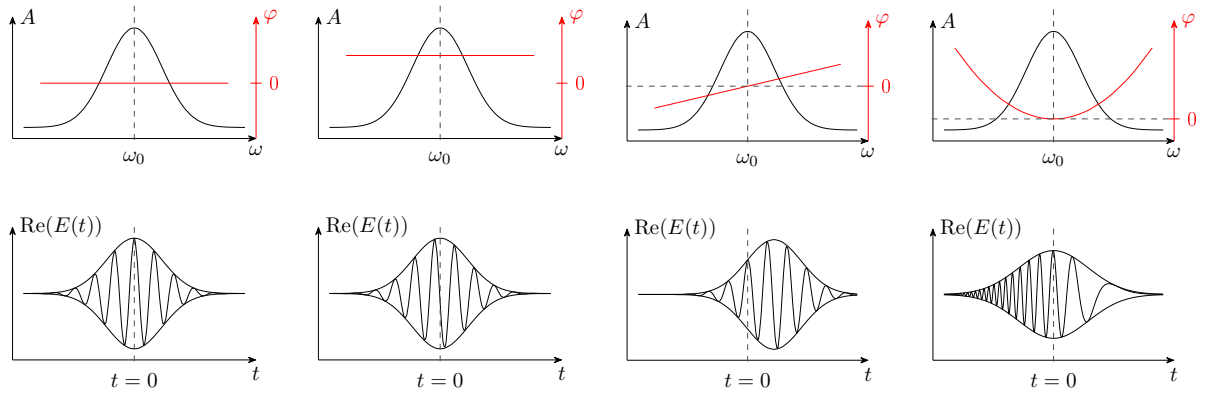

(a) No spectral phase. (b) Phase offset φ_0. (c) Delay φ_1. (d) Frequency chirp φ_2.

Figure 1.4: Influence of different components of the spectral phase on the electric field in the time domain.

Spectral Phase

In a next step, the spectral phase is added to the spectral envelope, so that $E(\omega) = A(\Delta\omega)e^{i\varphi(\omega)}$. Since the width of the spectrum is typically small compared to its central frequency, the phase can be developed in a Taylor series, yielding $\varphi(\omega) = \varphi_0 + \varphi_1(\omega - \omega_0) + \frac{\varphi_2}{2}(\omega-\omega_0)^2 + \frac{\varphi_3}{6}(\omega-\omega_0)^3 + \mathcal{O}(\omega-\omega_0)^4$. Using this approach, it is possible to study the influence of each part of the spectral phase independently from the others [23].

Adding the constant part φ_0, the field in the frequency domain becomes $E(\omega) = A(\Delta\omega)e^{i\varphi_0}$. Since φ_0 does not depend on ω, it translates directly into the time domain without being modified by the Fourier transform. Hence, the temporal field reads

$$E(t) = e^{i\varphi_0}e^{-i\omega_0 t}\mathcal{F}[A(\Delta\omega)]. \tag{1.5}$$

The carrier plane wave gets thus shifted by the phase offset φ_0 with respect to the envelope, so that the maximum of the envelope does no longer coincide with one of the maxima of the carrier wave, as shown in 1.4b. This phase mismatch is called carrier-envelope phase.

In the context of coherent beam combining, the phase offsets φ_0 of all the emitters need to be matched. In the presence of carrier-envelope phases, such a matching can give rise to slight mismatches in the positions of the pulse envelopes. However, this is not critical as long as the pulse duration is much larger than a few cycles of the carrier wave. Since this is the case within the framework of this thesis, carrier-envelope phases will not have any further impact.

A phase φ_1 which varies linearly with the frequency will result in a delay of the pulse, as can be shown by a simple calculation,

$$\begin{aligned} E(t) &= \frac{1}{\sqrt{2\pi}}e^{-i\omega_0 t}\int A(\Delta\omega)e^{i\varphi_1\Delta\omega}e^{-i\Delta\omega t}\,d\Delta\omega \\ &= \frac{1}{\sqrt{2\pi}}e^{-i\omega_0 t}\int A(\Delta\omega)e^{-i(t-\varphi_1)\Delta\omega}\,d\Delta\omega = e^{-i\omega_0 t}\mathcal{F}[A(\Delta\omega)][t-\varphi_1]. \end{aligned} \tag{1.6}$$

A spectral phase of first order results thus in a shift of the pulses by φ_1 in the time domain. However, only the temporal envelope gets shifted, while the carrier wave remains at its initial position with a maximum at $t = 0$. As this or any other maximum of the carrier wave does not necessarily coincide with the new position of the envelope maximum, a first order spectral phase generally introduces an additional carrier-envelope phase, as illustrated in fig. 1.4c.

Mathematically, this can be described by substituting $t' = t - \varphi_1$, so that the time axis is centered around the maximum of the spectral envelope. This yields

$$E(t') = e^{-i\omega_0 t'} e^{-i\omega_0 \varphi_1} \mathcal{F}[A(\Delta\omega)][t'] \tag{1.7}$$

and shows that the carrier wave gains an additional phase offset $\varphi_0 = -\omega_0\varphi_1$. Hence, if a constant phase $\varphi_0 = \omega_0\varphi_1$ is applied at the same time as φ_1, both the carrier wave and the spectral envelope are subject to the same delay, and no carrier-envelope phase is acquired. This is referred to as pure delay and requires that a spectral phase $\varphi = \varphi_1\Delta\omega + \varphi_1\omega_0 = \varphi_1\omega$ is added to the envelope. As will be seen below, such a phase is automatically applied when the pulse propagates in a non-dispersive medium.

A spectral phase of second order induces a frequency chirp and results in a temporal broadening of the pulse. This can be understood in terms of the group delay $\tau_g = \frac{d\varphi}{d\omega}$, which describes the delay accumulated by a frequency ω after propagation of a distance z. Since a second order spectral phase leads to a linear group delay $\tau_g = \varphi_2(\omega - \omega_0)$, the frequencies will arrive one after the other, so that the pulse undergoes a linear spectral chirp and a temporal broadening. For large φ_2, this behavior results in temporal phase and pulse profiles which are identical to the spectral ones.

The analytical expression of the temporal pulse profile depends in this case on its exact spectral shape. In order to give an instructive example, we will focus here on a pulse with a Gaussian spectral amplitude of width $\delta\omega$ centered around ω_0, $A(\Delta\omega) = A_0 \exp\left(-\frac{(\Delta\omega)^2}{2\delta\omega^2}\right)$. For comparison, the temporal shape of a Gaussian spectrum without a spectral phase is given by

$$\begin{aligned} E(t) = \mathcal{F}[A(\Delta\omega)] &= \frac{1}{\sqrt{2\pi}} A_0 \exp(-i\omega_0 t) \int \exp\left(-\frac{\Delta\omega^2}{2\delta\omega^2}\right) \exp(-i\Delta\omega t)\, d\Delta\omega \\ &= \frac{1}{\sqrt{2\pi}} \delta\omega A_0 \exp(-i\omega_0 t) \exp\left(-\frac{t^2}{2\delta t^2}\right), \end{aligned} \tag{1.8}$$

where $\delta t = 1/\delta\omega$. Adding the second order spectral phase $\varphi(\omega) = \frac{\varphi_2}{2}\Delta\omega^2$ yields then

$$\begin{aligned} E(t) &= \frac{1}{\sqrt{2\pi}} A_0 \exp(-i\omega_0 t) \int \exp\left(-\frac{\Delta\omega^2}{2\delta\omega^2}\right) \exp\left(i\frac{\varphi_2}{2}\Delta\omega^2\right) \exp(-i\Delta\omega t)\, d\Delta\omega \\ &= \frac{1}{\sqrt{2\pi}} \frac{\delta\omega}{\sqrt{C}} A_0 \exp(-i\omega_0 t) \exp\left(-\frac{t^2}{2(C\delta t)^2}\right) \exp\left(-i\varphi_2 \frac{t^2}{2C^2\delta t^4}\right), \end{aligned} \tag{1.9}$$

with the chirp parameter $C^2 = 1 + \frac{{\varphi_2}^2}{\delta t^4} \approx \frac{\varphi_2^2}{\delta t^4}$, where the approximation holds for $\varphi_2 \gg \delta t^2$. The Gaussian envelope gets thus broadened by a factor C. In the same time, its amplitude is reduced by $1/\sqrt{C}$, so that the energy conservation is still observed.

The frequency chirp postulated earlier can be confirmed by considering the instantaneous frequency $\omega(t)$, given by

$$\omega(t) = -\frac{d\varphi(t)}{dt} = -\frac{d}{dt}\left(-\varphi_2 \frac{t^2}{2C^2\delta t^4} - \omega_0 t\right) = \varphi_2 \frac{t}{C^2\delta t^4} + \omega_0 \approx \frac{t}{\varphi_2} + \omega_0, \tag{1.10}$$

where again the approximation holds for $\varphi_2 \gg \delta t^2$. The instantaneous frequency increases thus linearly with time, leading to a frequency chirp as depicted in fig. 1.4d. Moreover, at the point in time where the intensity of the chirped pulse has dropped to $1/e$ of its maximum value, $t' = C\delta t = \frac{\varphi_2}{\delta t}$, the instantaneous frequency is given by $\omega(t') = \frac{1}{\delta t} + \omega_0 = \delta\omega + \omega_0$, corresponding exactly to the point where the intensity of the frequency spectrum has dropped to $1/e$. Since the frequency chirp is linear in time and centered around $\omega(0) = \omega_0$, this direct correspondence is maintained for any other pairs of t' and ω. This confirms the homothetic behavior between the time and frequency domain described above.

A spectral phase of third order (TOD, third order dispersion) gives rise to a quadratic group delay, so that the central frequency arrives first (or last, depending on the sign of φ_3), while the other frequencies arrive later (earlier) in pairs of two. This leads to an oscillatory behavior in the time domain, so that the main pulse is followed (preceded) by several weaker post- (pre-) pulses. An analytical treatment of this case is possible for Gaussian pulses [24], but beyond the scope of this thesis. Moreover, it will be seen in section 3.4.2 that the impact of TOD on the coherent combining efficiency is very small.

Time-bandwidth Product

A common means to characterize the temporal and spectral quality of an ultrashort pulse is the time-bandwidth product, given as the product of the FWHM of the intensity spectrum $\Delta\nu$ and the temporal pulse profile Δt. In the ideal case, the pulse is Fourier transform limited or time-bandwidth limited, which means that the time-bandwidth product is minimized. This minimum value is calculated based on the measured spectrum, which is then Fourier transformed in order to access the theoretical temporal profile and its FWHM. However, due to spectral phases the actual experimental pulse width might be larger than the calculated one. Hence, the time-bandwidth product based on the measured pulse width is in general larger than the one based on the calculation, and indicates how close the pulse is to the ideal transform limited case.

Pulse Propagation in Free Space

On the optical axis and by neglecting the Gouy phase, the spatial phase of a Gaussian beam is given by $\varphi = kz$. Hence, after propagating a distance z, the beam has accumulated a phase $\varphi = kz$. In free space and if dispersion can be neglected, $k = n_0\omega/c$, where n_0 is the refractive index of air. Thus, after propagation of a distance z, the temporal profile of the pulse becomes

$$
\begin{aligned}
E(t) &= \frac{1}{\sqrt{2\pi}} \int E(\omega) e^{-i\omega t} e^{i\omega \frac{n_0}{c} z} \, d\omega \\
&= \frac{1}{\sqrt{2\pi}} e^{-i\omega_0 t} e^{i\omega_0 \frac{n_0}{c} z} \int A(\Delta\omega) e^{-i\Delta\omega \left(t - \frac{n_0}{c} z\right)} \, d\Delta\omega \, .
\end{aligned}
\tag{1.11}
$$

The pulse envelope gets thus shifted to a time $t'_{\varphi_1} = t - \frac{n_0}{c} z$. At the same time, the carrier wave acquires an additional phase $\omega_0 \frac{n_0}{c} z$, so that it reaches its maximum at $t'_{\varphi_0} = t - \frac{n_0}{c} z$. Given that $t'_{\varphi_1} = t'_{\varphi_0} = t'$, both the carrier wave and the envelope propagate at the same velocity $v_\varphi = c/n_0$, and no carrier-envelope phase is generated. Besides, by identifying $\varphi_1 = \frac{n_0}{c} z$ one sees that the overall phase applied to the pulse becomes $\varphi = \omega_0 \varphi_1 + \varphi_1 \Delta\omega = \varphi_1 \omega$, which corresponds to the pure delay introduced above.

By traveling a certain distance in a dispersion-free medium, the pulse get thus shifted to a time t', but remains otherwise unchanged, as expected. As will be seen in the next section, this behavior changes dramatically when it comes to propagation in a dispersive medium, such as an optical fiber.

1.1.2 Femtosecond Pulses in Optical Fibers

Spatial Considerations

In an optical fiber, the light is guided due to total internal reflection at the boundary of the fiber core and cladding (for more details on optical fibers, see section 1.2). In the fiber, the superposition of the reflected waves forms transversal standing waves, the so-called linearly polarized modes LP of the fiber. As every single wave is superposed with its own reflection, the radial components of their wavevectors cancel out, and the resulting modes propagate in z-direction according to the propagation constant β_{LP}, given by the z-component of the respective wavevectors. Hence, the phase accumulated by a given mode LP after propagation of a distance z in the fiber is simply given by $\varphi = \beta_{\mathrm{LP}} z$, and is constant along the transverse beam profile. In a single mode fiber, this profile can be approximated by a Gaussian beam of width w, where w depends on the fiber parameters [22]. Furthermore, as only the lowest order mode LP_{01} can propagate in such a fiber, β_{LP} can be replaced by β.

Dispersion

Due to the dispersive character of the fiber medium, its refractive index n depends on the wavelength, so that $n = n(\omega)$ and therefore also $\beta = \beta(\omega)$. In order to take into account the frequency dependence of the propagation constant, β is commonly approximated by a Taylor series, given by $\beta(\Delta\omega) = \beta_0 + \beta_1 \Delta\omega + \frac{\beta_2}{2} \Delta\omega^2 + \frac{\beta_3}{6} \Delta\omega^3 + \mathcal{O}(\Delta\omega^4)$. The phase is then recovered by multiplication of $\beta(\Delta\omega)$ with z, so that it is possible to identify each term of βz with one term of the spectral phase discussed in section 1.1.1. This means that the propagation in a dispersive medium gives rise to spectral phases of all orders, leading to the same effects on the temporal pulse shape as described above.

In consequence, a beam which covered a distance z in an optical fiber has gained a phase offset $\beta_0 z = \beta(\omega_0) z = \omega_0 \frac{n_0}{c} z = \frac{\omega_0}{v_\varphi} z$, where $v_\varphi = c/n_0$ is the phase velocity and $n_0 = n(\omega_0)$ the refractive index of the central wavelength in the fiber medium. In the same time, the envelope has accumulated a delay of $\beta_1 z = z \frac{\partial \beta}{\partial \omega}|_{\omega=\omega_0} = \frac{z}{v_g}$, with $v_g = \partial\omega/\partial\beta$ being the group velocity. Since phase and group velocity are generally not the same in a dispersive medium, this will give rise to a carrier-envelope phase.

Furthermore, $\beta_2 z$ can be identified as the group delay dispersion, giving rise to a linear frequency chirp and a temporal pulse broadening as discussed in section 1.1.1 for the spectral phase of second order. β_2 is a material constant given by $\beta_2 \simeq 200\,\mathrm{fs}^2/\mathrm{cm}$ for fused silica at a wavelength of $\lambda = 1030\,\mathrm{nm}$. Finally, $\beta_3 z$ corresponds to a third order spectral phase. Since the material constant $\beta_3 \simeq 410\,\mathrm{fs}^3/\mathrm{cm}$ for fused silica at $\lambda = 1030\,\mathrm{nm}$ is positive, this leads to the creation of post-pulses.

In order to estimate the impact of the dispersion on the final pulse shape, it is convenient to refer to the characteristic length scales associated with the different terms of the wavevector. They are defined as $L_{\mathrm{D},2} = \Delta t^2/\beta_2$ for the group delay dispersion and $L_{\mathrm{D},3} = \Delta t^3/\beta_3$ for the third order dispersion, and are an estimation of the distance which a pulse can propagate in the fiber before the effects of the respective phase become important [25]. In our case, $\Delta t \approx 225\,\mathrm{fs}$, so that $L_{\mathrm{D},2} \approx 2.5\,\mathrm{m}$ and $L_{\mathrm{D},3} \approx 280\,\mathrm{m}$. Considering that the front end of our laser system (cf. section 4.1) consists of about 90 m of fiber per channel, the contribution of the third order dispersion is negligible. In contrast, a second order phase of $\varphi_2 = \beta_2 z \approx 1.8 \times 10^6\,\mathrm{fs}^2$ will be accumulated due to the group delay dispersion. However, at the beginning of the chain, the pulses are temporally stretched by a factor of about 2000, which corresponds to a spectral phase of $\varphi_2 \approx C\delta t^2 = 36 \times 10^6\,\mathrm{fs}^2$. The additional second order phase induced by the fiber GVD will thus have no significant impact on the pulse duration. Nevertheless, if not taken into account and properly canceled, the newly accumulated phase can be detrimental to subsequent temporal pulse compression. Moreover, GVD can have a negative impact on the coherent combining efficiency, as will be shown in section 3.4.2.

Nonlinear Effects

For high intensity laser pulses, nonlinear effects may occur during pulse propagation. In the femtosecond regime, the most important ones are those related to the optical Kerr effect, which describes a change of the refractive index of a medium induced by the laser field itself, and proportional to its intensity. Hence, the refractive index of the medium becomes $n = n_0 + n_2 I$, which introduces an intensity-dependent nonlinear phase $d\varphi_{\mathrm{NL}} = \beta\, dz = \frac{2\pi}{\lambda} n_2 I(x, y, z, t)\, dz$. As this phase depends on the exact shape of the intensity profile, and since this shape changes constantly during propagation due to the newly accumulated nonlinear phase, the exact impact of the nonlinear phase on the pulse shape can only be simulated numerically by calculating the intensity profile for every increment dz. However, a qualitative understanding of the behavior of the beam when subject to a nonlinear phase can be obtained by considering the temporal and spatial domain independently one from another.

In the spatial domain, the optical Kerr effect generates a refractive index which is higher at the center of the beam than at the edges. The resulting nonlinear phase will lead to a curvature of the wavefronts such that the beam gets focused. In the same time, its diffraction gets stronger, so that it tends to re-diverge. If the peak power of the beam does not exceed the critical power $P_{\text{crit}} = \frac{\pi(0.61)^2\lambda_0}{8n_0n_2}$ [26], the diffraction is stronger than the focusing effect, and the beam is properly guided in the fiber. In the contrary, if P_{crit} is exceeded, the self-focusing effect enhances itself due to continuously increasing peak intensities, so that the beam finally collapses on itself, thereby destroying the material it propagates through. In an optical fiber with refractive indices $n_0 = 1.45$ and $n_2 = 2.5 \times 10^{-20}\,\text{m}^2/\text{W}$ operating at a wavelength $\lambda_0 = 1032\,\text{nm}$, the critical power is given by $P_{\text{crit}} = 4.3\,\text{MW}$. This value is rarely reached in standard fibers, since the peak power has to be limited well below P_{crit} in order to avoid distortions of the temporal and spectral pulse shape due to self-phase modulation (SPM) or damage of the fiber output surface.

Self-phase modulation is the result of a nonlinear phase in the time domain. Assuming a Gaussian temporal pulse profile approximated by a parabola, $\varphi_{\text{NL}} \propto I(t) = -\frac{t^2}{2\delta t^2}$ gives rise to a temporal phase of second order and thus to a frequency chirp which is inversely proportional to the pulse duration (squared). For an initially transform-limited pulse, the second order nonlinear phase leads to a spectral broadening, just as a spectral phase of second order gives rise to a temporal broadening. Furthermore, due to the increased spectral width the impact of dispersion on the temporal pulse shape gets more important, resulting in an increased temporal broadening of the pulse.

On the contrary, an initially stretched pulse exhibits already a strong frequency chirp. Moreover, the impact of the nonlinear temporal phase on the frequency chirp and the spectral broadening is reduced by a factor of C. Hence, the overall effect of the SPM on the pulse profile is quite low, so that the pulse essentially maintains its temporal and spectral shape. However, since for highly stretched pulses the temporal and spectral phase are homothetic, the temporal phase induced by SPM translates directly into a spectral one. It has thus to be taken into account when it comes to pulse compression. Furthermore, any real pulse shape is unlikely to be perfectly parabolic, so that the nonlinear phase contains higher order terms which in any case lead to arbitrary deformations of the spectral phase.

Finally, also pre- or post-pulses which are often present due to various reasons such as imperfect fiber coupling or parasitic reflections from a mirror are affected by nonlinear effects. Indeed, for largely stretched pulses SPM leads to an energy transfer from the main pulse to these pre- or post-pulses as well as to the creation of additional pulses at the harmonics of the initial pulse positions. The presence of a secondary pulse in the time domain leads to an oscillating spectral phase and oscillations in the frequency spectrum. Because of the homothety of the two domains, these oscillations are recovered in the temporal pulse shape, where they give rise to an oscillating nonlinear phase generated by SPM. This phase is then translated back into the frequency domain, where it leads to a nonlinear spectral phase whose oscillations add to those already present on the initial spectral phase. Hence, the amplitude of these oscillations is increased, which results in a relative power increase in the pre- or post-pulses [27]. Thus, even if the main pulse could be recompressed perfectly, at high levels of nonlinearity the transfer of energy to the secondary

pulses due to SPM would still have a detrimental effect on the energy contained in the main pulse.

In order to quantify the general impact of the nonlinear phase on the profile of the femtosecond pulses, a commonly used parameter is the B-integral, which is a measure of the overall nonlinear phase accumulated at the center of the beam of peak power P_{peak} during propagation along a distance z. It is defined as

$$B = \int d\varphi_{\mathrm{NL}} = \frac{2\pi}{\lambda_0} \int n_2 I_{\mathrm{c}}(z)\, dz = \gamma_{\mathrm{NL}} \int P_{\mathrm{peak}}(z)\, dz, \tag{1.12}$$

where I_{c} is the peak intensity at the center of the beam and $\gamma_{\mathrm{NL}} = \frac{2\pi}{\lambda_0} \frac{n_2}{A_{\mathrm{eff}}}$ is the so-called nonlinear parameter. A_{eff} is the effective mode area of the beam in the fiber. It was introduced in order to take into account that the intensity of the fundamental mode reaches its maximum at the beam center, which means that the nonlinear phase accumulated elsewhere is inferior to the estimation based on I_c. However, as the spatial intensity profile in the fiber is the result of a superposition of reflected beams, where each individual beam changes position constantly, and is therefore subject to varying amounts of nonlinear phase, the overall nonlinear phase is averaged over the entire spatial beam profile. It is thus less important than the one expected by considering only the intensity at the center of the fiber. In order to take this effect into account, I_c is replaced by the peak power P_{peak} of the beam and the effective mode area $A_{\mathrm{eff}} = \pi w^2$, which is by a factor of two larger than the "normal" area of a Gaussian beam. Hence, for a given peak power the intensity used for calculating the B-integral is decreased with respect to I_c, which also reduces the resulting nonlinear phase.

Equation (1.12) implies that there are only two ways to limit the B-integral and thus the amount of nonlinear effects: by reducing either the intensity of the beam or the distance z covered in the medium. Reducing z is not the best option due to the characteristics of beam amplification in optical fibers (see section 1.3.2 for more detail). However, there are several well-established techniques which allow to decrease the intensity, either by reducing the peak power of the beam, or by increasing its area. The former one can be achieved by chirped pulse amplification, the latter one by the use of large mode area fibers, as explained in sections 1.2.2 and 1.3.3, respectively.

1.2 Optical Fibers

In principal, optical fibers are very long and thin cylindrical waveguides. They are most commonly used in telecommunication systems because of their high signal transmission rate, their low losses and their robustness. However, there are numerous other applications, one of them being high power fiber lasers and amplifiers. Since the whole front end of the laser system used in this thesis, from the master oscillator to the power amplifiers, relies on fiber technology, this section will give a short introduction into the different types of optical fibers used in our setup.

1.2.1 Working Principle

An optical fiber is typically made of silica, where different dopants lead to different refractive indices in the small fiber core and the cladding around it. In the most common case, the refractive indices are constant within the fiber core and cladding, resulting in a so-called step-index fiber.

A light signal can be guided inside of a fiber core due to total internal reflection at the boundary between the core and the cladding (cf. fig. 1.5). In order to keep the reflection angle inside of the fiber larger than the critical angle of the total internal reflection, the light must enter the fiber at an angle inferior to the maximum tolerable input angle $\theta_{\text{max}} = \arcsin\left(\frac{1}{n}\sqrt{n_{\text{core}}^2 - n_{\text{clad}}^2}\right)$, where n is the index of refraction of the medium surrounding the fiber, n_{core} is the one of its core, and n_{clad} the one of the cladding. Typically, the difference between these two indices is very small, and the fiber is called weakly guiding.

In order to characterize a fiber, one often refers to its numerical aperture NA, defined as $\text{NA} = n \sin\theta_{\text{max}} = \sqrt{n_{\text{core}}^2 - n_{\text{clad}}^2}$. This is another way of describing the acceptance angle of the fiber, that is, the cone of light which is guided when coupled into the fiber. Light from outside of this cone is not guided, since it is transmitted in the cladding rather than reflected back in the fiber core, and therefore lost.

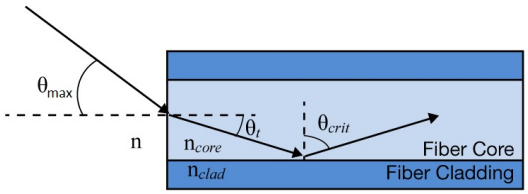

Figure 1.5: Schematic illustrating the light guidance due to total internal reflection in a step-index optical fiber. Picture taken from [28].

A complete description of the spatial shape of the beam inside the fiber, and therefore also at its output, can be obtained by solving Maxwell's equations with the boundary conditions imposed by the fiber. The solutions are a set of guided modes, and involve a combination of Bessel functions and a cosine along the azimuthal angle [22]. However, the intensity distribution of the fundamental mode can be well approximated by the one of a Gaussian beam. The emergence of higher order modes is characterized by the so-called V-parameter of the fiber, given by $V = ak\text{NA}$, where a is the radius of the fiber core and k is the wavenumber. For $V < 2.405$, only the fundamental mode

can propagate in the fiber, and the fiber is called truly single-mode. For higher V-parameters, effective single mode operation can be obtained if the propagation or guidance of higher order modes is suppressed, for instance by bending the fiber and thereby reducing its waveguiding ability.

Typical truly single mode fibers in the infrared wavelength region have a core diameter of about 5.5 µm. However, as the guided mode extends beyond the core-cladding interface, one often uses the mode field diameter (MFD) in order to characterize the fiber. It is defined as $\mathrm{MFD} = 2\sqrt{A_{\mathrm{eff}}}/\pi$, and for the core diameter given above, one finds MFD = 6.6 µm [29].

Furthermore, every mode of the fiber can take two different polarization states, and is therefore degenerate. In a perfect fiber, both polarizations would propagate in the same way, thus remaining independent one from another and conserving the initial state of polarization. However, any real fiber exhibits imperfections such as a slightly elliptical core. This introduces some random birefringence in the initially isotropic fiber. Moreover, local distortions of the fiber, such as bending or twisting, enhance this birefringence. Hence, the two polarization states of the mode propagate with different velocities, thus breaking the mode degeneracy. Furthermore, since the birefringence is induced locally in the fiber, the polarization eigenmodes change locally as well. The projection of one local eigenmode on the subsequent one leads to polarization mode coupling [30]. In consequence, the polarization in an optical fiber changes arbitrarily, and the output polarization state is random.

An optical fiber can be used as a laser amplifier if the fiber core is doped with laser-active ions such as erbium (Er^{3+}) or ytterbium (Yb^{3+}). The pumping necessary for the amplification is then performed optically, which means that an additional pump laser needs to be coupled into the fiber. This can be achieved in two ways: first, the pump beam can be coupled directly into the fiber core. This method is interesting because of its simplicity, however, in the case of single mode fibers it requires a pump laser of high beam quality. As those are somewhat limited in output power, the output power of a core-pumped single mode fiber amplifier stays limited as well.

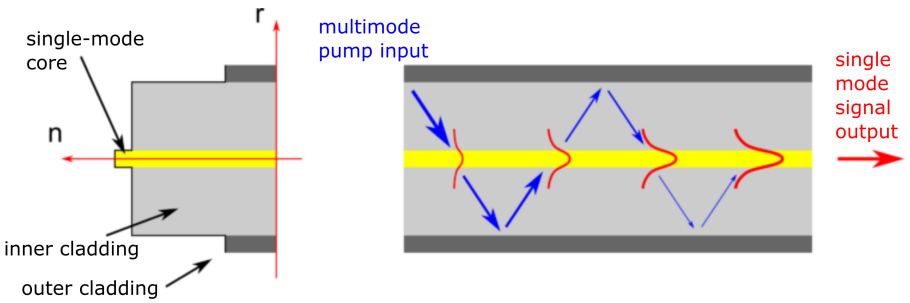

Figure 1.6: Working principle of a double-clad fiber. Picture taken from [31].

The alternative is the use of so-called double-clad fibers. In this type of fiber, an outer cladding is added around the first inner one, so that the signal stays confined in the fiber core, whereas the pump beam is guided by total reflection at the surface between inner and outer cladding, as illustrated in fig. 1.6. As in this case the pump beam is not required to be single-mode, both the numerical aperture and the diameter of the inner cladding can be increased, so that even poor-

quality pump beams can be efficiently coupled into the fiber. Those are often readily available in the form of low cost laser diodes, and can provide considerable pump powers. Hence, double-clad fibers are much better suited for high power amplification.

1.2.2 Special Types of Fibers

Polarization-Maintaining Fibers

Polarization-maintaining (PM) fibers are used if the polarization state of the input beam needs to be conserved. For this purpose, a strong birefringence is introduced in the fiber, so that the two polarization eigenmodes are well defined all along the fiber. Random mode coupling is still possible due to imperfections in the fabrication, bending or stress, but is largely suppressed, so that the initial polarization state is maintained within the fiber. The birefringence is induced by breaking the fiber symmetry, either by making the cladding itself asymmetric or by introducing stress bars parallel to the fiber core which are made of a different material than the cladding, as can be seen in fig. 1.7a.

Large Mode Area Fibers

As the name suggests, large mode area (LMA) fibers are optical fibers where the fiber core and therefore also the guided mode have a larger area than in standard fibers. The advantage is that the larger mode area reduces the intensity of the light in the fiber, so that the impact of nonlinear effects gets reduced. However, if such a fiber shall be truly single-mode, the larger mode area and therefore larger core diameter implies that the numerical aperture has to be reduced. This in turn requires a smaller difference between the indices of refraction of the core and cladding of the step-index fiber, which is difficult to manufacture. In consequence, the fiber is more sensitive to changes in the refractive index induced for example by stress or bending, and the waveguiding ability of the fiber gets reduced. Therefore, the core diameters of truly single-mode step-index LMA fibers are limited to about 15 µm. In contrast, different higher order mode suppression techniques allow to achieve an effectively single-mode operation of fibers with core diameters of up to 30 µm [32].

Photonic Crystal Fibers

A photonic crystal fiber (PCF) is microstuctured, that is, its cross section is interspersed with air holes. This leads to a variety of different fiber designs, each having its particular characteristics and applications [33]. In the PCF used within the framework of this thesis, the air holes are inserted in the fiber cladding, and the light is guided in the solid fiber core. The exact guiding mechanisms of such a PCF are complicated due to the silica-air hole structure of the fiber cladding, and the characteristics of the guided modes can only be determined numerically. A simplified model supposes an effective refractive index of the microstructured cladding which is inferior to the one of the solid fiber core. The light guidance can then be explained by a modified form of total internal reflection, comparable to the one in a step-index fiber [34]. However, a PCF has the advantage

that the effective refractive index of the cladding can be tuned precisely by adjusting the size and spacing of the air holes. Thus, for large core diameters PCFs are more readily manufactured than step-index ones, and MFDs of 35 µm have been demonstrated [35].

Since a main limitation to even larger mode areas is bending of the fiber, unbendable rod-type PCFs have been developed. This allows to design so-called large pitch fibers with MFDs exceeding 100 µm [32], whose output powers are largely increased with respect to standard fiber amplifiers.

Furthermore, a PCF can be made double-clad by inserting a second layer of air holes in the fiber cross section. It is also possible to obtain polarization-maintaining PCFs by inserting stress bars in the microstructured cladding. In the extreme case, the difference in refractive index of the two polarization eigenmodes is that high that only one of the modes is guided. In this case, the fiber is polarizing (PZ).

Due to the air holes in the fiber cross section, a PCF needs to be collapsed after cleaving. This means that the air holes are sealed off in order to prevent water vapor or other contaminants to enter. Since this necessarily removes the microstructure near the fiber end, the light is not guided anymore and diverges in the collapsed part of the fiber. However, this can be an advantage since the larger area of the diverging beam reduces the risk of damage of the fiber output surface. Furthermore, it is possible to add an endcap to the collapsed fiber end. This can be used to further increase the beam area, since the endcap can have a larger diameter than the fiber itself.

In our setup, rod-type fibers cannot be used due to the geometric constraints applied to the fiber endings, as will be explained in section 2.2.1. Thus, we use a state-of-the-art flexible double-clad polarizing ytterbium-doped large mode area fiber with a core diameter of 40 µm and an inner cladding diameter of 200 µm (a DC-200/40-PZ-Yb LMA fiber) [36]. A microscopic photo of its cross section is shown in fig. 1.7c, where the air holes of the cladding and the stress bars are clearly visible. In this fiber design, the guidance of other modes than the fundamental one is suppressed when the fiber is coiled to a certain radius. Therefore, the outer surface of the outer cladding is polished such that the fiber coils automatically in the required way. Furthermore, since both polished parts (only one of which is visible in fig. 1.7c) are parallel to the plane of the stress bars, the polarization of the output beam is automatically aligned with respect to the plane of the fiber bending. Moreover, the doping and therefore the gain of the amplifier contributes to the effectively single-mode behavior of the fiber, since only the parts of the modes which overlap with the doped fiber core are amplified. As this overlap is small for higher order modes, they are amplified much less than the fundamental one, which becomes therefore predominant. Hence, the output beam of the DC-200/40-PZ-Yb is effectively single mode and spatially and spectrally stable only if the fiber is coiled correctly and operated at a minimum pump power.

Finally, a 1 mm diameter endcap was added to the fiber ending in order to enlarge the output beam and avoid surface damage.

Multicore Fibers

The fibers used within the framework of this thesis all have only one single core, as it is most common for optical fibers. However, fibers with multiple cores do exist, and although they follow

the same physical principles as single core fibers, they have some peculiarities typical to the multicore design, such as mode coupling between the different cores [37]. They are of interest for CBC laser systems due to their compactness and the low phase differences between the beams confined in the different cores [38]. The cross section of such a fiber used in a CBC experiment is shown in fig. 1.7b. However, multicore fiber amplifiers are still a relatively new technology, with no commercially available products and a limited number of cores [39]. Hence, at the current state of the art, they are not well suited for the CBC of very high channel numbers.

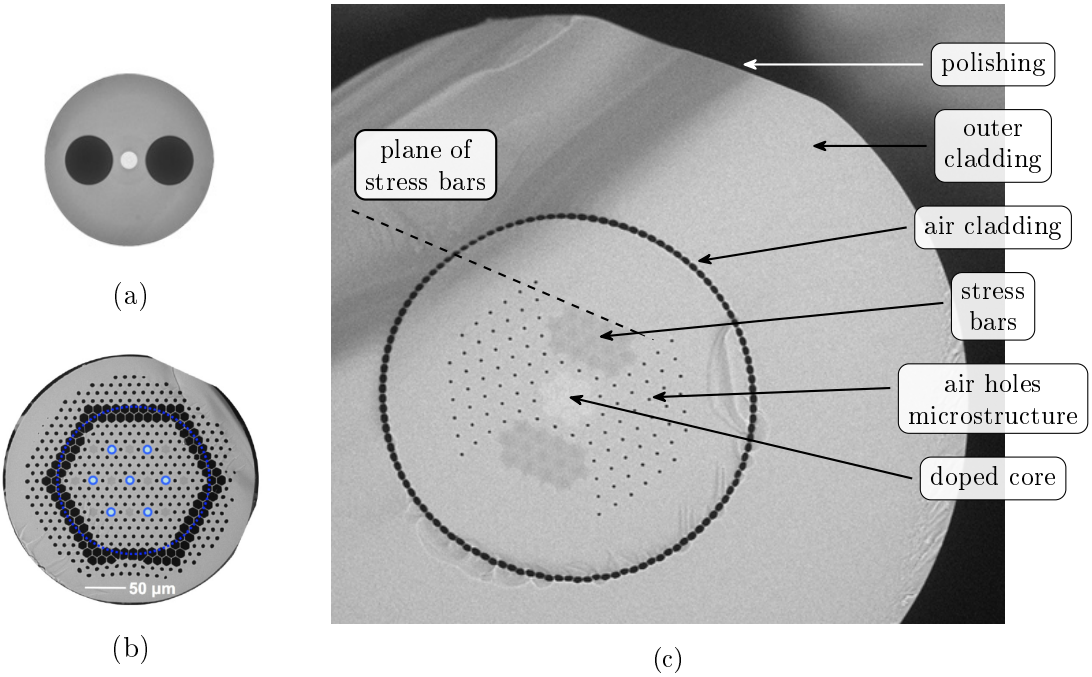

Figure 1.7: Picture of the cross sections of (a) a polarization-maintaining fiber, taken from [40], (b) a 7-core PCF, with the doped cores highlighted in blue, taken from [38], and (c) the DC-200/40-PZ-Yb LMA fiber used as power amplifier in our laser setup.

1.3 Ytterbium-doped Femtosecond Fiber Amplifiers

A fiber amplifier is an optical fiber whose core is doped with rare-earth ions such as erbium (Er^{3+}) or ytterbium (Yb^{3+}). If a pump beam is coupled in the fiber, the ions are transferred in an excited state, so that the laser signal can be amplified by stimulated emission of photons. Due to the long interaction lengths in optical fibers and the efficient heat removal resulting from their high surface-to-volume ratio, these amplifiers are very well suited for the amplification of high repetition rate signals to high average powers.

The characteristics of a specific amplifier, such as its bandwidth and gain, are determined by the doping ions and the hosting material, as will be explained in more detail in the first part of this section. The following two parts include some considerations on the pump beam, and a discussion of chirped pulse amplification.

1.3.1 Signal Amplification and Gain

The wavelength range which can be amplified by the fiber core depends on its spectroscopic properties, which are for their part determined by the dopants and the host itself. In the fiber amplifiers used in our setup, the doping ion is Ytterbium, which can in principle be described as a two-level system. However, as the ytterbium ions are integrated in the amorphous structure of the silica fiber, the electric fields of the surrounding atoms give rise to the Stark effect which causes a splitting and shifting of the initial Yb^{3+} energy levels. Moreover, since every ion sees slightly different electric fields, the individual energy shifts vary from one ion to another. Averaging over all ions thus yields a smooth energy distribution for both levels. Furthermore, it can be assumed that each state is in thermal equilibrium, which means that the ions are most likely in a lower sublevel of the respective manifold. As a consequence, absorption is more likely to take place at lower wavelengths, where ions from a lower sublevel of the ground state are excited, as schematically shown in fig. 1.8a. Conversely, emission is favored at higher wavelengths, corresponding to the emission of a photon from a lower sublevel of the excited state. For intermediate wavelengths, both processes have similar probabilities. The resulting exact absorption and emission cross sections of an Yb-doped silica fiber are shown in fig. 1.8b.

The amplification process is characterized by the frequency-dependent gain coefficient $\gamma(\nu)$, which describes the change in photon number per unit length. It is determined by the difference between the number of absorbed and emitted photons, so that

$$\gamma(\nu) = N_2\sigma_\mathrm{e}(\nu) - N_1\sigma_\mathrm{a}(\nu), \tag{1.13}$$

where $N_{1,2}$ is the number density of Yb-ions in the ground and excited state, respectively, so that $N_1 + N_2 = N$, where N is the total number of Yb-ions. $\sigma_{\mathrm{a,e}}(\nu)$ are the frequency-dependent absorption and emission cross sections of Yb:glass, as shown in fig. 1.8b. The gain coefficient depends thus both on the wavelength and the relative population of the two states.

It is worth noting that even if there is no population inversion, the gain coefficient can be positive in the long wavelength region where $\sigma_\mathrm{e}(\nu) > \sigma_\mathrm{a}(\nu)$. This is the case when only a small pump

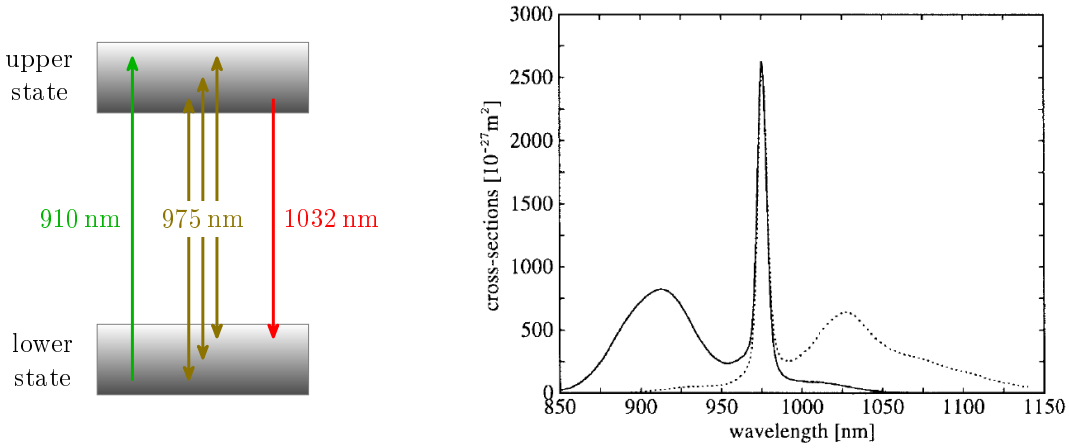

(a) Schematic of the main transitions.

(b) Absorption (solid) and emission (dotted) cross sections, taken from [41].

Figure 1.8: Spectroscopic properties of an Yb-doped fiber amplifier.

power is injected in the amplifier, and results in a low, but broadband gain at wavelengths well above 1000 nm, as shown in fig. 1.9a. In this case, amplification at higher wavelengths is favored. On the other hand, for higher pump powers and therefore larger excited state populations, the overall gain increases, and gets peaked around 1032 nm. Hence, wavelengths around this value get amplified most.

Due to this large gain profile around 1032 nm, Yb-doped fibers are well suited for the amplification of the broadband spectra inherent to femtosecond pulses. However, as the gain coefficient depends on the wavelength, some regions of the pulse spectrum are amplified stronger than other parts. The spectral envelope of the pulses changes thus with amplification. If this envelope was initially centered around the central frequency of the gain spectrum, its width gets reduced, a

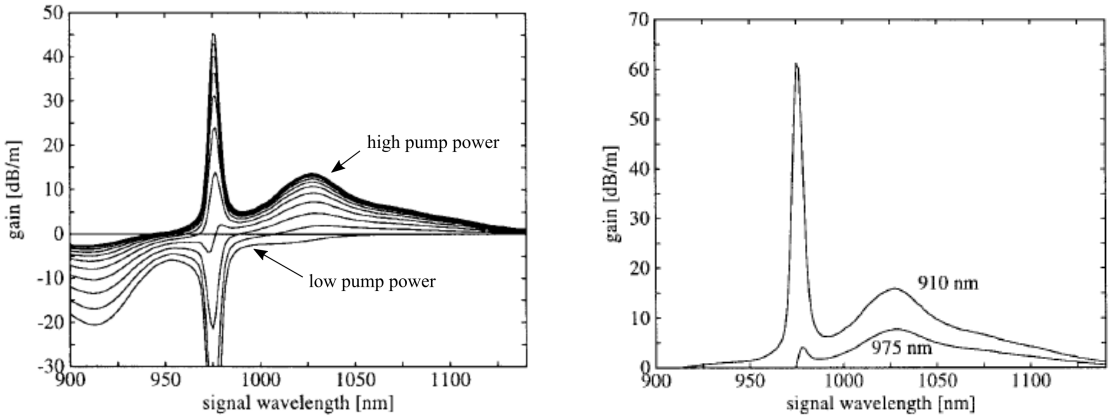

(a) Gain profiles as a function of pump power (from low to high) for pumping at 910 nm.

(b) Gain profiles as a function of pump wavelength for high pump powers.

Figure 1.9: Gain profiles of an Yb-doped fiber amplifiers in dependence of the properties of the pump laser. Pictures taken from [41].

phenomenon which is referred to as gain narrowing. Furthermore, if the gain spectrum is shifted with respect to the pulse spectrum, the amplification process additionally shifts the maximum of the pulse spectral envelope towards the maximum of the gain curve.

The overall gain of the amplifier, given by the ratio between its in- and output power, depends not only on the gain coefficient γ, but also on the power of the input signal. For increasing signal power, the upper state population and therefore the gain decreases. The saturation power P_s indicates the power at which the gain has dropped to half of its maximum value, and is given by $P_\mathrm{s} = \frac{h\nu}{\tau(\sigma_\mathrm{a}+\sigma_\mathrm{e})}A_\mathrm{eff}$ [42], where h is Planck's constant and τ is the upper state lifetime of Yb:glass, given by $\tau \sim 1\,\mathrm{ms}$. For a standard Yb-doped fiber, $P_\mathrm{s} \sim 5\,\mathrm{mW}$, whereas it is as high as $P_\mathrm{s} \sim 180\,\mathrm{mW}$ in the PCF used as power amplifier in our setup.

Depending on the signal power, the amplifier works in two very different regimes. The so-called small signal approximation holds for $P \ll P_\mathrm{s}$. The behavior in this case can be understood by assuming that every photon of the signal induces the creation of a second photon by stimulated emission. Hence, the number of photons and therefore the signal power increases exponentially, so that $P(z) = P(0)e^{\gamma(\nu)z}$. On the other hand, in the heavily saturated case where $P \gg P_\mathrm{s}$, the number of photons is much higher than the number of atoms in the excited state. Therefore, the number of newly created photons is proportional to the number of excited atoms, and the signal grows linearly according to $P(z) = P(0) + \gamma(\nu)P_\mathrm{s}z$ [22].

As fiber amplifiers can be very long and can therefore provide very high gains, they typically operate in both regimes. For instance, the input power of 100 mW of the power amplifier used in our setup is somewhat below its saturation power, whereas the output signal of 25 W is largely saturated.

For pulsed lasers, the impact of the repetition rate of the pulse train on the gain needs to be considered as well. When a CW pump beam is used, the excited state population builds up in between two pulses, since there is no possibility for stimulated emission, and spontaneous emission is suppressed as long as the time between two pulses is well inferior to the upper state lifetime τ. If this is not the case, there is a large risk that spontaneously emitted photons are amplified (ASE, amplified spontaneous emission), which reduces the upper state population and thereby the gain, and mixes unwanted frequencies in the output signal. Since the upper state lifetime of Yb^{3+} is $\tau \sim 1\,\mathrm{ms}$, the pulse repetition rate in our setup should be kept well above 1 kHz in order to avoid ASE.

Besides, due to the build-up of a large upper state population in between the pulses, the leading edge of each pulse is subject to a high gain. For high pulse energies, it partially depletes the excited state, so that the gain is reduced for the trailing edge of the pulse. Hence, the leading part of the pulse is amplified stronger than the trailing one. When the pulses are chirped, this implies that the leading frequencies (the lower ones for a positive chirp) are amplified stronger than the trailing ones, which results in a re-shaping of the pulse spectrum. For low-energy pulses, this behavior is often negligible since the gain depletion per pulse is weak, so that the gain remains approximately constant over the whole pulse. However, for high-energy pulses, serious spectral distortions can be observed, and the gain decreases considerably. The pulse energy necessary to reduce the gain to $1/e$ of its initial value is called saturation energy, and given by $\mathcal{E}_\mathrm{s} = P_\mathrm{s}\tau$. In the power amplifier

used in our setup, $\mathcal{E}_s \sim 180\,\mu J$, so that the pulse energies should be kept well below this value in order to avoid spectral deformations due to gain depletion. In the experiments, the output average power was set to 25 W per amplifier, which means that even at the lowest pulse repetition rate of 750 kHz, the pulse energy does not exceed $\mathcal{E} \sim 33\,\mu J$ and is thus well inferior to $\mathcal{E}_s$.

1.3.2 Optical Pumping

The spectroscopic properties of the gain medium also determine the wavelength of the optical pumping. Considering the absorption spectrum in fig. 1.8b, there are two obvious candidates for pumping of Yb:glass: 910 nm and 975 nm. Since the emission cross section at 910 nm is almost zero, this wavelength allows to transfer a very high amount of ions to the excited state. This implies that the gain curve is very similar to the spectral distribution of the emission cross section, with a strong peak around 975 nm, as shown in fig. 1.9b. If the signal to be amplified is located within the broad peak around 1032 nm, there will thus be a large risk for ASE at 975 nm. The simplest method to overcome this problem is to use this wavelength for the pump laser. Since at 975 nm the absorption and emission cross sections are almost equal, the upper state population is limited to about 50 %. In consequence, the gain in the longer wavelength region is reduced by about a factor of two, and is largely suppressed at the pump wavelength. Hence, spontaneous emission at this wavelength is reabsorbed rather than amplified, and has thus no negative impact on the amplification process. Therefore, and because of the large absorption cross section at 975 nm, this wavelength is typically used for the optical pumping. A convenient side effect of choosing a pump wavelength which is closer to the signal one is that also the quantum defect is reduced, that is, the amount of energy which is lost in the conversion of a pump photon to a signal one.

During operation, care has to be taken that there is always an input signal of constant average power coupled into the fiber amplifier. This ensures that during turn-on of the pump laser, the amplified signal power increases continuously and the gain remains moderate. After a certain time, the system reaches a steady state operation, where both the gain and the amplified signal power remain constant and at a moderate level. However, if for some reason the input signal is interrupted while the pump laser is running, very high gains are built up. Since furthermore an optical fiber can act as laser cavity, these gains can amplify spontaneously emitted photons to power levels largely exceeding those obtainable in steady state operation. This process is known as Q-switching and can in the worst case lead to an optical damaging of the fiber amplifier.

When it comes to coupling the pump laser into the fiber, there are two main options. On the one hand, it is possible to inject both the signal and the pump beam at the same end of the fiber amplifier, which is referred to as forward pumping. On the other hand, the pump can be injected at the opposite end of the amplifier, which is called backward pumping. For both cases, the signal and pump power are qualitatively shown in fig. 1.10 as a function of position in the fiber amplifier. For both pumping schemes, the increase in signal power changes from exponentially to linear as the signal power itself changes from small to saturated. However, in the case of forward pumping, at some point all the pump power has been absorbed, so that the amplification ceases and the signal power starts to decrease slowly due to losses in the fiber amplifier. This behavior does not

occur for backward pumping since in this case the pump is strongest at the fiber end. In contrast, in this configuration care has to be taken that there is enough pump power near the beginning of the fiber, in order to avoid a diminishment of signal power due to fiber losses.

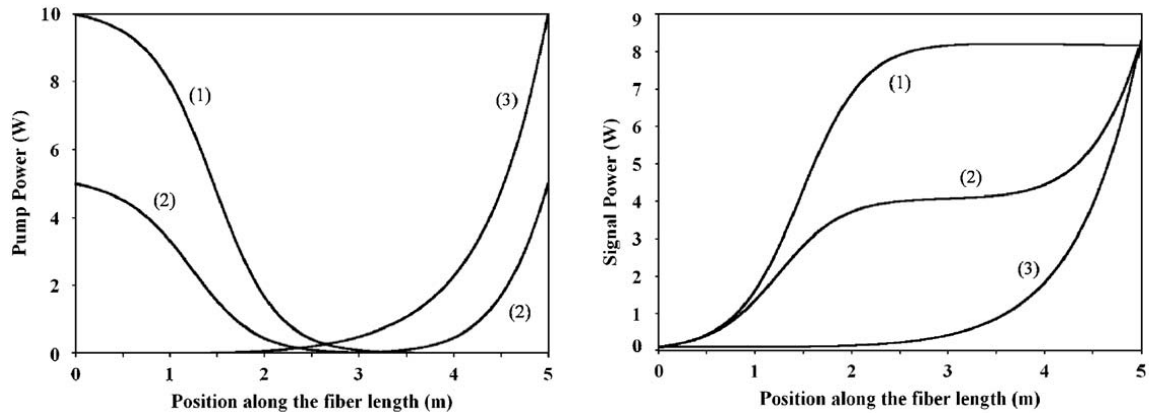

(a) Pump power.

(b) Signal power.

Figure 1.10: (q) Pump and (b) signal power as a function of position along the fiber amplifier for both (1) forward and (3) backward pumping. The case of bidirectional pumping, a combination of the two other cases, is shown as well (2). The figure shows the qualitative behavior in both cases, since the given dimensions do not apply to our specific setup. Pictures taken from [43].

The forward pumping scheme is slightly less efficient than the backward pumping one, since it exhibits a more pronounced ASE near the fiber beginning [44]. Moreover, when nonlinear effects need to be considered, forward pumping is less advantageous since the signal power increases slower near the fiber ending. This implies that quite some fiber length is needed in order to amplify an already strong signal to its maximum power. Since the B-integral scales with the signal intensity, this small endmost increase in signal power comes along with a large increase of nonlinear effects. In practice, the length of the fiber amplifier has to be chosen as a compromise between amplified signal power and B-integral. In a backward pumping scheme, this problem does not occur since the signal power increases steadily till the fiber ending. However, in our setup backward pumping is not possible due to the spatial constraints which are imposed on the fiber outputs. Hence, a forward pumping scheme was chosen and the fiber length of 1.6 m was calculated carefully in order to find the best working point.

1.3.3 Chirped Pulse Amplification

In order to minimize distortions of the spatial and spectral pulse shape induced during amplification of high intensity pulses by self-focusing or self-phase modulation, one commonly uses chirped pulse amplification (CPA, [13]). In this technique, the laser pulses are temporally stretched prior to amplification. This is achieved by passing the pulses through a suitable dispersive optical element, such as a pair of diffraction gratings or a chirped fiber Bragg grating (CFBG). These induce a spectral phase of several orders, which leads to a frequency chirp and a temporal stretching of

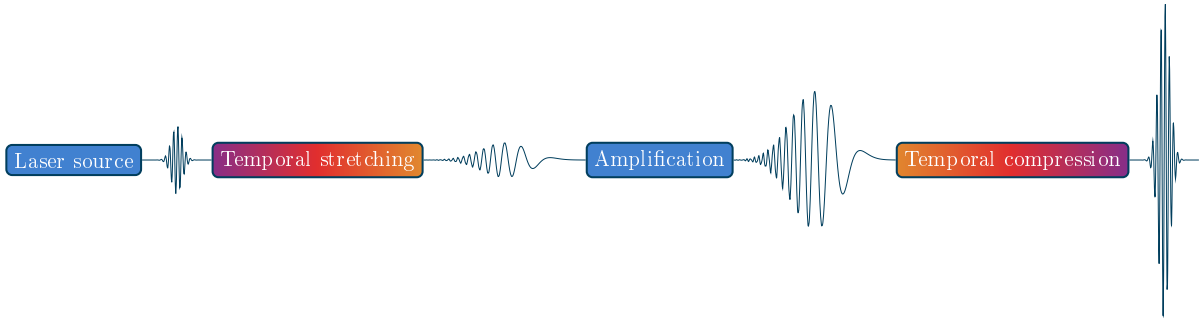

Figure 1.11: Working principle of chirped pulse amplification.

the pulses, so that their peak power is reduced, as depicted in fig. 1.11. After amplification, the spectral phase is removed by passing the pulses through another optical element with the inverse dispersion of the one used as stretcher. Due to the high peak powers attained in this process, the optical element in question usually relies on pulse propagation in free space. For largely stretched pulses, it most often consists of a diffraction grating pair.

The description given above somehow neglects the presence of additional dispersive elements between the stretcher and the compressor, such as the laser amplifier itself. The stretched pulse accumulates thus an additional spectral phase during propagation through these elements. In setups which rely essentially on free-space optics, these phases are often very small and can therefore be neglected. In contrast, in the all-fiber front end of our laser system, much larger spectral phases are accumulated. Hence, in order to recover the initial pulse shape after compression, the dispersion has to be taken into account in the design of the compressor, so that the spectral phase induced by the compressor should cancel the overall accumulated spectral phase rather than only the one induced by the stretcher. Unfortunately, the spectral phase components accumulated in the fibers due to GVD and TOD are both positive, while a grating compressor induces a second and third order spectral phase which are proportional to each other, but of opposite sign. This implies that in such a configuration a total compensation of the spectral phase is only possible if the spectral phase components of the stretcher can be chosen arbitrarily, as it is the case for a CFBG.

While the dispersion is generally well known and can therefore be included in the design of the CPA system, things are much more complicated when it comes to self-phase modulation. As in this case the accumulated phase is highly dependent on the initial conditions and on the exact behavior of the amplifier, the overall accumulated nonlinear phase can not be predicted precisely. Moreover, if developed in a Taylor series, the different orders of the nonlinear phase may have different signs or relative weights than those of the grating compressor, which means that if one order is well compensated, the relative contribution of another order may be increased. It is thus not possible to cancel the complete spectral phase of the pulse, so that the pulse does not recover its initial shape after compression. Indeed, the remaining spectral phase can give rise to a pedestal in the temporal pulse shape, or a broadened pulse profile. The exact temporal shape of the compressed pulse is often a compromise between these two, and depends on the specific alignment of the compressor.

1.4 Conclusion

In this chapter, the physical and technological bases of this thesis have been presented. In a first section, the physics of femtosecond laser pulses and their propagation in optical fibers have been discussed. It has been concluded that care has to be taken to properly manage the dispersion inherent to the all-fiber front end of our laser system, and to avoid excessive nonlinear effects which are detrimental to the temporal and spectral pulse quality.

In a next section, different types of optical fibers used in our setup have been introduced. In particular, the design and functioning of the photonic crystal fiber used as power amplifier have been presented.

Finally, phenomena related to the amplification of femtosecond pulses to high average powers have been discussed. It has been seen that Yb-doped fiber amplifiers are particularly well suited for this task, but that care has to be taken in order to avoid deformations of the pulse spectrum due to inappropriate amplification conditions. Finally, also the CPA technique has been presented.

The combination of all these principles and technologies is at the basis of the next chapter, where different methods of coherent beam combining of femtosecond fiber amplifiers will be discussed.

2 Coherent Beam Combining

In the previous chapter, the limitations in power scaling of femtosecond fiber amplifiers due to nonlinear effects have been discussed. The two main approaches used to overcome these limits have been presented, namely the use of LMA fibers and the CPA technique. However, both methods are hitting their limits. A further scaling of the mode area of fiber amplifiers is difficult due to increasing mode instabilities [45]. In order to reach higher peak powers with CPA, the pulses would need to be stretched more, which would require huge, complex and cost-intensive systems for their recompression.

This is why new approaches for the power scaling of femtosecond fiber amplifiers are being investigated. The current records in terms of peak and average output powers of fiber laser systems have been obtained using coherent beam combining (CBC) [14], which will be introduced in this chapter. In a first part, general aspects and different architectures will be discussed and evaluated with respect to their scalability to very large channel numbers exceeding 1 000 fibers. This will motivate our choice for one specific setup, which will be presented in more detail in the second part of this chapter.

It should be noted that the techniques presented below are limited to those suitable for the power scaling of femtosecond fiber amplifiers in master oscillator power amplifier (MOPA) configuration. Other combining techniques such as coherent pulse synthesis [46], CBC of other laser architectures [47] or passive combining techniques using a joint cavity [48] have been excluded from this description of the state of the art, in order to keep it strictly focused on the topic of this thesis.

2.1 General Aspects of Coherent Beam Combining

A schematic of a general MOPA CBC setup is shown in fig. 2.1. The beam emitted by the master oscillator is spatially split into N sub-beams, each of which is amplified independently of the others. The channels are then recombined coherently, so that one single, very powerful beam is obtained. This procedure can be interpreted as an extension of the already existing concepts of mode area increase and peak power reduction, since the use of multiple fiber amplifiers increases the overall available effective area. In the same time, the peak power in a single amplifier is largely reduced compared to the one obtained after the coherent combination.

In short pulse regimes, this concept can be expanded in the temporal domain, so that a pulse burst is amplified rather than single pulses. After amplification, the burst is recombined temporally so that a single pulse output with increased peak power is obtained.

Furthermore, temporal and spatial beam combining can be implemented simultaneously by

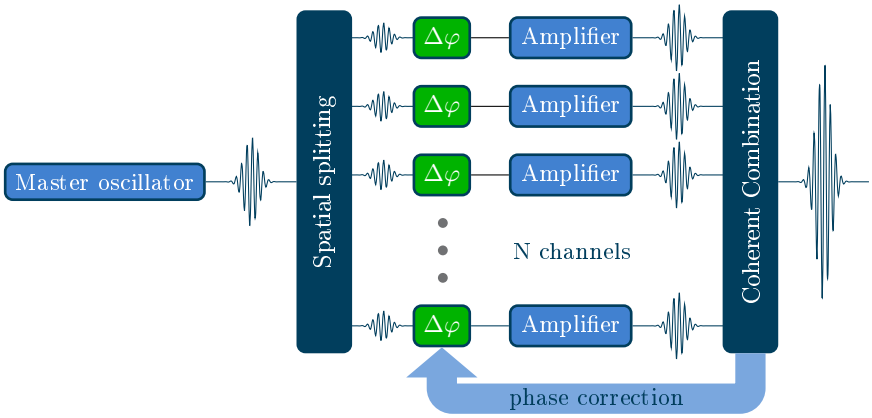

Figure 2.1: General setup of a CBC system with active phase control.

using a spatial CBC architecture as amplification stage within the temporal combining setup.

In order to ensure an efficient beam combination, all the characteristics of the individual pulses, that is, their spatial and spectral envelopes and phases as well as their polarizations, need to be perfectly matched [49, 50]. The combining efficiency η is then defined as the ratio between the power in the combined beam P_{comb} and the total output power of the fiber amplifiers P_{tot}, so that

$$\eta = \frac{P_{\mathrm{comb}}}{P_{\mathrm{tot}}}. \tag{2.1}$$

It should be noted that CBC does not only increase the peak and average power of the laser system, but has also a positive effect on the quality of the output beam. This is due to the fact that only features common to all pulses combine coherently. Aberrations of a single beam with respect to the average are still present in the combined beam, but reduced in intensity by a factor of N. Hence, the combined beam can exhibit spatial and spectral properties which are superior to those of the individual beams.

There are several points which need to be considered when setting up a CBC system: the combination architecture itself, the implementation of temporal beam combining, and the phase matching. In the following, different approaches are presented for these points, and they are evaluated in terms of scalability to a very large number of channels.

2.1.1 Spatial Combining Architectures

The spatial combining architectures can be divided in the two main classes of filled and tiled apertures, whose advantages and disadvantages are discussed below.

Filled Aperture

In a filled aperture geometry, the beams are combined in the near field. This can be done either by combining the beams two by two using (polarizing) beam splitters, as shown in fig. 2.2a, or in a collective approach which makes use of a diffractive optical element (DOE, fig. 2.2b). In both cases, the decrease in combining efficiency due to spatial and spectral disparities converges towards

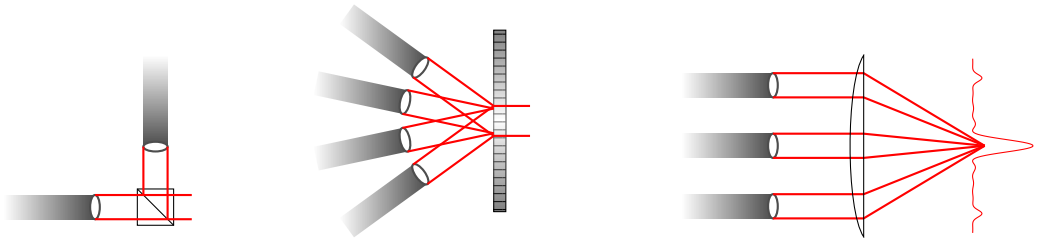

(a) Filled aperture configuration using beam splitters.

(b) Filled aperture configuration using a DOE.

(c) Tiled aperture configuration.

Figure 2.2: Schematic of different CBC architectures, with (a) and (b) a filled aperture configuration, and (c) a tiled aperture.

a constant value for an increasing number of channels [49, 51], so that the overall combining efficiency is only limited by the losses intrinsic to the combining elements.

Using beam splitters as combiners, very good efficiencies of over 90 % have been demonstrated experimentally for the CBC of a moderate number of beams [52, 53]. Moreover, the current record in average output power of a fiber laser system of $P_{\mathrm{av}} = 1.83\,\mathrm{kW}$ has been obtained by combining 16 rod-type amplifiers using thin film polarizers (TFP) as beam combiners, where the combining efficiency of $\eta = 0.82$ is limited by thermal lensing in some optical components [16]. However, CBC with beam splitters is somewhat limited when it comes to the scalability to very large channel numbers, since $N - 1$ beam splitters are necessary to combine N beams. Hence, the component count and therefore the complexity and cost of the system increases linearly with the number of channels. Moreover, if one considers the losses α inherent to the beam splitters, the combined power is proportional to $N(1-\alpha)^{N-1}$ [48]. This function first increases steeply, reaches then a maximum at $N_{\mathrm{max}} = -1/(\ln(1-\alpha)) \approx 1/\alpha$ and decreases afterwards. Hence, once the maximum output power is reached it cannot be increased further by adding more beams. Assuming high-quality AR-coated beam splitters with $\alpha = 0.001$, the number of beams is limited to $N_{\mathrm{max}} \approx 1000$, with a corresponding maximum combining efficiency of $\eta \approx 0.37$.

The problem of an increasing number of combining elements can be overcome by using DOEs, which act as $N \times 1$ beam splitters. However, the losses intrinsic to these elements are largely superior to those of 50/50 beam splitters or TFPs. In a recent demonstration where eight beams have been combined using a pair of DOEs, the intrinsic losses lead to a decrease in combining efficiency of about 10 % [54]. Although this value could be reduced by improving the manufacturing process of the DOEs, a remaining problem is the angular dispersion induced by these elements. Indeed, even when a pair of DOEs is used for the beam combination, the decrease in efficiency due to uncorrected dispersion is estimated to be about 5 % when combining about 200 beams of a spectral width of $\sim 12\,\mathrm{nm}$ [55].

Tiled Aperture

In a tiled aperture geometry, the beams are arranged in an array and collimated in order to obtain a near field. The combined beam is then found in the far field, as depicted in fig. 2.2c. This has

the advantage that no combining elements are needed, and only one lens has to be put in the beam path in order to perform the optical Fourier transform necessary to obtain the far field. However, as the near field is composed of the Gaussian output beams of the fiber amplifiers, its intensity is periodically modulated. This gives rise to secondary lobes in the far field which surround the main central lobe. Since this central lobe is typically considered as the combined beam, the side lobes put an upper limit to the combining efficiency which can therefore never reach 100 %. However, this upper limit is independent of the number of beams to be combined. Moreover, a beam array can be readily extended to include a large number of channels, which explains why the current record numbers of combined fibers have been obtained in tiled aperture configurations, involving 64 beams in CW regime [56] and 19 beams in femtosecond regime [21]. Therefore, this geometry has been chosen for our laser system.

2.1.2 Temporal Beam Combining

In temporal beam combining techniques, a pulse burst is prepared prior to amplification, and temporally combined afterwards. Hence, the amplitudes and phases of all the individual pulses in the burst need to be matched at the temporal combining stage.

Unfortunately, this is not fully possible for setups operating at high pulse energies, since the first pulse of the train partially depletes the gain of the amplifier. In consequence, the following pulses are amplified less strongly and exhibit therefore lower amplitudes and nonlinear phases. In order to overcome this problem, an amplitude shaping of the pulse train is typically performed prior to amplification, so that the gains experienced by the individual pulses are more alike. This allows to match either the amplitudes or the nonlinear phases of the pulses in the train, but not both at the same time. Hence, certain mismatches in at least one of the two properties remain, leading to a decrease in combining efficiency and the creation of pre- or post-pulses which deteriorate the contrast of the combined pulse [57]. Furthermore, it should be noted that at a given pump power temporal combining can only increase the peak power of the output pulses, while the average power remains constant and limited by the aforementioned pump power.

There are two different temporal combining schemes which are currently being investigated. In the divided pulse amplification (DPA, [58]) technique, the pulse burst is generated by separating the pulses in two different polarization states. This can be achieved in two ways. On the one hand, it is possible to use birefringent crystals, as has been done in the first experimental demonstration of DPA [58]. However, as the delay that can be induced by a crystal of reasonable size is limited, this approach is only applicable to unchirped femtosecond pulses, and therefore not suitable for the amplification to high peak powers. On the other hand, polarizing beam splitters and suitable delay lines can be used, so that larger delays can be obtained [59]. Hence, this method is compatible with temporally stretched pulses. Moreover, when it comes to the amplification to high energies, the amplitude shaping described above has to be taken into account. This implies that the amplitudes and phases of the amplified pulse burst vary considerably from those of the input pulses. Hence, independent delay lines are needed for the temporal pulse separation and recombination, and an active phase stabilization has to be implemented. This has the further advantage that any

chirped-pulse multi-channel spatial CBC setup can be inserted between the temporal splitting and combining stages. Indeed, the current record in output peak power of a femtosecond fiber amplifier system has been obtained by coherently combining four temporal and eight spatial pulse replicas. It was thus possible to demonstrate a pulse energy of 12 mJ at a repetition rate of 56 kHz and an overall combining efficiency of 78 % [15]. However, creating more than four replicas is difficult due to the strongly increasing system complexity and the intrinsic mismatches between the amplitudes and nonlinear phases of the amplified pulses in the burst, which lead to a decrease in combining efficiency. Furthermore, the use of DPA is limited to systems using exclusively fibers whose amplification characteristics are independent of the polarization state of the beam.

In contrast, in the coherent pulse stacking technique [60], the pulse burst is carved directly out of the master oscillator signal. The recombination is performed in a modified form of a Fabry-Pérot interferometer, called Gires-Tournois interferometer, which is aligned such that one round trip time corresponds exactly to the repetition rate of the pulses in the burst. The pulse burst is then prepared such that all but the last pulse interfere destructively at the resonator output port, so that their power remains in the interferometer and adds up. The last pulse is then used to extract the stored energy via constructive interference at the resonator output. Using this method and a pulse burst comprising 81 individual pulses, pulse energies of ~ 10 mJ have been achieved at a pulse duration of 540 fs [61]. A combination of this technique with spatial beam combining seems possible, but has not been demonstrated yet.

2.1.3 Phase Matching Techniques

As pointed out above, phase differences among the beams have to be balanced in order to obtain en efficient CBC. For femtosecond setups, this means that all orders of the spectral phase need to be matched. Orders higher than zero are typically constant in time, so that a static adjustment is sufficient [62]. This means that the group delay of the different channels need to be matched at all orders, so that delay and dispersion differences among the pulses are suppressed. In contrast, the zeroth order phase fluctuates due to acoustic and thermal noises. It is therefore essential to implement a real time phase offset correction. The necessary bandwidth of this correction depends strongly on the employed material and the experimental conditions. For instance, it has been concluded from measurements of phase fluctuations in an Yb-doped fiber amplifier that a bandwidth of at least several kilohertz would be necessary to obtain a phase correction on the order of $\lambda/10$ peak-to-valley. This value is considered as the maximum tolerable residual phase error for an efficient CBC [63]. However, various implementations demonstrate residual phase errors below $\lambda/40$ RMS with considerably lower bandwidths in the range of 500 Hz to 1 kHz [20, 52]. An extreme case was reported for the coherent combining of the different cores of a multicore fiber, where a bandwidth of 2 Hz was sufficient due to the low phase differences among the cores [38].

Similarly, various devices can be used for the phase correction, such as piezomechanical actuators used for translating a mirror [53] or stretching a fiber [20], electro- or acousto-optical modulators [52, 63], and in the case where a high bandwidth is not required, spatial light modulators [38].

In the following, different phase matching methods are presented, and each of them is evaluated with respect to its suitability for a highly scalable CBC system in tiled aperture configuration.

Passive Phase Matching

In passive phase matching approaches, the laser system is set up such that the phases of all emitters match automatically. In a MOPA configuration, this can be achieved by using a so-called Sagnac interferometer, where all pulses traverse the same optical components and amplifiers. They accumulate thus automatically the same spectral phase, so that no external phase correction is necessary. This allows to achieve very high combining efficiencies. For instance, $\eta = 0.96$ has been shown for the coherent combination of two amplifiers [64]. However, combining more than two channels using this architecture has not been demonstrated yet, and seems difficult due to increasing system complexity and the large amount of B-integral accumulated over the long distances which the beams cover in the amplifiers [48]. Moreover, as such a setup necessarily implies a filled aperture configuration, it is not well suited for CBC of a very large number of beams.

Hänsch-Couillaud Interferometry

Hänsch-Couillaud interferometry relies on the use of polarizing beam splitters as combining elements. The beams need thus to be combined two by two in a filled aperture configuration. Supposing that both beams have the same power and are orthogonally polarized, the polarization of the combined beam should be linear and turned by 45° with respect to the one of the input beams. Deviations from this ideal polarization are attributed to phase fluctuations between the two beams, which allows for the generation of an error signal for the active phase correction. This method has been proven to be well applicable to CBC of a moderate number of beams yielding very good combining efficiencies of more than 90 % [53], but is not suitable for a use in tiled aperture configuration.

Frequency Tagging

Another commonly used method for phase matching is the so-called locking of optical coherence via single-detector electronic-frequency tagging (LOCSET). It consists in modulating the phase of each channel with a unique, small amplitude frequency dither. This allows the identification of every channel in the combined beam by demodulating the recorded power signal at the respective frequencies, and the subsequent deduction of each individual phase with respect to the phases of all other channels. The advantage of this technique is that the detection is performed with one single device, and combining efficiencies higher than 90 % with residual phase errors as low as $\lambda/40$ RMS have been achieved by combining two femtosecond fiber amplifiers using LOCSET [52]. However, the number of beams which can be phase locked is limited by the number of available tagging frequencies, and is estimated at $N \approx 200$. Hence, the scalability of systems using LOCSET remains limited, even if the algorithm itself seems well suited for the application in a tiled aperture configuration.

Techniques to overcome this scaling limitation have been proposed [65, 66], but require several combining stages and one detector per stage. Hence, they make void one of the main qualities of LOCSET and are best suited for filled aperture configurations.

Hill-Climbing Algorithm

The stochastic parallel gradient descent (SPGD) algorithm is a phase matching method which does not require the measurement of individual phases. Instead, small phase variations are randomly applied to all the channels, and the corresponding power of the combined beam is measured. Based on this result, the algorithm varies the phase offsets such that the combined power is maximized. This approach has the advantage of a relatively simple implementation which requires neither multiple detectors nor RF electronics, and was successfully implemented to phase lock moderate numbers of channels [38, 54]. However, the convergence time of the algorithm increases linearly with N [48], so that it is not suitable for the real time phase matching of a very large number of beams. Nevertheless, SPGD algorithms can still be used to find optimal configurations for static or slowly varying parameters, and will be applied in this context in our setup (cf. section 2.2.2).

Phase-Intensity Mapping

A recently proposed phase matching method for CBC in tiled aperture configuration relies on the so-called phase-intensity mapping (PIM), which converts relative phase differences within the fiber array into intensity differences. Behind the PIM device, the measured intensity of each beam in the array is compared to the one which would be obtained if all the beams of the input array were perfectly in phase. From these results, an iterative algorithm calculates the phases that need to be applied to the input beam array in order to obtain the best possible match between the measured and the calculated intensities, which corresponds to a phasing of the beam array. Simulations have shown that phase locking of almost 500 beams should be possible with this technique [67], and an experimental implementation using 37 CW laser beams yielded a good residual phase error of $\lambda/25$ [68].

Although this method seems to be suitable for the phase locking of femtosecond lasers, it could not be considered as phase matching technique for the XCAN laser system since it was developed only after the project had started.

Collective Interferometric Measurements

In collective interferometric phase measurements, each beam interferes with a common reference beam, which allows to determine the relative phase between each emitter and the reference.

This can be achieved either in the temporal or in the spatial domain. In the first case, each beam is superposed with the same frequency shifted reference beam, and the resulting beat signals are recorded with photodiodes. The phase of each beam can then be deduced by demodulating the beat signals at the shifting frequency. This approach is somehow similar to the LOCSET technique, with the advantage that only one modulation frequency is needed, but with the drawback

that it requires N photodiodes and that the phase is only measured with respect to the reference beam.

In the spatial domain, interference can be obtained by superposing each beam with one and the same tilted reference beam. The resulting fringes are then detected on a fast CCD camera, and the relative phase between each beam and the reference can be calculated based on the exact position of the fringes on the camera screen. This approach is thus only limited by the number of beams which can be imaged on the camera, and by the time needed for the acquisition and analysis of the camera images. Besides, it has been shown that by using exclusively readily available equipment, the phase matching of an array of about 10 000 beams at a bandwidth of 1 kHz is theoretically possible [20]. Moreover, the highest number of coherently combined channels in the femtosecond regime has been obtained using this method on passive fibers [21]. This shows that this technique is well suited for femtosecond CBC of very large fiber arrays, and has therefore been chosen for the XCAN setup. More details on the exact implementation are given in section 2.2.2.

However, this approach has also some disadvantages. First of all, the use of a reference beam is cumbersome and somehow complicates the setup. Furthermore, since the phases of all beams are locked with respect to the reference beam, there is no guarantee that they are locked in phase with each other. Hence, an individual phase offset has to be applied to each beam in order to ensure constructive interference in the combined beam.

Self-Referenced Interferometric Measurement

In order to overcome the limitations of collective interferometric measurements, self-referenced methods relying on the spatial interference between adjacent beams have been proposed. The quadriwave lateral shearing interferometry technique uses a diffraction grating to spatially split each beam into several replicas, which overlap with those of the adjacent beams after having propagated a certain distance. The phase of a single beam is then calculated based on all the interference patterns originating from this beam [69]. Hence, several fringe patterns need to be evaluated in order to obtain the phase of one beam, which makes this approach more time-consuming than the one presented above, and therefore less well scalable to very large channel numbers. Nevertheless, this technique has been used in the CW regime in order to coherently combine a record number of 64 fibers [56]. A related approach suggests to omit the grating and use the interference fringes emerging in the free space propagation of the near field beam array instead [70]. However, CBC using this technique has not been demonstrated yet.

In conclusion, self-referenced techniques are very promising, but not yet mature enough to assure an easy and reliable phase matching for very large fiber arrays. Therefore, we decided to rely on the collective measurement presented before which uses a common reference beam.

2.2 Implementation in the XCAN Setup

In the previous section it has been concluded that a tiled aperture arrangement in combination with an interferometric phase measurement technique are best suited for the coherent combination of a very large number of channels. These configurations have thus been implemented in the XCAN setup, and will be presented in more detail in this section.

2.2.1 Tiled Aperture Configuration

In a tiled aperture configuration, highest combining efficiencies can be obtained for highest fill factors of the near field aperture. In consequence, the beam width has to be close to the array pitch, which can be achieved by collimating the beams after having them diverge over a certain distance. This has the side effect that each beam is clipped by its respective collimating lens, so that a certain part of the beam is not correctly collimated and therefore lost for the subsequent combining process, as illustrated in fig. 2.3a.

Such a configuration results in a side-by-side arrangement of circular beams, so that a hexagonal fiber array leads to the highest aperture filling [48]. Such an array is shown in fig. 2.3b. Since only completely filled hexagons make sens, this geometry gives rise to odd numbers of combined channels such as N = 7, 19 or 61. This number is related to the normalized diameter N_D of the hexagon by $N = 1 + \frac{3}{4}(N_D^2 - 1)$.

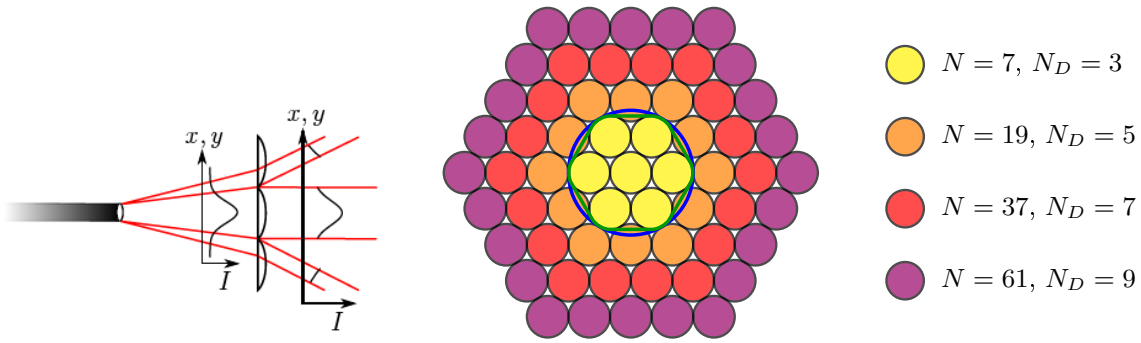

(a) A part of the beam is not collimated by the designated lens, and therefore lost for the subsequent combining process.

(b) Hexagonal "honeycomb" array with corresponding number of beams N and normalized diameter N_D. The green line indicates the shape of the actual seven fiber aperture, while the blue line shows its approximation by a circle.

Figure 2.3

Mathematically, the resulting near field can be described using four variables: a Dirac comb Ш_p describes the position of the beam centers on a hexagonal grid with pitch p. In order to take into account the finite size of the beam array, it is multiplied by a function Π_A describing the geometrical shape of the global aperture. Each individual beam can be expressed via a Gaussian envelope of width w, $E_w(x, y) = \exp(-\frac{x^2+y^2}{w^2})$, which is multiplied with the aperture of the collimating lens Π_L. The near field E_{NF} as depicted in fig. 2.4a can then be expressed by the

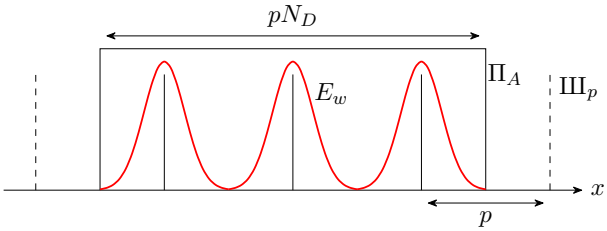

(a) Lineout of the near field with characteristic length scales. For simplicity, the lens aperture Π_L has not been included in the scheme.

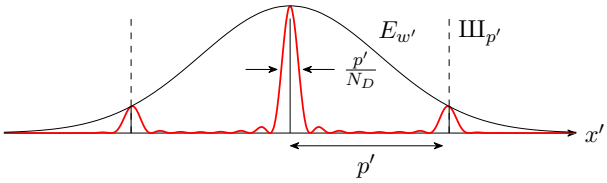

(b) Lineout of the corresponding far field, where the impact of Π_L is not shown.

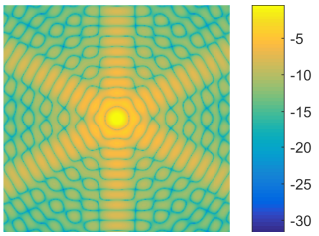

(c) Fourier transform of a hexagonal aperture. Note the logarithmic color scale.

Figure 2.4: Lineout of the (a) near and (b) far field of a tiled aperture configuration. (c) shows the two-dimensional Fourier transform of a hexagonal aperture function.

convolution of these two products, so that

$$E_{\text{NF}} = (\text{Ш}_p \times \Pi_A) \otimes (E_w \times \Pi_L). \tag{2.2}$$

The far field E_{FF} is given by the Fourier transform of E_{NF}. According to the convolution theorem, it can thus be expressed via the Fourier transforms of the individual components of the near field. Both the Dirac comb Ш and the Gaussian envelope E transform into themselves, but exhibit a modified period $p' = \lambda f/p$ and width $w' = \lambda f/(\pi w)$, respectively, where f is the focal length of the lens used to perform the Fourier transform experimentally. The Fourier transform of the global aperture Π_A has to be calculated numerically. As the hexagonal array is composed of circular beams, the aperture has the shape of a hexagon with rounded corners. For a seven fiber beam array, it can therefore be well approximated by a circular aperture (cf. the green and blue lines in fig. 2.3b), whose Fourier transform is given by the Airy function Ai. For larger beam numbers, the hexagonal features of the aperture become more pronounced, and $\mathcal{F}(\Pi_A)$ converges towards the Fourier transform of a hexagon, which is shown in fig. 2.4c. It should be noted that the Fourier transforms of both apertures exhibit significant side lobes around the main lobe. Furthermore, the width of this main lobe is inversely proportional to the size of the aperture itself. Finally, the Fourier transform of the lens aperture Π_L depends on the geometrical shape of the collimating lens. In our setup, we use a hexagonal array of hexagonal microlenses, so that $\mathcal{F}(\Pi_L)$ is given by the Fourier transform of a hexagon.

The far field can then be written as

$$E_{\text{FF}} = (\text{Ш}_{p'} \otimes \mathcal{F}(\Pi_A)) \times (E_{w'} \otimes \mathcal{F}(\Pi_L)). \tag{2.3}$$

The convolution of the new Dirac comb with $\mathcal{F}(\Pi_A)$ yields a hexagonal distribution of peaks with pitch p', whose width depends on the size of the beam array. Their side lobes stretch out in between the peaks. This basic pattern is modulated by the convolution of $\mathcal{F}(\Pi_L)$ with the Gaussian envelope $E_{w'}$. If the aperture of the collimating lens is sufficiently large compared to the diameter of the beams, the clipping is negligible and the envelope reduces to $E_{w'}$. In contrast, if the beams are noticeably clipped, the convolution has to be considered, and due to the side lobes of $\mathcal{F}(\Pi_L)$ the resulting envelope exhibits side lobes as well.

The multiplication of the basic pattern with this envelope leads to a far field with one strong central lobe, whereas the other peaks are reduced in intensity, as shown in fig. 2.4b. Since for a given Π_L the width of the envelope scales as $w' \propto 1/w$, more side lobes will appear if the beam width in the near field is reduced, resulting in a decrease in combining efficiency. Conversely, larger beams in the near field result in a better suppression of the side lobes in the far field and therefore a higher combining efficiency. Hence, larger w in the near field should be preferred. However, larger beams also result in an enhanced clipping at the collimating lenses, which leads not only to power losses directly at the lenses, but also to the appearance of side lobes of the envelope at the edges of the far field, so that the combining efficiency gets reduced. In consequence, the optimum beam size is a compromise between aperture filling and microlens clipping. Simulations used to calculate the best beam size will be presented in the next chapter.

Moreover, the combining efficiency is very sensitive to misalignments in the hexagonal beam array. Previous studies have investigated this effect for a rectangular beam array in terms of decrease of the Strehl ratio, which compares the on-axis power of the simulated system with an ideal one [71]. In the following chapter, these simulations will be adapted to the hexagonal array used in our setup, in order to find the maximum error tolerances acceptable on our fiber array.

Finally, the tiled aperture geometry has an impact on the choice of the specific fiber amplifier to be used. Since high combining efficiencies can only be obtained with a large aperture filling, empty space between the beams in the near field should be avoided. Hence, beam collimation with individual lenses and corresponding mounts is suboptimal, and the use of microlens arrays is preferred. Their typical pitches in the range of 100 µm to a few millimeters have to be applied to the fiber array as well. The use of unbendable rod type fibers becomes therefore impractical, and we use the DC-200/40-PZ-Yb LMA fiber presented in section 1.2.2 instead. This guarantees state of the art performances in terms of average and peak power of a single emitter, while also keeping the flexibility necessary to insert the fibers in an array with a pitch on the order of a few millimeters. However, as this fiber is polarizing, our spatial CBC setup cannot be combined with the polarization-dependent DPA technique. Hence, no temporal beam combining scheme was implemented.

2.2.2 Interferometric Phase Measurement

As explained in section 2.1.3, a collective interferometric phase measurement consists in the superposition of the beam array with a reference beam. In our setup, we work with a superposition in the spatial domain, so that a single fast camera is used as common detector for all beams. A

small power fraction of the near field is then imaged on the camera screen, and superposed with a plane wave reference beam which is aligned with a small angle α to the camera, as depicted in fig. 2.5a. This results in N fringe patterns on the camera, as shown in fig. 2.5b, and allows to correct both the relative delay φ_1 and the phase offsets φ_0, as will be explained in the following.

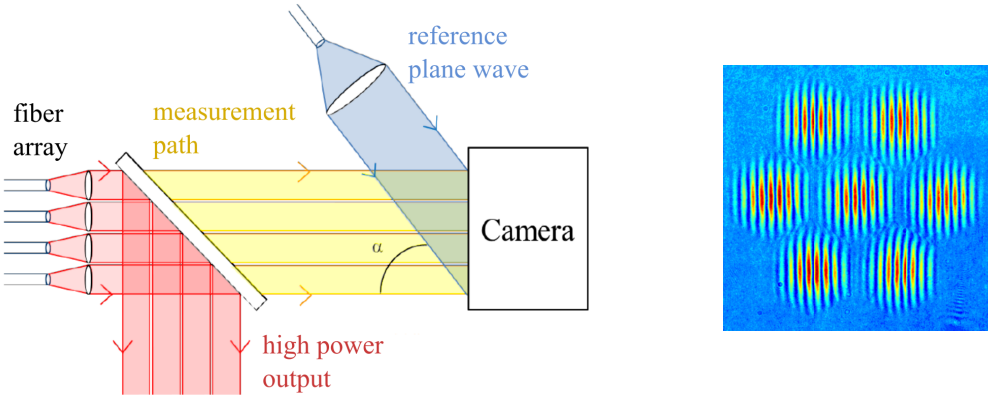

(a) (b)

Figure 2.5: (a) Schematic illustrating the phase measurement setup, adapted from [72]. For the sake of clarity, the tilt angle α of the reference beam is heavily exaggerated, and the imaging system in front of the camera is not represented. (b) Resulting interference fringes on the camera for $N = 7$ beams.

Delay Adjustment

Intuitively it is easy to understand that the pulses of the different amplifiers must arrive at the same time if they shall recombine coherently. Hence, in a first step, the relative delay between the pulses needs to be adjusted. This can be done by optimizing the contrast of the interference fringes on the camera, as illustrated in fig. 2.6 for chirped pulses. If the delay between the pulses is superior to their coherence time, no interference is possible and the camera images the Gaussian beams of the near field, as shown in fig. 2.6a. When the delay is inferior to the coherence time, but not fully compensated, interference is possible only for the parts of the pulses which overlap both in the time and frequency domain, as shown in fig. 2.6b. This results in an interference pattern with a bad contrast, since the non-interfering parts of the pulses add an incoherent background. Finally, when the delay between the pulses is well compensated, the whole temporal profile of the pulse contributes to the interference, and the contrast is maximized, as illustrated in fig. 2.6c.

This approach is appealing due to its simplicity, but it entails several issues.

First, this method is not very precise. It has been seen experimentally that relative delays inferior to $\sim 60\,\mathrm{fs}$, which is more than 25 % of the pulse duration, do not visibly deteriorate the fringe contrast, but have a negative impact on the combining efficiency. Hence, in the experiments with a seven beam array, the delays were first adjusted roughly based on the contrast of the interference fringes. Afterwards, the fine tuning was performed by measuring the combining efficiency in the far field and manually adjusting the delays accordingly. However, this is only possible for small beam arrays, where the adjustment of the parameters of one beam has a noticeable impact

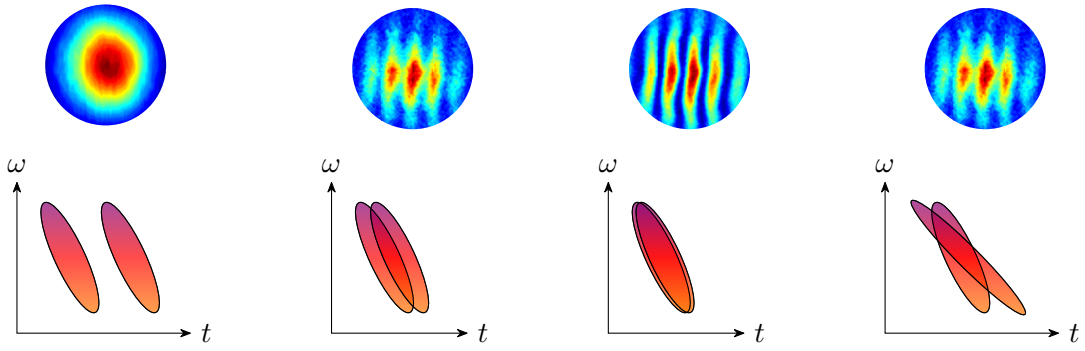

(a) Large delay, no overlap, no fringes.

(b) Moderate delay, small overlap, bad contrast.

(c) Very small delay, almost perfect overlap, very good contrast.

(d) Perfect overlap and good contrast not possible due to different chirps.

Figure 2.6: (a) - (c) Interference fringe pattern and corresponding time-frequency mapping for different delays between two chirped pulses. (d) Situation for two pulses with different chirps.

on the overall combining efficiency. This is not the case for $N = 61$ beams, where a single beam represents only 1.6 % of the overall beam array. Hence, the changes in combining efficiency due to the relative delay of a single beam are not necessarily distinguishable from those due to noise, which makes a one-by-one alignment impossible.

Second, for very large beam arrays, the tilt angle of the reference beam can become problematic. As the wavefronts are tilted with respect to the camera, the arrival time τ of the reference pulse at the screen varies linearly with its horizontal position. Since the delays of the beam array are adjusted with respect to this arrival time, they will also vary linearly with position, as illustrated in fig. 2.7. For instance, if one considers an interference pattern with five fringes per beam, the phase difference between the extreme edges of two outward beams is $15\,\lambda$ for a seven fiber array. This translates into a relative delay of 50 fs, which is on the order of magnitude of the precision in the adjustment of the delays based on the fringe contrast. Hence, in the seven fiber array the tilt of the reference beam will have no further impact on the delay alignment, and therefore on the combining efficiency.

In contrast, if one considers a 61 beam array under the same conditions, the delay between the two outmost beams becomes 150 fs, which is about two thirds of their coherence time. As this is detrimental to the combining efficiency, a way to compensate this linear delay dependence has to be found.

Third, this delay adjustment method works well only if all the channels have the same second order spectral phase as the reference beam. If this is not the case, for instance because the reference beam is not power amplified and therefore not subject to nonlinear phases, interference is only possible between a certain part of the temporal envelope of the stronger chirped signal pulse and the temporally unchanged reference beam, as shown in fig. 2.6d. Hence, there is always an incoherent background mixed to the interference pattern, and the contrast remains moderate for a wide range of delays. In such a case it is therefore not possible to compensate the relative

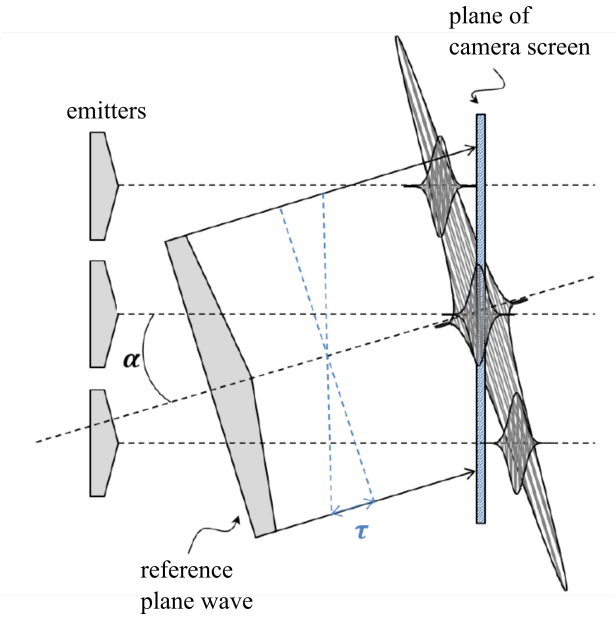

Figure 2.7: Schematic illustrating the different delays of the pulses due to the tilt angle of the reference beam, adapted from [73].

delays among the pulses solely by considering their contrast on the camera screen.

In order to overcome these three inconveniences, an SPGD algorithm is intended to be implemented in the 61 fiber setup for the precise optimization of the relative delays.

Phase Offset Correction

Once the delays are adjusted such that for all beams there are interference fringes visible on the camera, these can be used to measure the relative phase offsets between the signal beams and the reference one. This is done using an algorithm as described in [20]. It calculates the relative phases based on the position of the interference fringes on the camera. If a beam is perfectly in phase with the reference beam, the first maximum of the interference pattern will be located exactly at the center of the Gaussian envelope. Deviations from this position are due to phase differences, and can therefore be used to determine these latter ones. This could readily be done using Fourier transforms. However, as these calculations are relatively time-consuming and the feedback algorithm needs to run in the kilohertz regime, an approach using correlation calculations is implemented instead.

This method is based on the calculation of a library of reference interference patterns $R^i(\varphi_i)$, each corresponding to a fixed phase offset φ_i. Subsequently, the correlation coefficient between the measured fringe pattern S and every R^i is calculated in real time. This is depicted in fig. 2.8 for three different R^i. The measured phase corresponds then to the phase used to calculate the library pattern R^i which yields the highest correlation coefficient. The precision of this phase measurement is given by the number N_P of reference patterns in the library, since the phase is probed in intervals of $2\pi/N_P$.

As mentioned in section 2.1.3, this method locks the phases with respect to the reference beam,

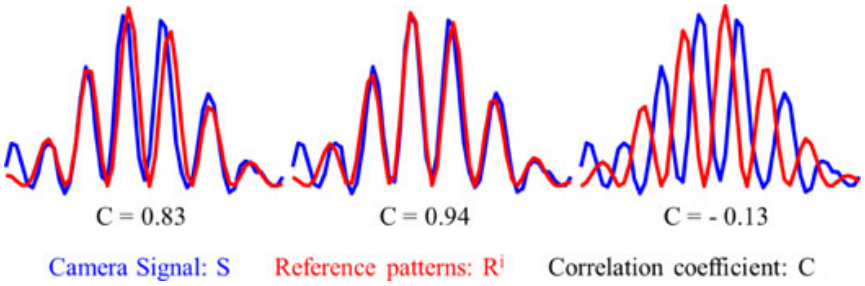

Figure 2.8: Schematic illustrating the phase measurement based on correlation calculations. The recorded camera signal S is shown in blue and the reference patterns R^i in red. The measured phase is the one used to calculate the reference pattern yielding the highest correlation coefficient C. Picture taken from [20].

which means that the phase locking does not automatically guarantee constructive interference in the far field. Hence, it is necessary to define a set point for each beam to which its phase offset shall be locked. Although an optimization of these offsets with respect to the combining efficiency would have been possible by hand in the seven fiber setup, better results have been obtained using a dedicated SPGD algorithm.

2.3 Conclusion

In the first part of this chapter, different CBC architectures and phase matching techniques have been presented. It has been concluded that for a CBC setup which should be scalable to more than 1 000 channels, a tiled aperture configuration in combination with an interferometric phase measurement is the best choice.

In the second part, these two approaches have been presented in more detail. In tiled aperture configuration, highest combining efficiencies are obtained with a hexagonal fiber array. Nevertheless, misalignments in this fiber array can lead to decreases of the combining efficiency. Besides, the interferometric phase measurement allows for an easy matching of both phases and delays of the beams, but especially the latter suffers from imprecisions in the adjustment.

In order to estimate the maximum imprecisions tolerable in our setup, the losses in combining efficiency due to various alignment errors both in the spatial and spectral domain have been calculated numerically. The results of these simulations are presented in the next chapter.

3 Simulations of the Beam Combining Setup

As mentioned in section 2.2.1, an accurate positioning of the fibers in a hexagonal array is essential for a high efficiency CBC in tiled aperture configuration. Moreover, also the spectral properties of the beams need to be very well matched. In this section, the maximum error tolerances for our specific setup will be determined based on numerical simulations.

3.1 General Setup

We suppose a hexagonal array of Gaussian beams, each of which gets both collimated and truncated by a hexagonal microlens. The far field is found by an optical Fourier transform of this composite near field, and the combined beam is given by the central lobe of the far field. Spatial filtering with a circular aperture allows to select the central part of the far field, which is then again Fourier transformed in order to access the recovered near field. A schematic of this setup is shown in fig. 3.1.

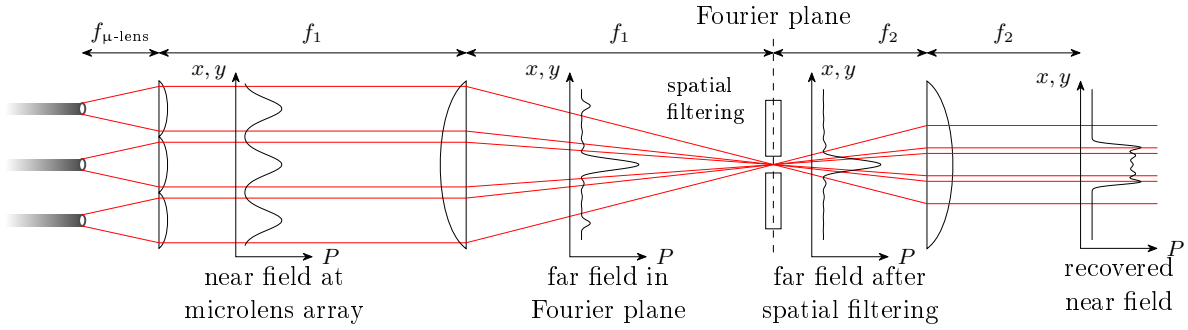

Figure 3.1: Schematic of the simulated setup.

The output of each individual fiber is supposed to be a Gaussian beam of the form

$$E_i(x,y) = E_{0,i} \exp\left(-\frac{(x-x_{f,i})^2 + (y-y_{f,i})^2}{w_{0,i}^2}\right), \tag{3.1}$$

where E_0 is the amplitude of the beam, w_0 its waist at $1/e^2$, and (x_f, y_f) are the coordinates of the beam center. Hence, the total output power is given by $P_{\text{tot}} = \iint \sum |E_i|^2 \, dx \, dy$.

Each individual beam gets both collimated and truncated by a hexagonal microlens centered

around $(x_{f,i}, y_{f,i})$ and described by the function

$$\Pi_{L,i}(x,y) = \begin{cases} 1, & (x,y) \text{ inside the hexagon} \\ 0, & \text{else,} \end{cases} \tag{3.2}$$

so that the truncated beam is given by $E_{\mathrm{t},i} = E_i \times \Pi_{L,i}(x,y)$. It should be noted that due to this truncation, there is no overlap between the individual $E_{\mathrm{t},i}$. The sum of all the truncated beams then yields the near field

$$E_{\mathrm{NF}} = \sum E_{\mathrm{t},i} = \sum E_{0,i} \exp\left(-\frac{(x-x_{f,i})^2 + (y-y_{f,i})^2}{w_{0,i}^2} \right) \times \Pi_{L,i}(x,y), \tag{3.3}$$

which thus describes a hexagonal array of N truncated Gaussian beams as shown in fig. 3.2a. It is thus equivalent to the expression given in eq. (2.2) (section 2.2.1), and was preferred here in order to simplify the implementation in the numerical simulations.

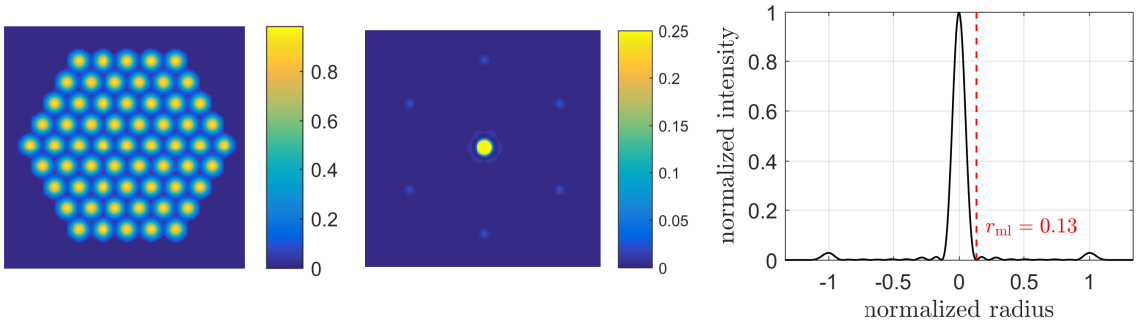

(a) Near field.

(b) Far field.

(c) Vertical lineout of the far field with r_{ml} indicating the relative position of the first minimum.

Figure 3.2: Near field and far field for $N = 61$ beams. The peak intensities have been normalized to one and the color scale in (b) has been adjusted such that the secondary lobes become visible.

Due to the microlens clipping, the overall power in this near field $P_{\mathrm{NF}} = \iint |E_{\mathrm{NF}}|^2 \, dx \, dy$ is smaller than the total power P_{tot}. In order to quantify this power loss it is convenient to define the microlens transmission

$$t_{\mu\text{-lens}} = \frac{P_{\mathrm{NF}}}{P_{\mathrm{tot}}}. \tag{3.4}$$

Although there is no direct dependence in the formula, it is intuitively clear that the microlens transmission depends on the diameter $2w_0$ of the beams at the microlens array with respect to the short diagonal d of the microlens. In the following, this ratio will be called microlens fill factor $\tau_r = 2w_0/d$.

In a next step, the near field gets Fourier transformed. This generates the far field $E_{\mathrm{FF}} = \mathcal{F}(E_{\mathrm{NF}})$, which consists of a very powerful main lobe, six secondary lobes arising due to the threefold sym-

metry of the near field, and several other, fainter lobes, as explained in section 2.2.1 and shown in fig. 3.2b. In these and all following 2D images of a 61 fiber far field, the peak intensity has been normalized to one and the maximum of the color scale has been set to 0.25, so that the side lobes become clearly visible. Figure 3.2c displays a vertical lineout of the far field, showing the relative amplitude of some of those fainter lobes close to the main lobe. The radius has been normalized with respect to the position of the secondary lobes, so that the first minimum next to the main lobe is located at $r_{\mathrm{ml}} = 0.13$.

Then, the far field gets spatially filtered by a circular aperture. This can be described by multiplication of E_{FF} with a truncating function, so that one finds for the remaining truncated field

$$E_{\mathrm{tr}}(r) = E_{\mathrm{FF}} \times \mathrm{disc}_r(x,y) \quad \text{with} \quad \mathrm{disc}_r(x,y) = \begin{cases} 1, & \sqrt{x^2+y^2} \leq r \\ 0, & \sqrt{x^2+y^2} > r, \end{cases} \tag{3.5}$$

where r is the radius of the aperture. This radius determines how much power is transmitted into the truncated field, which can be described by the truncation efficiency

$$\eta_{\mathrm{tr}}(r) = \frac{P_{\mathrm{tr}}(r)}{P_{\mathrm{FF}}}, \tag{3.6}$$

where P_{tr} is the power in the truncated field, given by $P_{\mathrm{tr}}(r) = \iint |E_{\mathrm{tr}}(r)|^2 \, dx \, dy$, and $P_{\mathrm{FF}} = \iint |E_{\mathrm{FF}}|^2 \, dx \, dy$ is the power in the far field. Figure 3.3a shows the truncation efficiency as a function of aperture radius. Obviously, the larger the aperture radius, the more energy is transmitted.

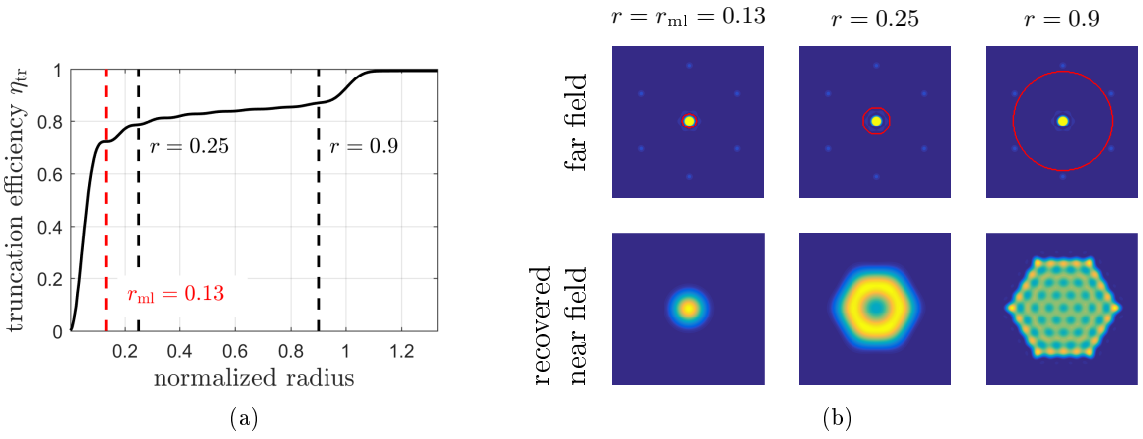

(a) (b)

Figure 3.3: (a) Truncation efficiency and (b) recovered near fields as a function of aperture radius r for $N = 61$ beams. Note that the output fields are scaled arbitrarily.

However, there is also the shape of the recovered near field E_{out} which needs to be considered. Given by the far field of the truncated field E_{tr}, it can be found by a second Fourier transform, so that $E_{\mathrm{out}} = \mathcal{F}(E_{\mathrm{tr}})$. Since the spatial filtering removes the higher spatial frequencies of E_{FF}, the recovered near field becomes more homogeneous and Gaussian-like for smaller aperture radiuses r. Indeed, if the filtering is performed at the first extinction of the far field ($r = r_{\mathrm{ml}}$), a very clean

and smooth recovered near field can be obtained (cf. left column of fig. 3.3b). For a filtering at the second extinction ($r = 0.25$ for $N = 61$ beams), the recovered near field has a donut-like shape, as can be seen in the middle column of fig. 3.3b. For larger filtering radii, E_{out} becomes more structured. Finally, for a filtering which only removes the secondary lobes, it recovers the hexagonal contour of the initial fiber array ($r = 0.9$, right column of fig. 3.3b). Considering this behavior, the truncating aperture radius has to be chosen as a function of transmitted power and desired output beam shape.

Typically, the combined beam is considered to be the main lobe of the far field. In order to calculate the combining efficiency η as defined in eq. (2.1) (section 2.1), it is thus necessary to know $P_{\text{comb}} = P_{\text{ml}}$, which can be obtained by truncating the far field at the position of its first minimum r_{ml}. Hence, $E_{\text{ml}} = E_{\text{FF}} \times \text{disc}_{r_{\text{ml}}}$, and consequently $P_{\text{ml}} = \iint |E_{\text{ml}}|^2 \, dx \, dy$. Thus,

$$\eta = \frac{P_{\text{comb}}}{P_{\text{tot}}} = \frac{P_{\text{ml}}}{P_{\text{tot}}}. \tag{3.7}$$

It should be noted that $\eta \neq \eta_{\text{tr}}(r_{\text{ml}})$, since η takes into account the microlens transmission, whereas $\eta_{\text{tr}}(r_{\text{ml}})$ does not. Hence, $\eta_{\text{tr}}(r_{\text{ml}})$ corresponds to the efficiency measured in the far field,

$$\eta_{\text{FF}} = \eta_{\text{tr}}(r_{\text{ml}}) = \frac{P_{\text{ml}}}{P_{\text{FF}}}, \tag{3.8}$$

and using eq. (3.4) and the identity $P_{\text{FF}} = P_{\text{NF}}$ it follows that

$$\eta = \eta_{\text{FF}} \times t_{\mu\text{-lens}}. \tag{3.9}$$

The next sections will describe the impact of spatial misalignments and spectral disparities on the combining efficiency η. The maximum tolerable error on the alignment or the spectral properties was defined as the value corresponding to an efficiency loss of one percentage point. As far as not otherwise mentioned, the following parameters have been used in the simulations:

- central wavelength $\lambda_0 = 1032\,\text{nm}$
- fiber pitch and microlens short diagonal $d = 3.2\,\text{mm}$
- microlens pitch $p = 3.2\,\text{mm}$
- microlens fill factor $\tau_r = 0.9$
- microlens focal length $f = 50.5\,\text{mm}$

It should be noted that the microlens focal length has not been chosen arbitrarily, but has been calculated based on the array pitch p, the microlens fill factor τ_r and the beam divergence θ at the fiber output, so that $f = \tau_r p/(2\theta)$. The beam divergence is specific to the fiber amplifier in use and is given as a function of the waist and M^2 of the beam. In our case, we have $w_0 = 15\,\mu\text{m}$ and $M^2 = 1.3$, so that it follows $\theta = M^2/w_0 = 0.0285\,\text{rad}$ and consequently $f = 50.5\,\text{mm}$. Furthermore, the beam divergence can be used to calculate the Rayleigh range of the uncollimated beam, which equals $z_R = w_0/\theta = 0.68\,\text{mm}$.

Besides, in every of the following subsections only the final equation describing a certain misalignment will be given in two dimensions. Everywhere else, the y-dimension can be found completely analogous to the x-dimension and has therefore been omitted for the sake of readability. For the same reason, also the index i has been omitted and the coordinates $((x - x_{f,i}), (y - y_{f,i}))$ have been replaced by (x, y), even if the given fields describe only one beam, and not necessarily the central one.

3.2 Microlens Fill Factor

In a first step, the combination efficiency η has been calculated as a function of the microlens fill factor τ_r. As explained in section 2.2.1, for small τ_r the microlens clipping is nearly zero, but the small beam diameter in the near field gives rise to numerous and powerful side lobes in the far field (see fig. 3.4a (top) for an example with $N = 7$ beams). This decreases the combining efficiency η. In contrast, for large τ_r, the side lobes in the far field are less prominent and there is thus a higher amount of power in the main lobe, as shown in fig. 3.4a (bottom). However, there is also more power lost due to microlens clipping. In order to find the best compromise between microlens clipping and power contained in side lobes, η has been calculated as a function of the microlens fill factor τ_r. The results for $N = 61$ beams are shown in fig. 3.4b, and are highly similar to those obtained with only seven beams. The optimal fill factor is thus given independently from the number of fibers by $\tau_r = 0.93$, and the corresponding seven-fiber fields are shown in fig. 3.4a (center). For this case, the microlens transmission is given by $t_{\mu\text{-lens}} = 0.91$ and the overall combining efficiency reaches its optimum value of $\eta_{\text{ideal}} = 0.67$.

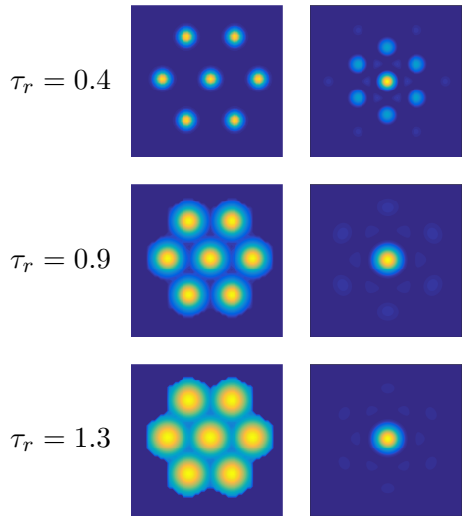

(a) (left) Near fields and (right) far fields for $N = 7$ beams and different τ_r.

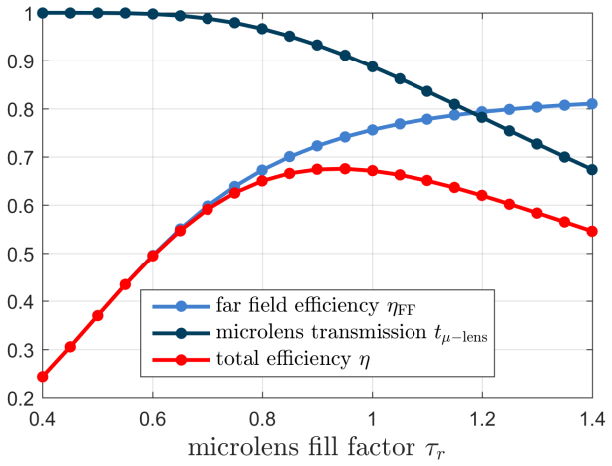

(b) Combination efficiency η as a function of microlens fill factor τ_r for $N = 61$ beams.

Figure 3.4: Microlens fill factor τ_r.

3.3 Spatial Alignment Errors

In this section, the influence of errors in the alignment of the fiber and microlens array on the coherent combination efficiency is investigated. For every misalignment, a schematic of the simulated situation and a curve showing the drop in efficiency for increasing misalignments will be presented. If applicable, the maximum tolerable alignment errors will be considered relative to the absolute value of the corresponding parameter of the fiber array.

3.3.1 Misalignments within the Fiber Array

In this part, the impact of misalignments in the fiber array is simulated. It is supposed that the alignment of each fiber is carried out as precise as possible, so that errors are randomly distributed around zero, with higher probabilities for errors closer to zero. Hence for every misalignment m the errors were simulated by drawing N random variables from a Gaussian distribution with standard deviation m and applying them as errors to the N beams. This leads to irregular intensity distributions in the far field, as exemplarily shown in fig. 3.5a for a far field calculated with 61 beams and errors on the lateral alignment of $\Delta x = 5\,\mu\text{m}$.

As every set of errors leads to slightly different far fields and corresponding combining efficiencies, 50 runs were executed for each m. The combining efficiency is then given as the mean of the 50 individual results, whereas the error bars represent their standard deviation. They indicate thus not the standard error of the mean, but rather the fluctuations of the simulated efficiencies.

Since the XCAN project aims at the coherent combining of 61 fibers, but the experiments presented in this thesis have been conducted with only seven channels, simulations have been run using both of these numbers. Figure 3.5b shows a typical efficiency curve, in gray for seven fibers and in black for 61, obtained here for errors on the lateral alignment of the fibers. It can be seen that the efficiencies themselves vary only slightly with the fiber number, which is why

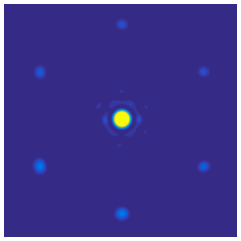

(a) Example far field for $N = 61$ beams and $\Delta x = 5\,\mu\text{m}$

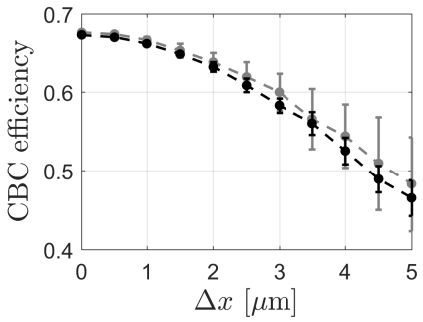

(b) Example efficiency curve for errors on the alignment of (gray) seven and (black) 61 fibers.

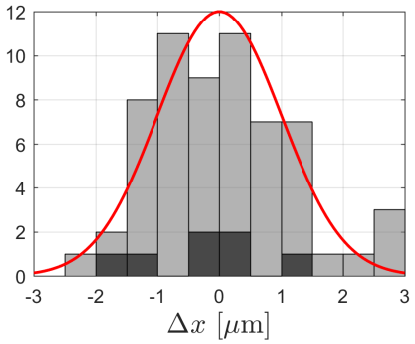

(c) (red) Gaussian probability distribution with standard deviation $\sigma = \Delta x = 1\,\mu\text{m}$ and example histograms for (gray) 61 and (black) seven random variables drawn from this distribution.

Figure 3.5

in the following only the curve for $N = 61$ beams will be shown. However, the error bars are much larger in the case of $N = 7$ beams. The reason for this is that when only seven variables are drawn, they don't necessarily reflect well the distribution they are drawn from. Hence, two different sets of errors may lead to very different efficiencies. In contrast, when 61 numbers are drawn, the different sets are more alike, since their histograms resemble much more the Gaussian distribution. This is illustrated in fig. 3.5c, where an example histogram for (gray) 61 and (black) seven random errors is shown, together with the Gaussian probability distribution they are drawn from (red line). Another way to describe this effect is to consider that in the seven fiber array, one outlying variable will impact one fiber out of seven, that is, 15 % of the total fiber number. In the case of 61 fibers, this reduces to 1.6 %. From another point of view one could say that in the 61 fiber array, there is a sort of averaging among the errors which will smooth out the impact of individual values, and which is much less important in the case of seven fibers.

It should be emphasized that the errors indicated on the x-axis of the efficiency curves are the standard deviations of the distribution from which the N errors have been drawn. This means on the one hand that about 32 % of the errors will be higher than the indicated value. For instance, in the example given in fig. 3.5c, 23 of the 61 values are larger than the indicated error of 1 µm, with three of them having more than 2.5 times its value. On the other hand, when it comes to an estimation of efficiency losses based on errors measured on the experimental setup, care has to be taken not to consider the highest measured peak-to-valley error, but rather the standard deviation of all the experimental values.

Another option consists of course in simulating the far field and thereby the combining efficiency by directly applying the measured errors to the respective beams in the model. This is interesting especially in the seven fiber setup, since in this case the combining efficiency can vary considerably for different sets of errors, as has been explained above and is also reflected in the large error bars in fig. 3.5b. Hence, calculating the combining efficiency directly with the measured errors leads to a more precise result than an estimation based on their standard deviation. In contrast, such an estimation might be adequate for a 61 fiber setup, since the simulated combining efficiencies depend much less on the actual distribution of the errors among the channels.

Especially for large errors, the central lobe of the far field may become shifted, or the minima next to it may blur out. It was therefore decided that the combining efficiency would always be calculated by considering the amount of power which is in the area of the main lobe of an ideal far field. As the far field with errors becomes more arbitrary for larger errors, the amount of power in the main lobe area varies more strongly, giving rise to larger fluctuations in the calculated efficiencies. This explains the larger standard deviations found for larger errors (cf. fig. 3.5b), even if the high number of runs per error guarantees a reliable result for the mean efficiency η.

It should be noted that for all spatial errors, the combination of the beams remains coherent. This means that the combining efficiency can even drop to zero, if the alignment errors are such that they result in a destructive interference in the area of the main lobe.

In the following, different misalignments within the fiber array will be presented independently one from another.

Fiber Tilt

If a fiber is tilted by an angle θ_x with respect to the optical axis, the collimated beam will still be parallel to the optical axis, but shifted by a distance Δx, as shown in fig. 3.6a. The final field reads then

$$E = E_0 \exp\left(-\left(\frac{(x-\Delta x)^2 + (y-\Delta y)^2}{w_0^2}\right)\right), \tag{3.10}$$

where Δx is given by $\Delta x = f \tan\theta_x$. This shifting of the beam impacts the combining efficiency in two ways: on the one hand, the microlens clipping is increased, and on the other hand the far field efficiency is reduced due to the irregularities in the hexagonal beam array.

The corresponding efficiency curves are shown in fig. 3.6b. It can be seen that the overall losses in combining efficiency are dominated by the reduced microlens transmission. In order to limit these overall efficiency losses to one percentage point, the tilts on the fibers should not exceed 2.5 mrad. This corresponds to 8.9 % of the fiber numerical aperture or the divergence of the emitted beam.

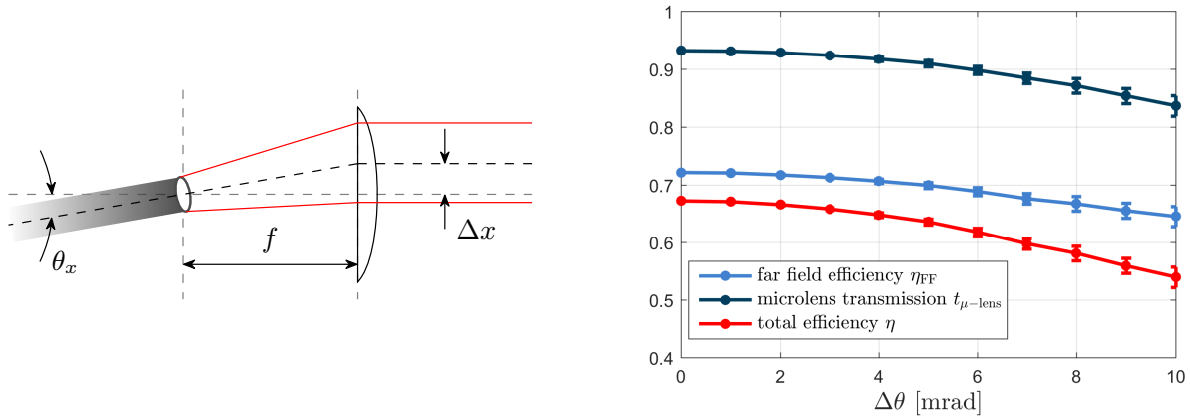

(a) Schematic of a tilted fiber

(b) Efficiency losses due to fiber tilt

Figure 3.6: Fiber tilt.

Fiber Displacement

If a fiber is placed at a distance Δx from the optical axis, the beam collimated by the microlens will be tilted by an angle θ_x (see fig. 3.7a). This corresponds to a tilt of the wavefronts and can be described in the near field by

$$E = E_0 \exp\left(-\left(\frac{(x-\Delta x)^2 + (y-\Delta y)^2}{w_0^2}\right)\right) \exp\left(-ik(x\theta_x + y\theta_y)\right), \tag{3.11}$$

where the approximation $\theta_x \approx \tan\theta_x = \frac{\Delta x}{f}$ has been used. This latter one is justified since the Δx are typically in the order of a few micrometers, whereas f equals 50.5 mm. Given the resulting curve shown in fig. 3.7b it is apparent that errors on fiber displacement should be limited to about one micrometer. This corresponds to only 0.03 % of the fiber pitch and is therefore one of the

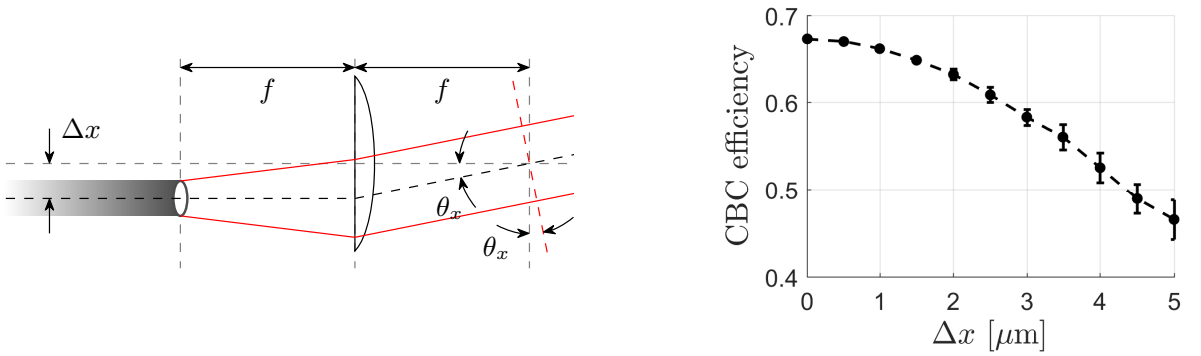

(a) Schematic of fiber displacement.

(b) Efficiency losses due to fiber dispalcement

Figure 3.7: Fiber displacement.

most critical parameters in the setup.

Due to these very small tolerable errors, the microlens clipping remains almost unchanged by fiber displacements. The losses in combining efficiency are therefore largely dominated by the tilted wavefronts of the collimated beams.

Focal Errors

If the fiber is placed on the optical axis at a distance Δf from the focal point of the microlens, the beam will not be collimated anymore, but rather focused at a distance s' from the microlens, as shown in fig. 3.8a and 3.8b for positive and negative Δf, respectively. These distances are related by the thin lens equation*, given by

$$\frac{1}{f} = \frac{1}{s} + \frac{1}{s'} = \frac{1}{f+\Delta f} + \frac{1}{s'} \quad \Leftrightarrow \quad s' = \frac{f(f+\Delta f)}{f+\Delta f - f} = \frac{f^2}{\Delta f} + f. \tag{3.12}$$

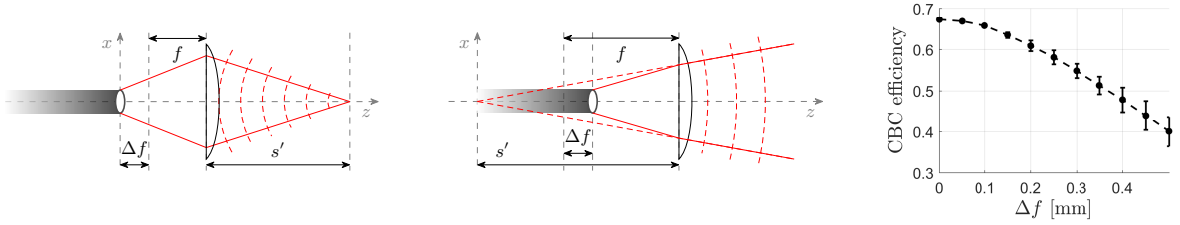

(a) Schematic of focal error with $\Delta f > 0$.

(b) Schematic of focal error with $\Delta f < 0$.

(c) Efficiency losses due to errors on focal distances

Figure 3.8: Focal errors.

*Strictly speaking, one has to consider the position s of the waist of a Gaussian beam in front of the thin lens and the one behind it (s'). These are related by $s'/f - 1 = \frac{s/f-1}{(s/f-1)^2+(z_R/f)^2}$ [22]. In our case, $z_R \approx 0.7\,\text{mm}$ and $f = 50.5\,\text{mm}$, meaning that z_R/f can be neglected. Writing furthermore $s - f = \Delta f$, the previous equation simplifies to $s'/f - 1 = f/\Delta f$, which is equivalent to the expression given in eq. (3.12).

Such an error on the focal distance results in spherical wavefronts with radius r converging towards the point $z = s'$. In the plane of the microlenses, the resulting curved wavefront can be described by

$$r^2 = x^2 + z^2 \Leftrightarrow z(x, \Delta f) = \begin{cases} r + \sqrt{r^2 - x^2}, & \Delta f < 0 \\ r - \sqrt{r^2 - x^2}, & \Delta f > 0, \end{cases} \tag{3.13}$$

where $r = s' = \frac{f^2}{\Delta f} + f$.

This curved wavefront translates into a phase term, so that the final expression for the field of the beams reads

$$E = E_0 \exp\left(-\left(\frac{x^2 + y^2}{w_0^2}\right)\right) \exp\left(-ikz(x, y, \Delta f)\right), \tag{3.14}$$

and the resulting drop in efficiency is shown in fig. 3.8c. As can be deduced from the curve, errors in the focal distance should not exceed 0.08 mm, which is 0.15 % of the microlens focal length and 12 % of the Rayleigh range of the beam.

One might argue that an error on the focal distance changes the beam size on the microlens array, and thereby the microlens transmission. This is certainly true, however, it can be shown* that the relative change in beam radius caused by the maximum focal errors applied in fig. 3.8c does not exceed 1 %, which translates directly to a relative change of the microlens fill factor of 1 %. This implies that the losses due to an altered microlens fill factor are negligible, especially with respect to the efficiency drop already caused by the spatial phase mismatches.

Output Power

There might be differences in the output power of the different fiber amplifiers, resulting in power differences in the near field as illustrated in fig. 3.9a.

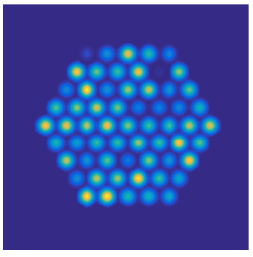

(a) Example of a near field with $\Delta P_0 = 0.5$.

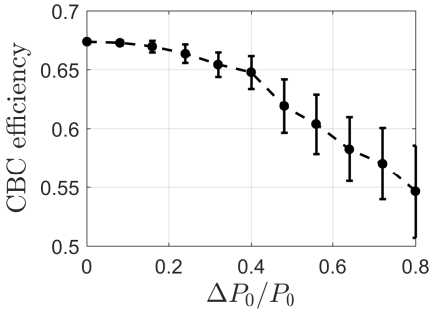

(b) Efficiency losses due to disparities in output power.

Figure 3.9: Output power.

*The beam radius at the microlens array $w(z)$ is the width of a Gaussian beam, $w(z) = w_0\sqrt{1 + (z/z_R)^2} \approx w_0 z/z_R$. The difference in beam radius $\Delta w(z)$ resulting from a difference in z is thus given by $\Delta w(z) = w_0 \Delta z/z_R = w(z)\Delta z/z$. For $\Delta z = \Delta f = 0.5$ mm and $z = f = 50$ mm this yields $\Delta w(z)/w(z) = \Delta z/z = 0.01$. Furthermore, since the microlens fill factor is given by $\tau_r = 2w(z)/d$, it follows that $\Delta\tau_r = 2\Delta w(z)/d = 2w(z)/d \times \Delta z/z = \tau_r \Delta z/z$, which means that τ_r changes in the same way as $w(z)$.

In order to model these disparities, the power amplitude P_0 was normalized to one, and errors ΔP_0 have been added. However, especially for large ΔP_0 there is a certain risk that a negative total amplitude $P_0 + \Delta P_0 < 0$ is found. Since such an amplitude has no physical meaning, it was set to zero whenever this case occurred. Finally, the amplitude of the electric field E_0 is related to the power amplitude by $E_0 = \sqrt{P_0 + \Delta P_0}$, so that one finds for the Gaussian beam

$$E = \begin{cases} \sqrt{P_0 + \Delta P_0} \exp\left(-\left(\frac{x^2+y^2}{w_0^2}\right)\right), & P_0 + \Delta P_0 > 0 \\ 0, \text{ else.} \end{cases} \tag{3.15}$$

It should be noted that after applying these errors the total power P_{tot} might be higher than the one of the ideal case with $E_0 = 1$. The overall power in the main lobe of the far field P_{ml} might therefore also be higher than in the ideal case. However, since the combining efficiency is given as the ratio of those two, the extra power will have no impact on η.

The resulting efficiency curve is shown in fig. 3.9b and indicates that power differences of up to 25 % from the nominal value are acceptable.

Polarization

The combined beam is polarized along $\vec{p}$, which is the mean of the polarizations of all individual beams. Hence, if a a beam is polarized along a vector $\vec{p}\,'$ that is turned by an angle θ with respect to the mean polarization direction, only the projection of $\vec{p}\,'$ on $\vec{p}$ can be considered for the coherent combination, as illustrated in fig. 3.10a. The amplitude of the beam is thus reduced by a factor $p'_x = |\vec{p}\cos\theta|$, so that

$$E = p'_x \exp\left(-\left(\frac{x^2+y^2}{w_0^2}\right)\right). \tag{3.16}$$

This expression resembles the one given above for disparities in the output power. However, the

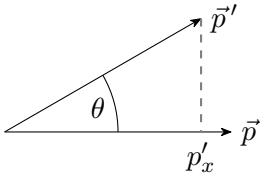

(a) Schematic of a polarization vector which is turned by an angle θ with respect to the main polarization $\vec{p}$, and its projection on $\vec{p}$.

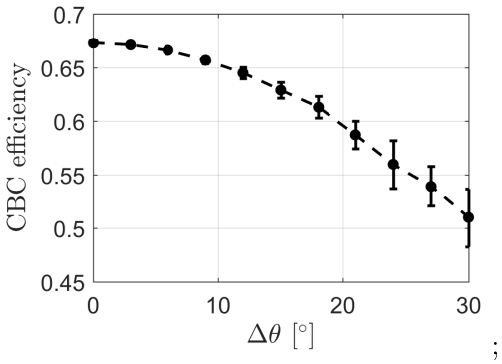

(b) Efficiency losses due to differences in polarization.

Figure 3.10: Beam polarization.

main difference between these two cases is that for mismatched output powers, the total power emitted by the fiber amplifiers is transmitted to the far field, and losses in combining efficiency are solely due to power disparities. In contrast, in the case of polarization mismatches, a part of the emitted power is lost in the orthogonal polarization direction. Hence, in this case the decrease in combining efficiency is due to both an overall power loss and power disparities in the remaining near field.

The corresponding efficiency curve is shown in fig. 3.10b and suggests that polarization disparities should be limited to $\Delta\theta = 7°$.

Beam Ellipticity

Typically, the output mode of the PCF fiber used in the experiments is not exactly circular. Therefore it was studied at which point a beam ellipticity might impact the combining efficiency.

An elliptic beam can be modeled by decomposing the beam waist w_0 into its components in x- and y-direction and by multiplying them with an ellipticity constant ϵ, so that one finds $w_x = \epsilon w_0$ and $w_y = w_0/\epsilon$. In this way the area of the beam $A = \pi w_x w_y = \pi w_0^2$ and thus its relative power stay constant, and the expression for the Gaussian beam reads

$$E = E_0 \exp\left(-\frac{x^2}{w_x^2} - \frac{y^2}{w_y^2}\right). \tag{3.17}$$

In a first step it was supposed that all beams exhibit the same ellipticity ϵ. Two example near fields corresponding to this case are shown in fig. 3.11a (top left and right) for $\epsilon = 0.6$ and $\epsilon = 1.4$, respectively. As consequence of such elliptic beams, the microlens clipping is reduced on the short diagonal of the beam ellipse, but increased on the long one. Since the microlenses have a hexagonal shape, the clipping will be less important if the long diagonal of the ellipse is oriented

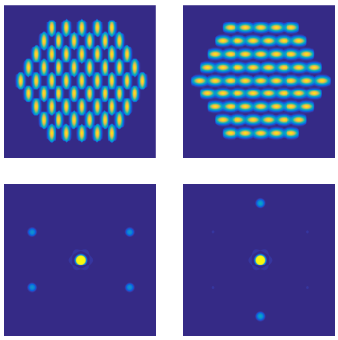

(a) (top) Near fields and (bottom) far fields for an ellipticity of (left) $\epsilon = 0.6$ and (right) $\epsilon = 1.4$ common to all beams. The color scale of the far fields is the same as in fig. 3.2b.

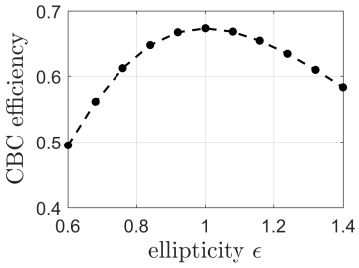

(b) Efficiency losses due to an ellipticity common to all beams.

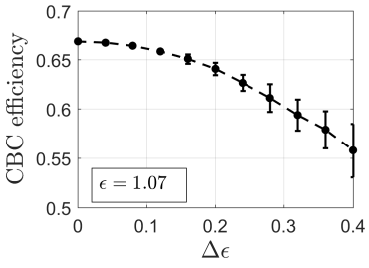

(c) Efficiency losses due to random errors on the ellipticity of each beam, where a global ellipticity of $\epsilon = 1.07$ was applied.

Figure 3.11: Beam ellipticity.

parallel to the long diagonal of the hexagon.

Furthermore, due to the elliptic beam shape in the near field, the envelope of the far field becomes asymmetric as well, and somehow squeezed in the direction of the long diagonal of the ellipse. This results in a suppression of the side lobes of the far field in this direction, as can be seen in fig. 3.11a (bottom left and right). Due to this asymmetric behavior, the related losses in combining efficiency are less important in the case where the long diagonal of the beam ellipse is oriented parallel to the long diagonal of the hexagonal aperture of the microlens, which corresponds to $\epsilon > 0$. Hence, in the experimental setup, the fibers should be aligned accordingly.

In a next step, variations in the ellipticity were applied, so that $w_x = (\epsilon + \Delta\epsilon)w_0$. In order to stay close to the experimental situation, the measured mean ellipticity $\epsilon = 1.07$ was added to each beam. The corresponding efficiency curve is shown in fig. 3.11c and indicates that differences in ellipticity of up to $\Delta\epsilon = 0.12$ won't strongly impact the combination efficiency.

3.3.2 Microlens Array Misalignments

In this section, the impact of a misalignment of the microlens array on the combining efficiency will be studied. Since there is only one microlens array, each error needs to be applied only once, so that there is no need for a statistic approach as presented in the previous section. This is also why there are no error bars on the efficiency curves.

For each error one or two example far fields will be presented. However, those are for illustrative purposes only, as the errors applied in each case largely exceed the acceptable range. They were chosen in order to show the general effect of such an error on the far field. As explained in section 3.1 (page 44), the peak intensity of the far fields has been normalized to one and the color axis adjusted such that the side lobes become clearly visible.

Besides, it should be noted that any misalignment of the microlens array results in a change in the position and/or the shape of the truncating mask $\Pi_L(x, y)$ which gives rise to an enhanced microlens clipping. However, it has be seen in the section before that in the case of a displacement between each fiber and its respective microlens, already random errors of some micrometers cause a considerable drop in combining efficiency. In this section, the errors will be common to all microlenses. Nevertheless, it will be seen that the tolerable errors on the microlens array positioning remain on the order of several micrometers. Hence, efficiency losses caused by an enhanced microlens clipping due to a microlens array displacement can be neglected. In contrast, if the clipping is due to a tilt of the microlens array, its influence on the combining efficiency will have to be discussed.

Microlens Displacement

A displacement of the microlens array in x- or y-direction is described by the same geometry as a displacement of a fiber, but with all of the fibers being subject to one and the same displacement (see fig. 3.12a). Thus, the mathematical description does not change with respect to section 3.3.1, leading to losses in efficiency as shown in fig. 3.12b. Furthermore, the curves for a displacement in x- or y-direction are exactly the same. From these curves one can deduce that the microlens

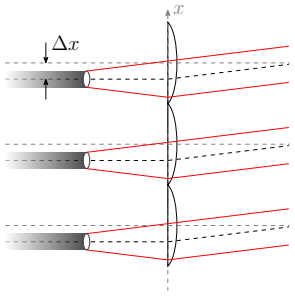

(a) Schematic of a displaced microlens array.

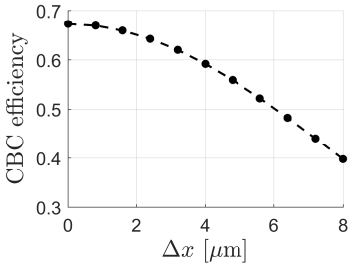

(b) Efficiency losses due to microlens displacement in x- or y-direction.

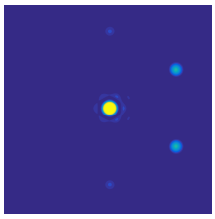

(c) Far field for a displacement of 4 µm in x-direction

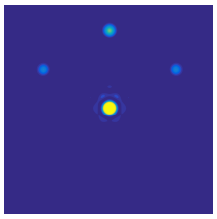

(d) Far field for a displacement of 4 µm in y-direction

Figure 3.12: Microlens displacement.

displacement should not exceed 1.4 µm in either direction, which is 0.04 % of the array pitch.

As consequence of such a displacement, the envelope of the far field gets shifted in x- or y-direction, as shown in fig. 3.12c and 3.12d for a displacement of 4 µm in x- and y-direction, respectively.

Microlens Rotation

A rotation of the microlens array corresponds to a displacement of the fibers in x- and y-direction, where the distances from the ideal position Δx_{rot} are given as a function of the rotation angle φ_{rot}, yielding

$$\Delta x_{\mathrm{rot}} = x_f(1 - \cos\varphi_{\mathrm{rot}}) - y_f(1 - \sin\varphi_{\mathrm{rot}}) \tag{3.18}$$

$$\Delta y_{\mathrm{rot}} = x_f(1 - \sin\varphi_{\mathrm{rot}}) + y_f(1 - \cos\varphi_{\mathrm{rot}}), \tag{3.19}$$

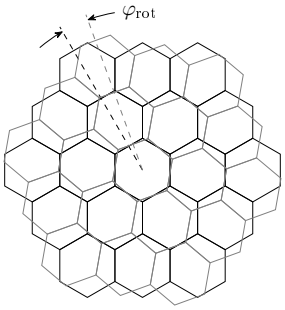

(a) Illustration of microlens rotation.

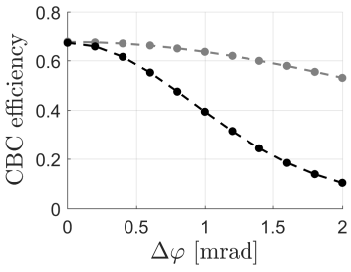

(b) Efficiency losses due to a rotation of the microlens array for an array of (black) 61 and (gray) 7 fibers

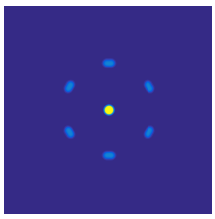

(c) Far field resulting from a rotation of 1 mrad

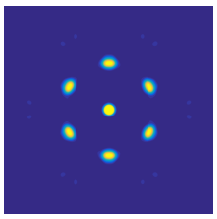

(d) Far field resulting from a rotation of 1.7 mrad

Figure 3.13: Microlens rotation.

where x_f if the position of the fiber. Thus, the expression for the Gaussian beam reads

$$E = E_0 \exp\left(-\left(\frac{(x-\Delta x_{\text{rot}})^2 + (y-\Delta y_{\text{rot}})^2}{w_0^2}\right)\right) \exp\left(-ik(x\theta_{x_{\text{rot}}} + y\theta_{y_{\text{rot}}})\right) \tag{3.20}$$

where $\theta_{x_{\text{rot}}} = \frac{\Delta x_{\text{rot}}}{f}$. This leads to a sort of smearing of the side lobes, as if the far field was spun around the central lobe, as shown in fig. 3.13c and 3.13d for a rotation of 1 mrad and 1.7 mrad, respectively.

As can be seen in fig. 3.13a, the displacement between the fiber and the corresponding microlens gets larger with increasing distance from the center of the array. It is thus not surprising that the impact of a rotation of the microlens array is much more violent for a 61 fiber array than for one containing only seven fibers. The two corresponding curves are shown in fig. 3.13b in black and gray, respectively. It follows that for 61 fibers the rotation has to be as precise as 0.16 mrad, whereas for the downscaled version of seven fibers, 0.5 mrad are still acceptable.

Microlens Pitch

Just as for the microlens rotation, a difference between the pitch p of the microlens array and the pitch d of the fiber array results in a displacement of each fiber which respect to the center of the corresponding microlens. If the difference in pitch is given by $\Delta p = p - d$, then the displacement can be described by $\Delta p_{\text{tot}} = \frac{x_l}{p}\Delta p$, where x_l is the center of the microlens. This results in a wavefront tilted by an angle $\theta_{x_l} = \frac{\Delta p_{\text{tot}}}{f} = \frac{x_l}{p}\frac{\Delta p}{f}$, as shown by the dotted lines in fig. 3.14a. If the far field is modeled with these tilted wavefronts, the impact of a pitch difference on the combining efficiency is very high, as shown in fig. 3.14b (top), yielding a far field as shown in fig. 3.14c (top).

However, if the phase offsets between the individual beams are well adjusted, one obtains an overall segmented wavefront as shown by the dashed lines in fig. 3.14a, which can be approximated by a parabola (solid line). Such a wavefront can be easily compensated in an experiment by adjusting the distances of the subsequent imaging lenses.

A mathematical description can be derived by considering that the slope θ_{x_l} of the wavefronts increases linearly with x_l. Hence, the parabolic wavefront z can be calculated by generalization of θ_{x_l} to all x and subsequent integration,

$$z = \int \theta_x \, dx = \int \frac{\Delta p}{pf} x \, dx = \frac{1}{2}\frac{\Delta p}{pf} x^2. \tag{3.21}$$

The individual wavefront segments z_l are then given by the tangents on this parabola in the points x_l, so that

$$z_l = \frac{\Delta p}{pf} x_l (x - \frac{1}{2} x_l). \tag{3.22}$$

If these two are well matched, only a small residual parabolic phase remains on each beam, given by

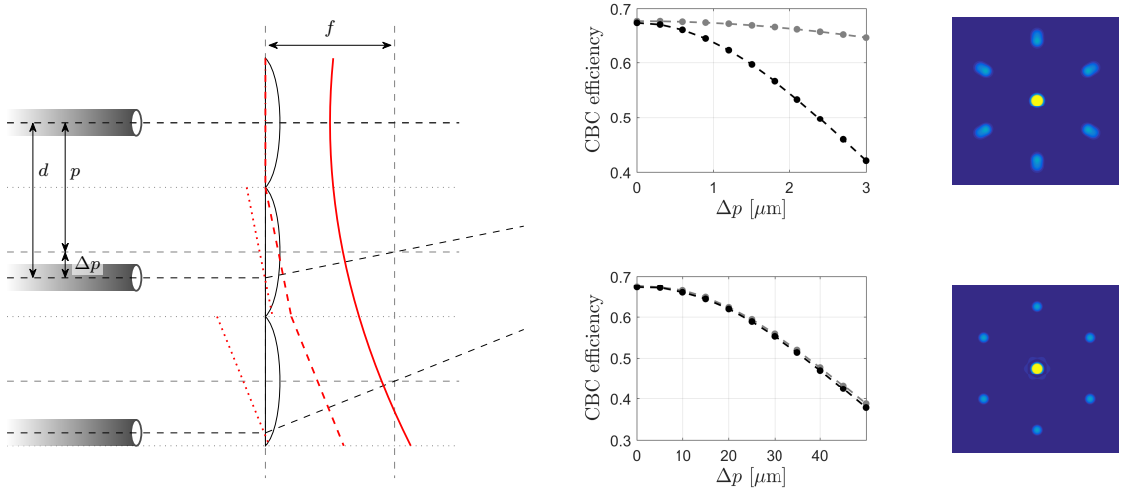

(a) Schematic illustrating a pitch difference between the fiber and microlens array. The dotted red lines are the individual wavefronts, which can be approximated and partially compentated for by a parabolic phase (solid line) after suitable phase offset compensation (dashed lines).

(b) Efficiency losses due to a pitch difference for an array of (black) 61 and (gray) 7 fibers, (top) without and (bottom) with correction of second order phase. Note the different scaling of the x-axis.

(c) Far fields (top) without and (bottom) with correction of second order phase for $\Delta p = 3.5\,\mu\text{m}$ and $40\,\mu\text{m}$, respectively.

Figure 3.14: Microlens pitch.

$$\varphi_{\text{res}} = k(z - z_l) = \frac{\pi}{\lambda}\frac{\Delta p}{pf}(x - x_l)^2, \tag{3.23}$$

and leading to a small defocalization of each individual beam. This explains the excess of power in the side lobes of the corresponding far field (fig. 3.14c (bottom)) which are typically an indication of a defocalization. The resulting losses in combining efficiency are shown in fig. 3.14b (bottom). They are by more than a factor of ten less sensitive than in the case without compensation, and independent of the number of fibers. This latter one is due to the fact that after the compensation of the overall second order phase, the phase of each individual beam does not depend anymore on the distance of the beam from the microlens center. Therefore, there is no reason that beams closer to the edges of the hexagon are impacted stronger by the difference in pitch. Nevertheless, this difference should be kept below 9.5 µm in order to limit the efficiency losses to one percentage point. Although this implies that the outmost fibers are shifted by almost 40 µm with respect to their microlenses, the efficiency losses due to an enhanced microlens clipping are still largely inferior to those induced by the parabolic wavefronts of the beams.

The maximum tolerable pitch difference of 9.5 µm corresponds to 0.3 % of the microlens array pitch and highlights again the high precision which is necessary on both the fiber and the microlens array, so that a perfect match between the two can be achieved.

Microlens Focal Distance

An error in the focal distance of the microlens array is described by the same equations as an error on a single fiber, only that all fibers are subject to the same error (see fig. 3.15a). As consequence of a focal error, the side lobes of the far field become more prominent, as shown in fig. 3.15c and 3.15d for an error in focal distance of 0.6 mm and 1.0 mm, respectively. As for a focal error of a single fiber, the change in microlens fill factor due to a change in the focal distance and the corresponding losses in combining efficiency are negligible (cf. section 3.3.1 on page 52). The curve shown in fig. 3.15b indicates that the error on the focal distance of the microlens array should not exceed 0.13 mm, which corresponds to 0.25 % of its focal length, and to 19 % of the beam's Rayleigh range.

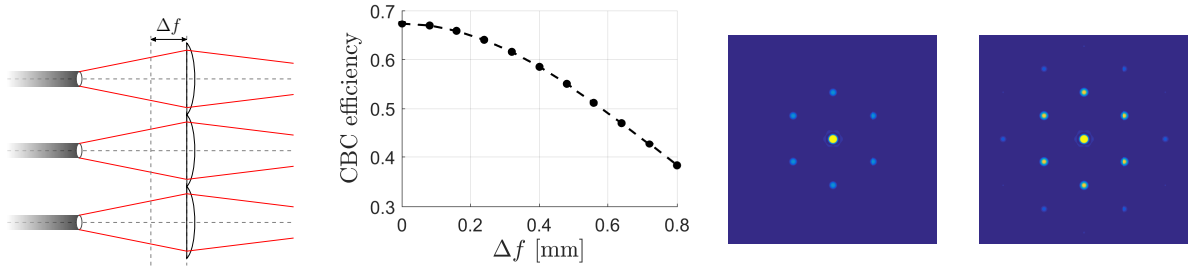

(a) Schematic of an error in the focal distance of the microlens array.

(b) Efficiency losses due to an error in the focal distance of the microlens array

(c) Far field resulting from a focal error of $\Delta f = 0.6\,\mathrm{mm}$

(d) Far field resulting from a focal error of $\Delta f = 1.0\,\mathrm{mm}$

Figure 3.15: Microlens focal distance.

Microlens Tilt

A schematic of a tilted microlens array is shown in fig. 3.16a. It can be described as a combination of a displacement between the fibers and their respective lenses, an error on the focal distances, and a tilt of each single microlens. While this latter one does not impact the phase of the beam, it has to be taken into account that the beams are not clipped by the original hexagonal shape of the lenses $\Pi_L(x)$, but rather by its projection on the x-axis, given by $\Pi_{L_x}(x) = \Pi_L(x)\cos\vartheta_x$, where ϑ_x is the tilt angle. Furthermore, each lens gets shifted by a distance $\Delta x = x_f(1-\cos\vartheta_x)$ with respect to the fiber position, which also enhances the microlens clipping. However, even for the largest tilt angles ϑ_x used in the simualations, the calculated microlens transmissions remain almost constant, which implies that the losses in combining efficiency are largely dominated by the displacements and the altered focal distances between the fibers and their respective microlenses.

Those focal distances Δf depend on the position of the fiber and can be described by

$$\Delta f = x_f \tan\vartheta_x. \tag{3.24}$$

Inserting this term into eq. (3.13) yields the parabolic phase $z(x, y, \Delta f)$ which has to be added to the Gaussian beam.

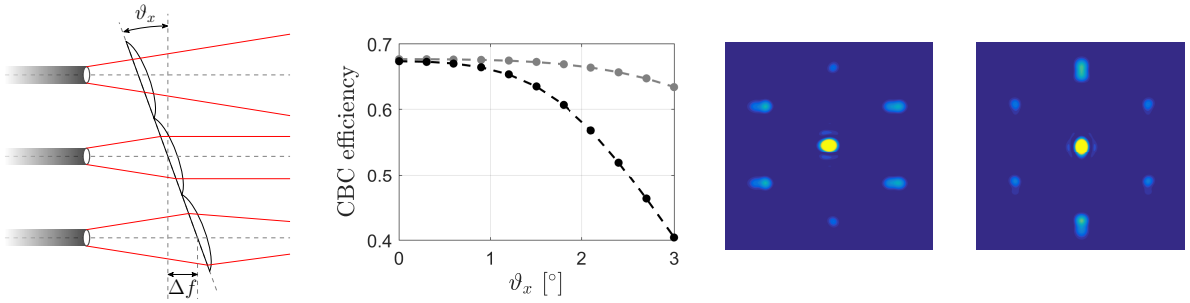

(a) Schematic of a tilted microlens array.

(b) Efficiency losses due to microlens tilt in x- or y-direction for an array of (black) 61 and (gray) 7 fibers.

(c) Far field resulting from a tilt of 3° in x-direction

(d) Far field resulting from a tilt of 3° in y-direction

Figure 3.16: Microlens tilt.

Furthermore, the wavefront tilt angle θ_x induced by the relative displacement between fibers and microlenses can be deduced from geometrical considerations and is given by

$$\theta_x = \frac{\Delta x}{f + \Delta f} = \frac{x_f(1 - \cos\vartheta_x)}{f + \Delta f}, \tag{3.25}$$

with the Δf derived above. Finally, the expression for a beam including all phase terms reads

$$E = E_0 \exp\left(-\left(\frac{x^2 + y^2}{w_0^2}\right)\right) \exp\left(-ik(x\theta_x + y\theta_y + z(x, y, \Delta f))\right). \tag{3.26}$$

A tilt on the microlenses in one direction will somehow squeeze the far field in this direction, as is shown in fig. 3.16c and 3.16d for a tilt of 3° in x- and y-direction, respectively. Just as for the microlens displacement, there are nearly no differences between the efficiency losses related to a tilt along the one or the other axis.

However, as for the rotation of the microlens array, the tilt also becomes more important with the distance from the array center, and is thus more critical for larger fiber arrays. This can also be seen in the curve given in fig. 3.16b which implies that for a seven fiber array, tilts of up to 2° are acceptable, whereas they should be limited to 1° for the final setup of 61 fibers.

Gap Between Lenses

Due to constraints in the manufacturing of the microlens array, there is a small gap g between the individual lenses where no light is collected. This results in an enhanced beam clipping at the microlens array, so that the microlens transmission gets reduced and the beam diameter in the near field decreases. This leads to an increase of power both in the side lobes of the far field and at its borders. An example near field with a gap of $g = 800\,\mu\text{m}$ between the lenses is shown in fig. 3.17a, and leads to a far field with strongly increased side lobes as depicted in fig. 3.17b. Figure 3.17c shows the corresponding losses in microlens transmission $t_{\mu\text{-lens}}$, far field efficiency η_{FF} and overall efficiency $\eta = \eta_{\text{FF}} \times t_{\mu\text{-lens}}$.

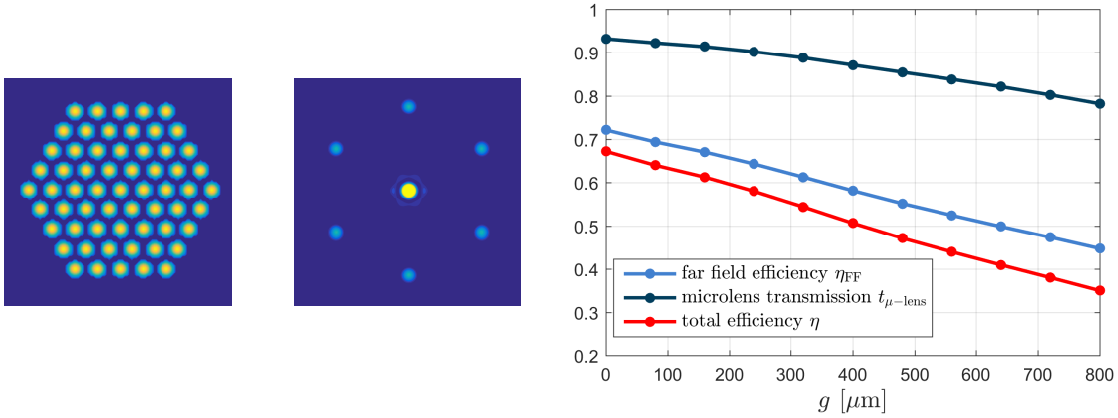

(a) Example near field with $g = 800\,\mu\mathrm{m}$.

(b) Corresponding far field.

(c) Efficiency losses due to a gap between the microlenses.

Figure 3.17: Gap between the microlenses.

From this efficiency curve it can be concluded that the gap should not exceed 30 µm, which corresponds to 0.9 % of the microlens pitch. However, according to the datasheet of the microlens array used in the experiments, a gap between 100 µm and 200 µm has to be expected, which would lead to efficiency losses between 3.5 % and 7.5 %.

3.3.3 Summary

In this section, the influence of various errors in the spatial alignment of the fiber and the microlens array on the coherent combining efficiency have been modeled. An overview of the maximum error tolerances is given in table 3.1. As far as comparable, these results are in good agreement with previously published error tolerances for coherent beam combining in filled aperture configuration [49].

Furthermore, a statement about the criticality of the misalignments is given, that is, how difficult it will be to meet the stated precisions in the experimental setup. The fiber and microlens mounts which have been implemented in the final laser system in order to comply with these spatial requirements will be presented in detail in section 4.3.

The most critical error is a relative displacement between the fibers and their corresponding microlenses, which has to be controlled on a micrometer scale. Mismatches on the tilts, and focal distances and polarizations of the individual beams also have an impact, but are less critical. Finally, the acceptable errors on beam ellipticity and power differences are so high that they largely exceed any error likely to be present in an actual experimental setup. Therefore, they need to be considered only marginally when setting up the experiment.

However, it should be kept in mind that the given error tolerances have been calculated by applying only one error at a time. In reality, the errors will occur all at the same time, thus influencing one another. For instance, if a focal error Δf is added to a fiber displacement Δx, the wavefront will be tilted by an angle $\theta'_x = \Delta x/(f + \Delta f)$ rather than by the angle $\theta_x = \Delta x/f$

criterion	maximum absolute error	maximum relative error	criticality
fiber displacement	1 µm	0.03 %	high
fiber tilt	2.5 mrad	8.9 %	medium
focal errors	0.08 mm	12 %	medium
beam polarization	7°	-	medium
beam ellipticity	0.12	-	low
output power	25 %	-	low
microlens rotation	0.16 mrad	-	high
microlens pitch	10 µm	0.3 %	high
microlens gap	30 µm	0.9 %	high
microlens displacement	1.4 µm	0.04 %	medium
microlens focal	0.13 mm	19 %	medium
microlens tilt	1°	-	medium

Table 3.1: Recapitulation of the modeled misalignments, their maximum tolerable errors if efficiency losses shall be limited to one percentage point, and how critical they will be in the alignment.

used in the simulation of the fiber displacement. Hence, the efficiencies will change.

Moreover, all the simulations presented here were performed using a microlens fill factor of $\tau_r = 0.9$. For different fill factors, the efficiencies vary slightly. For instance, the losses found for a tilted fiber are mainly due to an enhanced microlens clipping. Hence, for a lower τ_r and thus smaller beams, the tilts can be higher before the microlens clipping becomes important. This is of particular interest since in the experimental setup, a fill factor of only $\tau_r = 0.7$ has been measured. An efficiency curve using this value has been calculated, but remains quite close to the one based on $\tau_r = 0.9$, and has therefore not been shown. In the same way, the impact of a gap between the microlenses decreases for lower fill factors. Indeed, for the experimental fill factor of $\tau_r = 0.7$, a gap of up to 60 µm can be tolerated.

3.4 Spectral Disparities

Since the experiments are conducted with femtosecond pulses, the spectral properties of the beams may influence the combining efficiency. In order to estimate the losses in efficiency due to disparities in the spectral amplitude or phase of the pulses, eq. (3.1) was expanded in the spectral dimension, so that the electric field of each beam becomes

$$E(x, y, \omega) = E(x, y)E(\omega), \tag{3.27}$$

where $E(\omega) = A(\omega - \omega_0)e^{i\varphi(\omega)}$ as in section 1.1.1.

Since there is no interference between the different wavelengths of the spectrum, the observed far field can be considered as the incoherent superposition of the far fields of every incremental wavelength. Thus, the power P of an electric field E is given by $P = \iiint |E(x, y, \omega)|^2 \, d\omega \, dx \, dy$, and the combining efficiency can be calculated using the same formula as in eq. (3.7).

3.4.1 Spectral Envelope

The spectral envelope $A(\omega - \omega_0)$ might not be exactly the same for all of the beams. However, as each frequency increment is considered independently from the others, mismatches in spectral envelope translate into power discrepancies among the beams. Since it has been seen in section 3.3.1 that those do not have a strong impact on the combining efficiency, spectral envelope mismatches have not been studied in more detail.

3.4.2 Spectral Phase

Considering additionally the spectral phase, the electric field reads

$$E = E(x, y)A(\omega - \omega_0) \times e^{i\varphi(\omega)}. \tag{3.28}$$

As detailed in section 1.1.1, the spectral phase can be developed in a Taylor series, where the different coefficients correspond to a phase offset (φ_0), a delay (φ_1), a group delay dispersion and therefore a frequency chirp (φ_2), and a third order dispersion (φ_3). This allows to separate E into four independent electric fields, each describing one separate term of the spectral phase,

$$E_{\varphi_0} = E(x, y)A(\Delta\omega) \times \exp(i\varphi_0) \tag{3.29}$$

$$E_{\varphi_1} = E(x, y)A(\Delta\omega) \times \exp(i\varphi_1\Delta\omega) \tag{3.30}$$

$$E_{\varphi_2} = E(x, y)A(\Delta\omega) \times \exp\left(i\frac{\varphi_2}{2}\Delta\omega^2\right) \tag{3.31}$$

$$E_{\varphi_3} = E(x, y)A(\Delta\omega) \times \exp\left(i\frac{\varphi_3}{6}\Delta\omega^3\right). \tag{3.32}$$

Furthermore, the nonlinear phase φ_{NL} can simply be expressed as

$$E_{\varphi_{\mathrm{NL}}} = E(x, y)A(t) \times \exp(i\varphi_{\mathrm{NL}}(t)), \tag{3.33}$$

where $A(t) = \mathcal{F}(A(\Delta\omega))$ is the amplitude of the pulse in the time domain.

If all beams had the same spectral phase, this would have no impact on the combining efficiency. However, there may be differences in the spectral phases of the individual beams, which give rise to a transfer of power from the main lobe to a speckle pattern around it. Since this speckle is removed at the spatial filtering pinhole, the power in the combined beam is reduced with respect to the overall output power, and the combining efficiency decreases.

The impact of the different spectral phase terms on the combining efficiency η was studied in the same way as it has been done for the spatial errors. Hence, for each phase coefficient 50 runs have been executed, each using a set of random errors drawn from a Gaussian distribution with standard deviation $\Delta\varphi_n$. The efficiency curves show the mean value and the standard deviation of the 50 efficiency values that were calculated, in black for the average power and in gray for the peak power, as explained below.

3.4.2.1 General Considerations

As mentioned before, the overall power in the far field can be considered as the sum of the powers contained in the far fields of each incremental frequency. However, except for the zeroth order, the spectral phase grows with $\Delta\omega$, so that frequencies close to the center of the spectrum are less heavily impacted by the spectral phase than those at the edges. In consequence, for these latter frequencies the phase differences between the individual beams are higher, so that the far fields become more arbitrary, with less power concentrated in the main lobe and more in a speckle pattern around it. This behavior is shown in fig. 3.18 for three different wavelengths for beams with a Gaussian spectral envelope, a pulse duration of $\Delta t \approx 225\,\mathrm{fs}$ and a first order phase of $\Delta\varphi_1 = 250\,\mathrm{fs}$. This phase has been chosen much higher than any value that could be expected in real experiments, in order to clearly show the general behavior of the far field under the influence of spectral phases. It should also be noted that the first wavelength corresponds to the central one and exhibits therefore an ideal far field.

In the following, different consequences resulting from this frequency dependence will be presented. As above, the phases used in all the examples are highly exaggerated in order to give an instructive illustration of the effect in question.

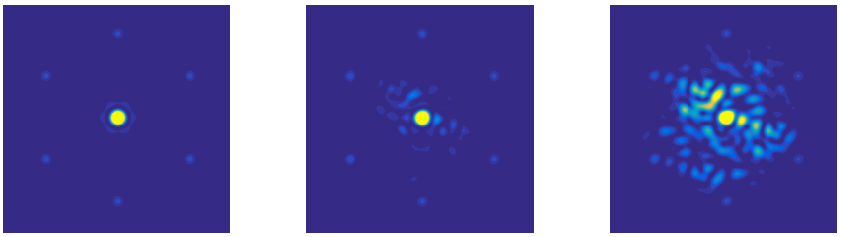

(a) $\lambda = 1032\,\mathrm{nm}$ (b) $\lambda = 1033.5\,\mathrm{nm}$ (c) $\lambda = 1035\,\mathrm{nm}$

Figure 3.18: Example far fields for three different wavelengths from the center of the spectrum to its edge, calculated with a Gaussian spectral envelope and first order phase of $\Delta\varphi_1 = 250\,\mathrm{fs}$.

Inhomogeneous Spectral Content of the Far Field

For small spectral phase coefficients, the phase differences between the central and the edge frequencies may remain below 2π. In this case, there is a clear relation between the phase of each incremental frequency, so that the corresponding far fields resemble each other, only that the speckle pattern becomes more pronounced for the larger spectral phases belonging to the frequencies at the edge of the spectrum. In contrast, for large phase coefficients, the phase difference between two frequency components largely exceed 2π, so that each frequency exhibits a far field which is not related to those of the other frequencies, and has its own individual speckle pattern. This implies that different frequencies have different intensities at different locations in the far field, so that the spectral content of the far field is spatially inhomogeneous.

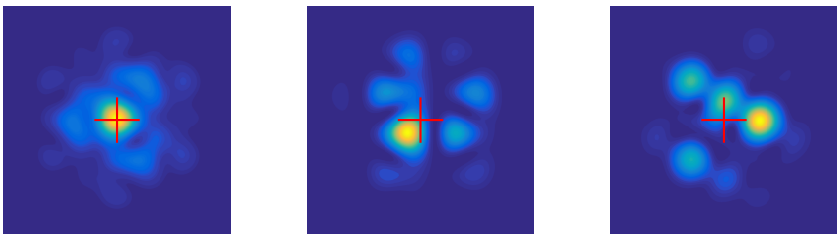

(a) Overall far field. (b) $\lambda = 1038\,\mathrm{nm}$ (c) $\lambda = 1040\,\mathrm{nm}$

Figure 3.19: Inhomogeneous spectral content of the far field for large phase coefficients. The red plus marks the position of the main lobe of the overall far field.

This is illustrated in fig. 3.19 which shows in fig. 3.19a an example seven fiber far field calculated with a phase coefficient of $\Delta\varphi_2 = 1 \times 10^5\,\mathrm{fs}^2$, corresponding to fiber length differences of 5 m. Figure 3.19b depicts the far field calculated for a wavelength of $\lambda = 1038\,\mathrm{nm}$, where the intensity maximum is clearly shifted below and to the left of the position of the main lobe. Hence, wavelengths around 1038 nm can be found at this shifted position, but are very faint in the main lobe. In contrast, at a different wavelength of $\lambda = 1040\,\mathrm{nm}$, the intensity maximum is located to the right of the main lobe, as can be seen in fig. 3.19c. This means that this wavelength appears mostly at another position in the far field than the wavelength considered before, which confirms the spatial variations of the spectral content of the far field.

In conclusion, the tiled aperture configuration gives rise to spatio-temporal inhomogeneities in the far field.

Impact of the Spectral Envelope

Since the combining efficiency is defined as the amount of power in the area of the main lobe of an ideal far field, the frequency-dependent increase of the speckle pattern in the far field implies that frequencies at the edges of the spectrum give rise to a stronger decrease in combining efficiency than those at the center. In consequence, the spectral shape of the pulses has an impact on this efficiency. For instance, by comparing a Gaussian spectrum $|A_G(\Delta\omega)|^2 = \exp\left(-\frac{(\Delta\omega)^2}{\delta\omega^2}\right)$ and a super-Gaussian one with the same intensity FWHM and $|A_{sG}(\Delta\omega)|^2 = \exp\left(-\frac{(\Delta\omega)^4}{\delta\omega^4}\right)$, as shown

in fig. 3.20a, one can observe that for the super-Gaussian spectrum the relative amplitude of frequencies close to the center of the spectrum is increased, whereas it is strongly reduced at the wings. Hence, for the super-Gaussian spectrum the impact of the frequencies at the edges of the spectrum on the combining efficiency is reduced as well, resulting in higher overall efficiencies. This is illustrated in fig. 3.20b which shows curves for losses in average power efficiency due to disparities in the second order spectral phase, calculated with both the Gaussian and the super-Gaussian spectra defined above.

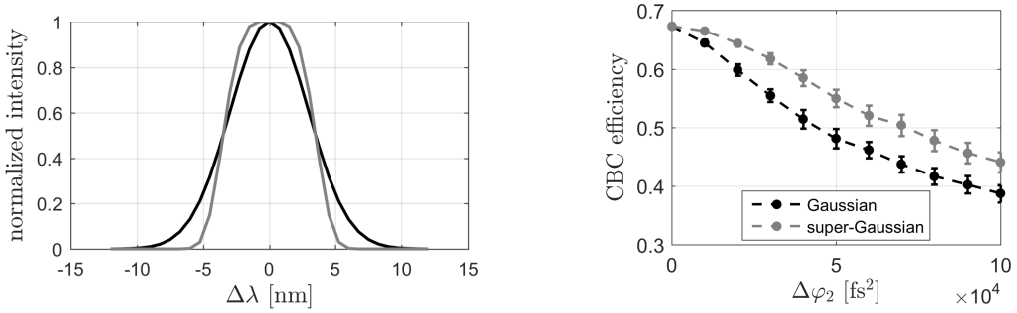

(a) (black) Gaussian and (gray) super-Gaussian spectrum with the same intensity FWHM.

(b) Corresponding efficiency curves.

Figure 3.20: Impact of the spectral envelope on the combining efficiency.

However, it should be noted that the combining efficiency obtained with the super-Gaussian spectrum highly depends on its width. In the case presented here, the Gaussian and the super-Gaussian spectrum have the same intensity FWHM. As can be seen in fig. 3.20a, this means that the reduction of intensity at the edges of the super-Gaussian spectrum is somewhat stronger than the increase near the center. This could be easily changed by normalizing the spectra to another parameter, for instance their energy. The corresponding super-Gaussian spectrum would then be broader than the one presented here, resulting in a reduced combining efficiency.

The impact of the spectral shape on the combining efficiency is increased in the case where a nonlinear phase is considered in combination with a CPA configuration, so that the spectral phase is directly proportional to the power spectrum of the pulses. In this case, a super-Gaussian spectrum implies a nonlinear phase which is approximately constant over the central frequency region, and can therefore be corrected by the feedback algorithm. Hence, the losses in combining efficiency are strongly reduced.

Peak Power Losses

Due to the increasing speckle pattern in the far field (cf. fig. 3.18), an increasing amount of power is lost at the spatial filtering pinhole (cf. fig. 3.1 on page 43) for frequencies at the edge of the spectrum. Hence, the contribution to the power of the spatially filtered combined beam is decreased for these frequencies. The resulting spectrum of the combined beam $P_{\mathrm{spec}}(\omega) = \iint |E_{\mathrm{tr}}(x, y, \omega)|^2 \, dx \, dy$ is thus narrower than the initial one, as shown by the black

line in fig. 3.21a for a combined beam where arbitrary phases drawn from a Gaussian distribution with $\Delta\varphi_1 = 250\,\mathrm{fs}$ were applied. For comparison, the gray line shows the spectrum of an ideal combined beam without spectral phases, which remains unaffected by the spatial filtering. This spectral narrowing implies that the Fourier transform limited temporal pulse profile $P_{\mathrm{spec}}(t) = |\mathcal{F}(\sqrt{P_{\mathrm{spec}}(\omega)})|^2$ gets broadened with respect to the one of the initial pulse, as is illustrated in fig. 3.21b showing the temporal profiles corresponding to the spectra of fig. 3.21a.

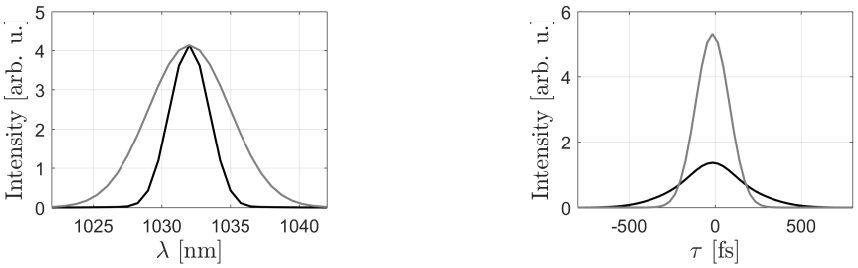

(a) Spectra (b) Temporal profiles

Figure 3.21: Example (a) spectra and (b) temporal pulse profiles of (gray) an ideal combined beam and (black) a combined beam exhibiting a spectral phase of $\Delta\varphi_1 = 250\,\mathrm{fs}$.

This implies that there are not only losses in the average power of the combined pulse, but additionally that its peak power gets reduced due to the temporal broadening. This decrease can be calculated by comparing the peak power of the combined and compressed pulse $P_{\mathrm{peak}} = P_{\mathrm{spec}}(t=0)$* with the ideal peak power $P_{\mathrm{peak,\,ideal}}$, so that the peak power efficiency η_{peak} is given by

$$\eta_{\mathrm{peak}} = \frac{P_{\mathrm{peak}}}{P_{\mathrm{peak,\,ideal}}} \times \eta_{\mathrm{ideal}}, \tag{3.34}$$

with η_{ideal} as defined in section 3.2.

Asymptotic Behavior for Very Large Phase Mismatches

It should be noted that disparities among the spectral phases destroy the coherence between the beams. For example, in the extreme case where the relative delay between the pulses becomes larger than the pulse duration, the pulses arrive one after the other and can thus not interfere. Hence, the resulting far field is just the incoherent superposition of all the beams. However, the combining efficiency is still defined as the amount of power confined in the area of the main lobe of an ideal far field, so that even an incoherently combined beam exhibits a certain non-zero combining efficiency η_{inc}. Since spectral phases cause incoherence, but can not lead to destructive interference, combining efficiencies below η_{inc} are not possible. However, η_{inc} depends on the size of the near field and therefore the number of beams, since for larger beam numbers the size of the main lobe of the far field decreases with respect to the size of the incoherently combined beam, as shown in fig. 3.22. In consequence, for $N = 7$ beams, the efficiency will not drop below

*This definition is slightly different from the one given in section 1.1. However, we are interested in the ratio between two peak powers, for which both definitions yield the same results.

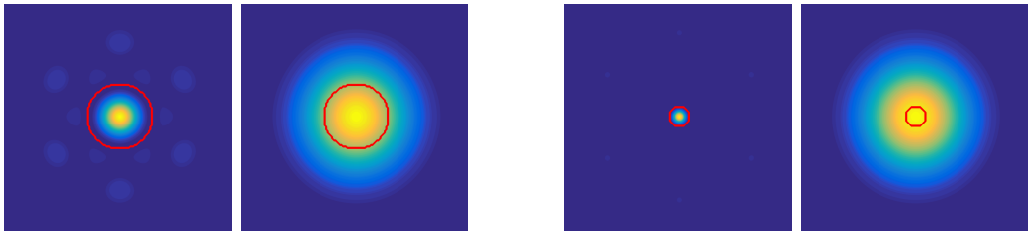

(a) (b)

Figure 3.22: (left tiles) Area of the main lobe for ideally combined beams, and (right tiles) corresponding area for incoherently combined beams, for (a) seven and (b) 61 beams. The ratio between the power contained in the red circles of the incoherently combined beams and the overall power of these beams defines the lower limit of the combining efficiency.

$\eta_{\mathrm{inc}} = 38\,\%$, whereas it can decrease to $\eta_{\mathrm{inc}} = 4\,\%$ in the case of $N = 61$ fibers.

This can be generalized by considering that η_{inc} is roughly proportional to the area of the main lobe of the far field $A_{\mathrm{ml}} \propto \frac{1}{(N_D/2)^2}$, where N_D is the normalized diameter of the near field as defined in section 2.2.1. By substituting $N_D^2 = (4N-1)/3$ one obtains $A_{\mathrm{ml}} \propto 12/(4N-1) \to 3/N$ $(N \to \infty)$, which means that η_{inc} decreases first steeply and tends then slowly towards zero. This implies that also the requirements on the matching of the spectral phase increase considerably when the fiber number is increased from a very low to a higher value, as is the case in the examples above. However, for already very large N, the changes flatten out.

Furthermore it should be kept in mind that these incoherent efficiencies represent an asymptotic behavior found in extreme cases for very large spectral disparities. In any real CBC setup, the combining efficiency still depends on N, but the spectral mismatches need to be limited to values which can be considered as small perturbations of an ideal system.

3.4.2.2 Modeled Efficiency Curves

In the following, the decrease in combining efficiency due to disparities among the different components of the spectral phase will be modeled both for the average and the peak power of the combined beam. As for the spatial misalignments, the maximum tolerable error is set to a loss of one percentage point in average power combining efficiency.

The beams are supposed to have a Gaussian spectral envelope

$$A_G(\Delta\omega) = \exp\left(-\frac{(\Delta\omega)^2}{2\delta\omega^2}\right), \tag{3.35}$$

whose width $\delta\omega$ is related to the intensity FWHM wavelength λ_{FWHM} and the central wavelength λ_0 by

$$\delta\omega = \frac{\pi c}{\sqrt{\ln 2}} \frac{\lambda_{\mathrm{FWHM}}}{\lambda_0^2}. \tag{3.36}$$

We assume $\lambda_{\mathrm{FWHM}} = 7\,\mathrm{nm}$. The corresponding pulse length is given by $\Delta t = 2\sqrt{\ln 2}/\delta\omega = 223\,\mathrm{fs}$, which corresponds well to the experimental pulse width of 216 fs retrieved from autocorrelation

measurements on the combined beam (see section 4.5.5 for more detail).

Phase Offset φ_0

The results for a difference in phase offset are shown in fig. 3.23. It can be observed that the distribution of phase offsets should not exceed $\pi/19\,\mathrm{rad}$ or $\lambda/38\,\mathrm{RMS}$ in case of CBC of seven fibers, and $\pi/24\,\mathrm{rad}$ or $\lambda/48\,\mathrm{RMS}$ in case of 61 fibers.

In an experiment, phase fluctuations will be introduced by any kind of acoustic, mechanical or, on a longer timescale, thermal noise. The feedback algorithm used for the coherent combination has thus to be able to correct for all these noises in order to reduce the phase fluctuations on a single fiber to values below $\lambda/48\,\mathrm{rms}$.

Delay φ_1

Intuitively it is easy to understand that the pulses of all the channels need to arrive at the same time if they shall recombine coherently. However, small delays between the pulses are acceptable, as can be seen in the efficiency curves in fig. 3.24. This implies that the delays should be limited to about 35 fs for a seven fiber setup and 22 fs for a 61 fiber setup, which corresponds to an optical path difference of 10.5 µm or 6.6 µm, respectively. This result may be generalized by considering the delay of 35 fs or 22 fs with respect to the pulse duration of about 223 fs, so that the errors on the delays should not be significantly higher than 15 % of the pulse duration in the seven fiber setup, and 10 % in the 61 fiber setup.

Group Delay Dispersion φ_2

The second order phase is induced by the dispersion of the fiber medium. It can therefore be expressed as a difference in fiber length, as indicated in the top axis of the efficiency curves shown in fig. 3.25. It can be seen that the differences in φ_2 should not exceed $7500\,\mathrm{fs}^2$ for seven fibers and $5000\,\mathrm{fs}^2$ for 61 fibers, which corresponds to a relative error of $\Delta\varphi_2/\Delta t^2 = 0.15$ or 0.1, respectively, and a difference in fiber length of 37.5 cm or 25 cm.

Third Order Dispersion φ_3

As the group delay dispersion, the third order dispersion (TOD) is related to beam propagation in a medium. The resulting efficiency curves are shown in fig. 3.26, and imply that the acceptable difference in fiber length is on the order of 32 m for seven fibers and 20 m for 61 fibers. Since this is much larger than the $\sim 30\,\mathrm{cm}$ required for the matching of the GDD, no special care has to be taken for the TOD adjustment.

Higher Order Dispersions $\varphi_4, \ldots$

Since already the third order dispersion is not critical for the combining efficiency, no higher order dispersions have been modeled.

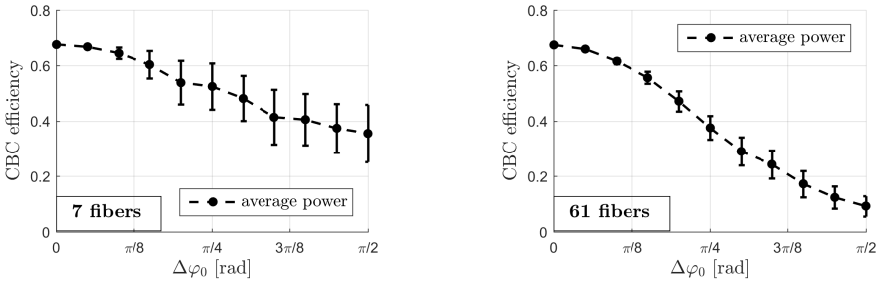

(a) Seven fibers. (b) 61 fibers.

Figure 3.23: Phase offset $\Delta\varphi_0$.

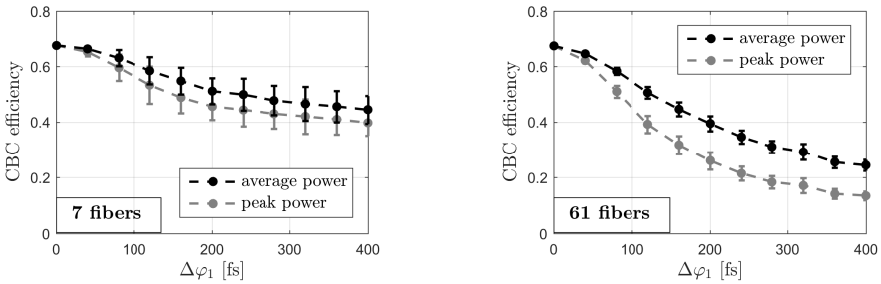

(a) Seven fibers. (b) 61 fibers.

Figure 3.24: Delay $\Delta\varphi_1$.

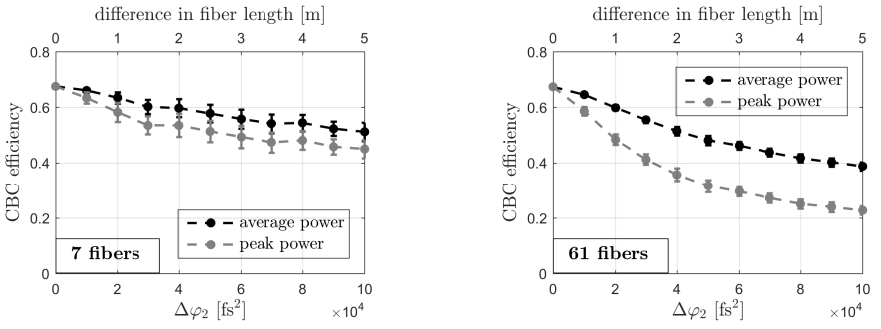

(a) Seven fibers. (b) 61 fibers.

Figure 3.25: Group delay dispersion $\Delta\varphi_2$.

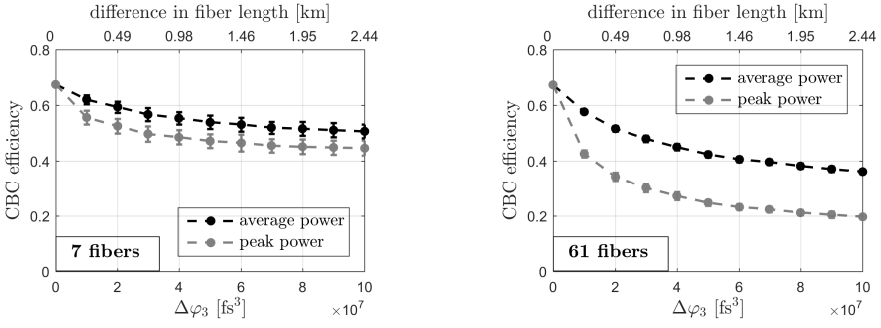

(a) Seven fibers. (b) 61 fibers.

Figure 3.26: Third order dispersion $\Delta\varphi_3$.

Nonlinear Phase φ_{NL}

Last but not least, the beams can exhibit a nonlinear phase

$$\varphi_{\mathrm{NL}} = k \int n_2 I(z,t)\, dz = \gamma_{\mathrm{NL}} \int P(z,t)\, dz \tag{3.37}$$

as introduced in section 1.1.2. This expression can be simplified by separating $P(z,t)$ into a spatial and a normalized temporal part, so that $P(z,t) = P_{\mathrm{peak}}(z)P_{\mathrm{spec}}(t)$, and

$$\varphi_{\mathrm{NL}}(t) = \gamma_{\mathrm{NL}} \int P(z,t)\, dz = P_{\mathrm{spec}}(t) \times \gamma_{\mathrm{NL}} \int P_{\mathrm{peak}}(z)\, dz = P_{\mathrm{spec}}(t) \times B. \tag{3.38}$$

Inserting this phase in the general expression of a beam exhibiting a nonlinear phase given in eq. (3.33) yields

$$E_{\varphi_{\mathrm{NL}}}(x,y,t) = E(x,y)A(t) \times \exp\left(iP_{\mathrm{spec}}(t)B\right). \tag{3.39}$$

Furthermore, as the pulses are subject to a strong temporal stretching in a CPA setup, the temporal pulse profile exhibits the same shape as the spectral one. It is therefore possible to substitute $A(t)$ by $A(\Delta\omega)$ and $P_{\mathrm{spec}}(t)$ by $P_{\mathrm{spec}}(\Delta\omega) = |A(\Delta\omega)|^2$, where the correspondence between t and $\Delta\omega$ is given by $\Delta\omega(t) = t/\varphi_2$, as detailed in section 1.1.1.

Hence, the nonlinear phase can be expressed as $\varphi_{\mathrm{NL}} = B \times |A(\Delta\omega)|^2$, and the overall field of one beam becomes

$$E_{\varphi_{\mathrm{NL}}}(x,y,\omega) = E(x,y)A(\Delta\omega) \times \exp\left(iB|A(\Delta\omega)|^2\right). \tag{3.40}$$

Assuming that all beams exhibit the same spectrum, differences in nonlinear phase are solely caused by disparities among the B-integrals of the beams. Those can arise due to differences in the amplification conditions, such as slight mismatches in amplifier length or variations in pump or seed signal power.

Since global phase offsets have no impact on the combining efficiency, the overall B-integral of the beams has been neglected in the simulations, and only variations ΔB have been considered*. However, it should be kept in mind that negative B-integrals have no physical meaning. Hence, if a relative difference of $\Delta B = 1$ is applied to the beams, this implies that the absolute B-integral is high enough to tolerate such differences. From a more application-oriented point of view, one could also say that a relative difference of $\Delta B = 1$ is not very probable for an absolute B-integral of, for instance, $B = 1.5\,\mathrm{rad}$, since this would imply that one beam has a B-integral of $0.5\,\mathrm{rad}$, whereas for another beam one may find $B = 2.5\,\mathrm{rad}$. Such values are unlikely to be obtained under normal experimental conditions, especially when an effort is made to equalize the B-integrals of the different beams.

Furthermore, it should be noted that in the experiments ΔB is expected to increase with growing B. This is due to the fact that for an increasing amount of nonlinearities the behavior of

*Simulations taking into account different absolute values of B have been presented in [73]. Since the calculated losses in combining efficiency remain independent of B, these results confirm that only ΔB needs to be considered.

each amplifier becomes more sensitive to its exact working conditions, so that differences among the channels become more pronounced. Hence, even if the absolute value of B has no impact on the combining efficiency, for increasing B-integral a decrease in combining efficiency has to be expected due to increasing ΔB.

The spectrum of the beams is supposed to be Gaussian as defined in eq. (3.35). Nevertheless, assuming that phases of order zero and one are corrected by the feedback algorithm and the delay adjustment procedure, their contributions have to be removed from the nonlinear phase. Hence, in eq. (3.40) $|A(\Delta\omega)|^2$ has to be replaced by $P'_{\text{spec}}(\Delta\omega) = |A(\Delta\omega)|^2 - 1 - \frac{\partial|A(\Delta\omega)|^2}{\partial\omega}\Delta\omega$. However, for the special case of the symmetric spectrum used in these simulations, $\frac{\partial|A(\Delta\omega)|^2}{\partial\omega} = 0$, so that $P'_{\text{spec}}(\Delta\omega)$ simplifies to $P'_{\text{spec}}(\Delta\omega) = |A(\Delta\omega)|^2 - 1$. The final electric field used in the simulations reads thus

$$E_{\varphi_{\text{NL}}}(x, y, \Delta\omega) = E(x, y)A(\Delta\omega) \times \exp(iP'_{\text{spec}}(\Delta\omega)\Delta B). \tag{3.41}$$

The corresponding efficiency curves are shown in fig. 3.27. For seven fibers, the differences in B-integral should be limited to $\Delta B = 0.46\,\text{rad}$, whereas for 61 fibers, $\Delta B = 0.32\,\text{rad}$ should not be exceeded.

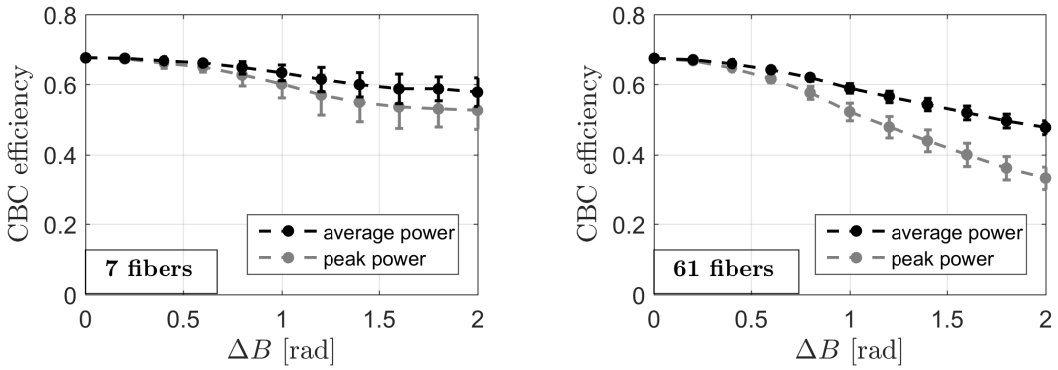

(a) Seven fibers.

(b) 61 fibers.

Figure 3.27: Nonliner phase $\Delta\varphi_{\text{NL}} = \Delta B$.

3.4.3 Summary

In this section it was modeled at which point the combining efficiency is affected by disparities in the spectral properties of the beams. A summary of the results obtained for the average power is shown in table 3.2.

In the literature, similar simulations for CBC in tiled aperture configuration are restricted to losses in peak power efficiency, but show results comparable to the ones obtained here [50, 74]. Furthermore, the tolerances stated in [49] for the phase and delay mismatches in filled aperture configurations are in good agreement with the average power efficiencies given in the table below.

Especially a phase offset and a delay between the pulses prove to be very critical and will have to be controlled precisely in the experiments. This will be done using the procedures detailed in

criterion	maximum absolute error		maximum relative error		criticality
	7 fibers	61 fibers	7 fibers	61 fibers	
phase offset φ_0 [rad]	$\pi/19$	$\pi/24$	-	-	high
delay φ_1 [fs]	35	22	16 %	10 %	high
group delay dispersion φ_2 [fs^2]	7500	5000	15 %	10 %	low
higher order dispersions	high	high	-	-	low
nonlinear phase [rad]	0.46	0.32	-	-	medium/high (depending on B)

Table 3.2: Recapitulation of the modeled spectral phase disparities, their maximum tolerances if efficiency losses in average power shall be limited to one percentage point, and how critical they will be in the alignment.

section 2.2.2, and the devices presented in section 4.1. In contrast, dispersions of an order of two or higher and differences in the B-integrals will probably not pose major problems.

3.5 Conclusion

In this chapter, a numerical model was developed which gives a complete description of the hexagonal fiber and microlens array used for the coherent beam combining.

This allowed first of all to estimate the impact of misalignments in these two arrays and of spectral disparities among the beams on the combining efficiency. It was calculated which errors on the alignment are acceptable if the efficiency should not drop by more than one percentage point. These maximum tolerances will have to be taken into account when it comes to the design of the experimental setup. The solutions which have been found in order to meet these requirements are presented in the next chapter.

Furthermore, this model also allows to simulate the experimental beam array by taking into account the measured misalignments. It is thus a valuable tool for evaluating the impact of each of these misalignments on the combining efficiency, and to estimate the maximum efficiency which can be expected in the experiments.

4 Seven Fiber Laser System

In this chapter, the setup and characterization of a tiled aperture CBC system consisting of seven high power fiber amplifiers is presented. It is the predecessor of the 61 fiber setup aimed for in the XCAN project, and has been implemented in order to identify and overcome a variety of technical and scientific challenges which might occur in the upscaled version of 61 fibers. Hence, the setup presented here is designed such that it is suitable to accommodate all 61 amplifiers, and is therefore partly overdimensioned for only seven channels.

Figure 4.1: Schematic of the three main parts of the seven fiber laser system.

The laser system can be divided into three main parts (cf. fig. 4.1), which will be described in this chapter. In the front end, the initial laser pulses are prepared for the coherent combining and the power amplification, and are then power amplified. The following section describes measures which were taken in order to characterize and reduce the passive phase noise in this front end. A third section introduces the next part of the seven fiber laser system, the laser head, which is the mechanical structure that allows to obtain a hexagonal array of collimated beams. Next, the laser back end is presented, where the coherent beam combining, the spatial filtering and the temporal recompression take place. Finally, the performances of the system are characterized both in linear and nonlinear working regimes.

4.1 Laser Front End

A schematic of our laser front end is shown in fig. 4.2, and a photo of it is displayed in fig. 4.3. The front end has to meet several requirements:

First, it needs to prepare the initial laser pulse sequence for power amplification. This includes temporal and spectral broadening of the pulses, reduction of the pulse repetition rate by pulse picking, and shaping of the spectral phase in order to guarantee best recompressibility. Furthermore, the whole front end has to be designed such that its B-integral is minimized. In fig. 4.2, the parts belonging to the amplification are colored in different shades of blue, whereas the pulse pickers are yellow and the phase shaping components exhibit a red color gradient.

Second, the front end is used to prepare the pulses for the coherent combination. This means that the initial laser beam has to be split into eight sub-beams (seven for the CBC and one as reference beam for the phase measurement), and the optical path lengths of these sub-beams have to me matched. Furthermore, the real time phase correction takes also place in the front end. Elements belonging to this domain are colored in green in fig. 4.2.

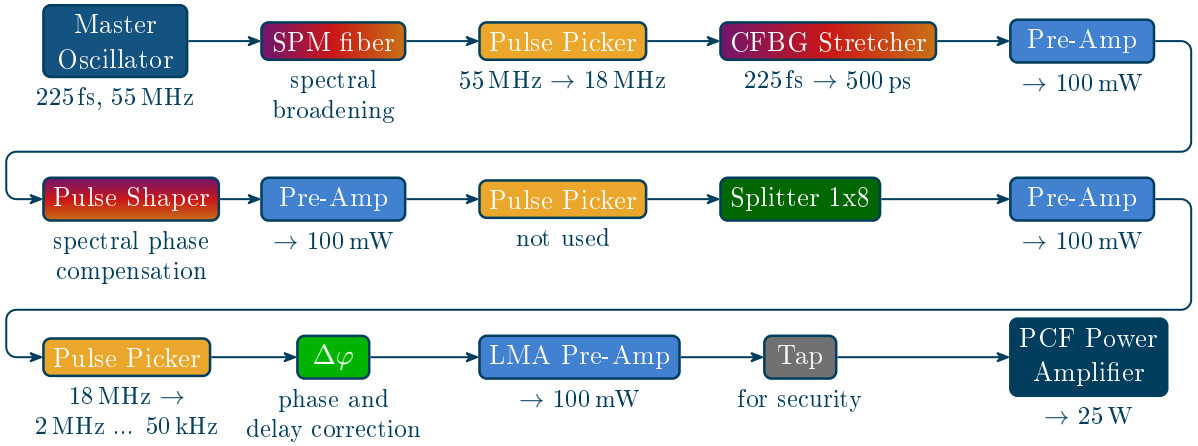

Figure 4.2: Schematic of the front end of our laser system.

Third, the front end should be fail-safe, robust, easy to maintain, and convenient to use. Therefore, we designed an all-PM-single-mode-fiber front end using off-the-shelf parts wherever possible. Moreover, in order to ensure an easy path length adjustment, the fiber lengths of all parallel components were meant to be matched to ±1 cm.

Finally, our front end is intended to be as similar as possible to the one which will be used in the 61 fiber setup. This means that any elements which might be critical in the 61 fiber setup have been included in the seven fiber one, even if they were overdimensioned for this case, or if their use complicated the setup. This concerns in particular the pulse picking system and the number of pre-amplifiers which were included in the front end, as will be explained below.

In the following, the individual parts of the front end will be presented in more detail.

Pulse Generation and Temporal Stretching

The master oscillator is a Mikan from Amplitude Systèmes delivering 225 fs pulses at a repetition rate of 55 MHz. In a first step, these pulses are passed through a 3 m long fiber, so that the pulse spectrum gets broadened due to self-phase modulation. This allows to pre-compensate the spectral gain narrowing induced by subsequent amplification stages.

Afterwards, a first pulse picker can be used to reduce the pulse repetition rate, as will be described in more detail below. Subsequently, a chirped fiber Bragg grating (CFBG) stretcher from Teraxion is used to increase the pulse duration to 500 ps. This stretcher was designed such that it pre-compensates the overall spectral phase induced by both the GVD in the all-fiber front end and the fixed geometry of the grating compressor.

The pulse duration in the seven fiber setup is by a factor of ten smaller than the 5 ns aimed for in the 61 fiber setup. It was chosen as a preliminary set point, since the 5 ns compressor was not available in time, whereas a much more compact 500 ps compressor could be readily provided. In consequence, in order to keep the overall B-integral at the level of about 5 rad aimed for in the 61 fiber setup, the pulse repetition rate had to be increased by a factor of ten from the initial 200 kHz to 2 MHz, so that the pulse energy is decreased by this same factor of ten and the peak

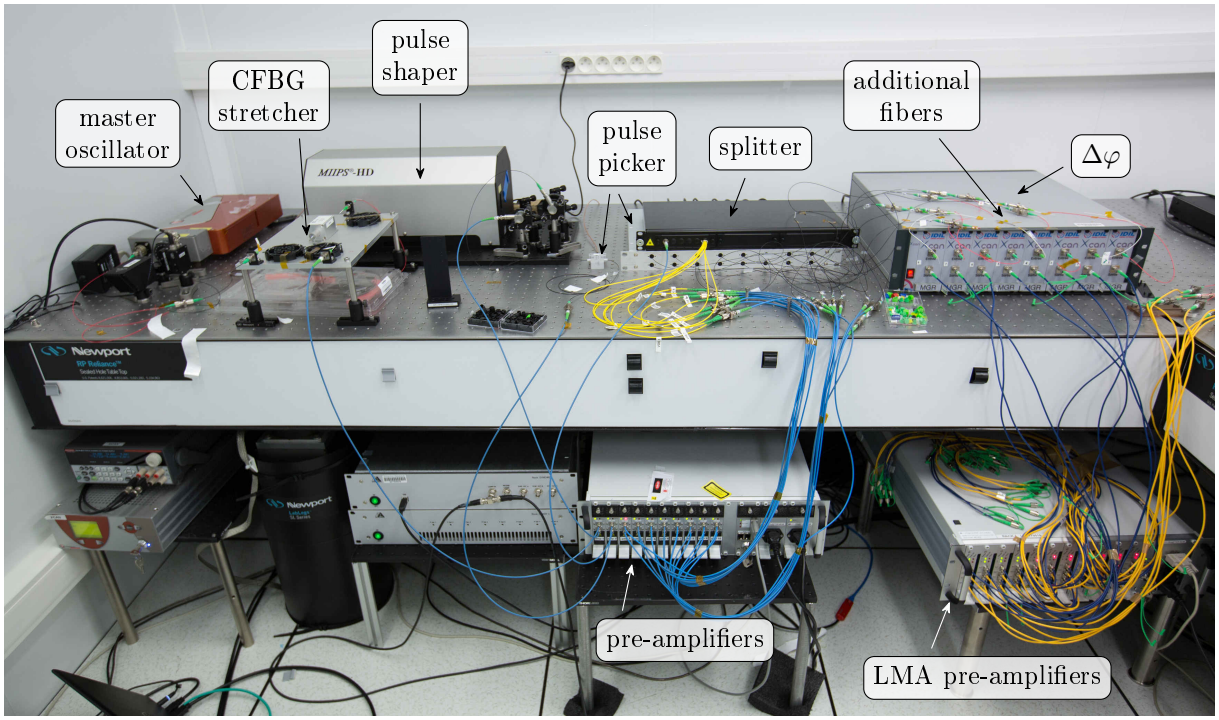

Figure 4.3: Photo of the front end.

power remains at a constant level.

Pulse Shaping

The stretcher is followed by a pulse shaper. Based on a spatial light modulator, this device allows to reshape both the spectral amplitude and phase of ultrashort pulses. This can be done either by applying a pre-defined mask, or by measuring and compensating the actual phase of the pulses using an iterative correction algorithm. In our setup, the pulse shaper is used to compensate for spectral phase mismatches between the stretcher and the compressor. These can arise due to unforeseen changes in the front end setup, such as an increase in overall fiber length, which introduce additional spectral phases and thus degrade the compressibility of the combined beam. Moreover, if the system is operated in nonlinear regime, the accumulated nonlinear phase causes a further downgrading of the compressed pulse quality. To a certain extend, this can be compensated for by the pulse shaper. Besides, due to the limited bandwidth of the pulse shaper of about 18 nm, the spectrum is cut sharp between 1025 nm and 1043 nm.

Phase and Delay Adjustment

The beam is separated into eight sub-beams by a 1x8 spatial splitter, and each sub-beam is passed through a phase and delay control element ($\Delta\varphi$ in the figures) provided by IDIL fibres optiques. These elements consist of two stages: First, a piezomechanical fiber stretcher manufactured by Optiphase is used for the real time phase adjustment. This device consists of 15 m of PM fiber which is wound around a cylindrical piezo stack (cf. fig. 4.4). If a voltage is applied to the piezo,

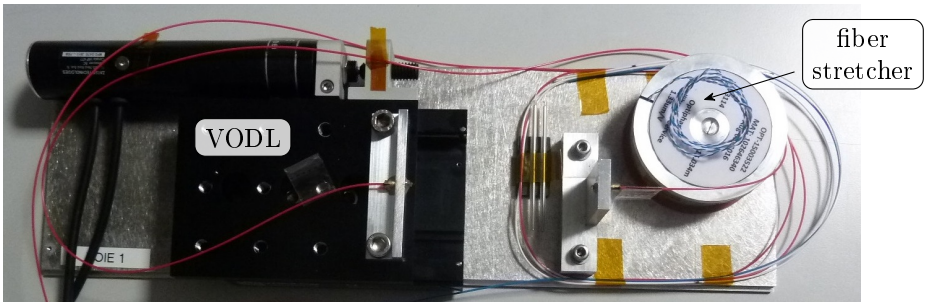

Figure 4.4: Photo of a phase and delay control element.

it changes in diameter, thus slightly stretching the fiber and thereby changing its length. This changes also the spectral phase accumulated by the beam when traveling through the fiber, and the zeroth order component of this phase is adjusted such that all beams remain in phase with the reference beam. Due to the small available driving voltage of $\pm 10\,\mathrm{V}$, the optical path length correction is limited to $\pm 19\,\mu\mathrm{m}$, corresponding to phase differences of $\pm 18.4\,\lambda$. Hence, in order to achieve a stable phase locking, phase fluctuations must not exceed $\pm 18.4\,\lambda$. This means that the laser system has to exhibit a good stability when operated in open loop and needs to be well isolated from any sources of noise. The measures taken on our experimental setup in order to achieve such conditions are discussed in section 4.2.

Second, a free space variable optical delay line (VODL) allows to adjust the optical path lengths of the channels. Figure 4.4 shows a photo of a phase and delay control element, where the VODL can be seen to the left. It consists of a motorized translation stage which can be used to move a fiber port with respect to the fixed position of its counterpart. This translation has a precision of $0.1\,\mu\mathrm{m}$, which corresponds to $0.3\,\mathrm{fs}$. This is by far high enough to avoid efficiency losses due to mismatches in the optical path lengths. Furthermore, the motorization ensures both a precise and repeatable alignment and the possibility to implement an SPGD algorithm for the delay fine adjustment.

However, although all elements of the front end were supposed to feature well matched optical path lengths, differences in fiber length of up to $\pm 9\,\mathrm{cm}$ between two channels have been measured. This is way too large to be compensated for by the VODLs which offer a free-space delay adjustment of $\pm 3\,\mathrm{cm}$ or $\pm 90\,\mathrm{ps}$, corresponding to $\pm 2\,\mathrm{cm}$ of fiber length. Hence, additional pieces of fiber of suitable length had to be added to each channel. Afterwards, the remaining path length differences were matched by adjusting the VODLs.

Pulse Picking

A three-stage pulse picking system manufactured for us by AA Opto-electronic is included in the front end, which allows to reduce the pulse repetition rate. At a given average power, this increases the peak power and energy of the pulses and allows thus to study the behavior of the laser system in presence of nonlinear effects. The pulse picking is performed with acousto-optic modulators (AOM). A first AOM with a short response time of $6\,\mathrm{ns}$ is placed at the very beginning of the front end in order to ensure a good extinction ratio at the initial pulse repetition rate of

55 MHz. A second pulse picker would be needed for a further reduction of the repetition rate in the 61 fiber setup, but was not used in the seven fiber system. The third stage consists of eight parallel pulse pickers with identical optical path lengths, characteristics and driving electronics. In this way it is ensured that all parallel pulse pickers apply the same frequency shifts at the same time to the sub-beams.

The easiest way to obtain the intended repetition rate of 2 MHz would have been to use only the first two pulse pickers. However, it was decided to work with the first and the third stage in order to test the operation of the parallel pulse pickers and to reduce the repetition rate as late as possible. In this way, high peak powers and the corresponding nonlinear effects occur only near the end of the chain, which reduces their impact.

However, the pulse picking system is configured such that the pulse picking ratios of the three stages depend on one another, and need to be at least a factor of three per pulse picker. Hence, even if the second stage is bypassed, it is not possible to achieve pulse repetition rates between 55 MHz and $55\,\text{MHz}/3^3 \approx 2\,\text{MHz}$. In the experiments, the minimum ratio of three has been applied to the first pulse picker, thus reducing the repetition rate to 18 MHz. The ratios applied to the other pulse picking stages were chosen as a function of the desired final repetition rates between the nominal working point at 2 MHz and a much lower value of only 750 kHz. This latter one was used to study the impact of increased peak powers and thereby nonlinear effects on the combining efficiency.

Pre-amplification

Several core pumped Yb-doped single-mode 6/125* fiber amplifiers tailored for us by Keopsys, a Lumibird Group company, allow to raise the average power to $\sim 100\,\text{mW}$. They have been inserted wherever in the 61-channel front end the average power would have dropped below 1 mW, which

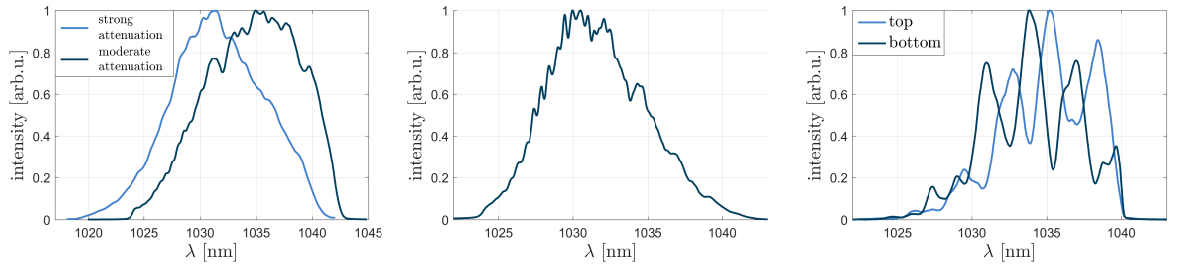

(a) Output spectra of the front end operated at 55 MHz, whith attenuators in front of all preamplifiers (light blue), or in front of all but the LMA preamplifiers (dark blue). The shifted bandwidth is due to a different transmission of the pulse shaper.

(b) Output spectrum of the front end operated at 2 MHz.

(c) Distorted spectra of an uncoiled power amplifier, recorded in the top and bottom of the output beam.

Figure 4.5: Different spectra recorded in the front end.

*Having a core diameter of 6 µm and a cladding diameter of 125 µm

is the typical input power of such amplifiers. The endmost pre-amplifier uses 10/125 LMA fibers in order to minimize nonlinear effects which occur if the pulse repetition rate is strongly reduced. Due to the gain narrowing inherent to these amplifiers, the spectrum of the pulses changes from the flat-top form it obtained due to the hard cut of the pulse shaper to the more triangular shape which can be seen in figs. 4.5a and 4.5b.

In the seven fiber setup, the average power losses are much less important than in the 61 fiber setup, since the pulse repetition rate stays higher and only one 1x8 spatial splitting stage needs to be included. Hence, the pre-amplifiers operate with very high input signals, which implies that their gain is quite small. This in turn results in a shift of the central frequency of the spectrum towards higher wavelengths. In order to reduce this effect and to work with a spectrum which resembles more the one estimated for the 61 fiber setup, attenuators have been included in the front end. Due to the limited number of attenuators available, this was only possible before the spatial splitting, so that the LMA pre-amplifiers stayed largely saturated. The resulting output spectrum has a maximum around 1035 nm, as shown in the dark blue curve in fig. 4.5a. For comparison, the output spectrum of the 61 fiber setup was emulated by putting attenuators in front of all pre-amplifiers of one channel, leading to the spectrum shown in the light blue curve in fig. 4.5a, with a maximum at 1032 nm. The shift of the spectral bandwidth of this spectrum is due to a different alignment of the pulse shaper.

A behavior similar to the one emulated for the 61 fiber setup can be observed for a reduced pulse repetition rate. Since the pulse picking also entails a reduced average power at the pre-amplifier inputs, their gain is increased and the peak of the output spectrum is centered around 1032 nm, as shown in fig. 4.5b.

Preparation for Power Amplification

After the last, large mode area pre-amplifier, one of the sub-beams is separated in order to serve as reference plane wave for the interferometric phase measurement. The remaining seven sub-beams are designated for power amplification. Prior to coupling into the power amplifiers, a small fraction of about 2 % of their overall power is separated by a tap coupler and directed into a security box manufactured by Koheron. The purpose of this element is to rapidly turn off the pump lasers of the power amplifiers in case of a sudden signal breakdown. If Q-switches due to ASE shall be avoided, this turn-off time needs to be well below to the build-up time of the upper state population, which depends on both the upper state lifetime of the Ytterbium ions and the available pump power. For our experimental conditions, this build-up time is estimated at 250 µs. Therefore, the security box is configured such that it opens the hardware interlock of the pump lasers whenever the signal power of one channel stays below a certain threshold during more than 10 µs.

The remaining power of each of the seven sub-beams, typically between 80 mW and 100 mW, is combined with the pump beams and coupled into the power amplifiers. This could have been done in free space. However, as our power amplifiers have a small signal numerical aperture of only 0.03, free space coupling is complex and would require maintenance on a very regular basis.

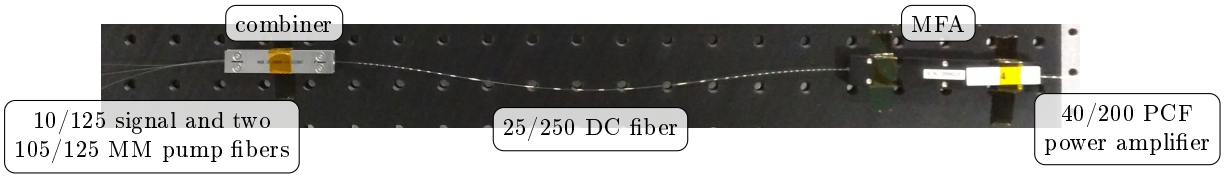

Figure 4.6: Photo of a combiner (silver box) and an MFA (black box) taped to a breadboard. On the left, one signal and two pump input fibers are visible.

Since this would hinder a smooth and simultaneous operation of 61 fiber amplifiers, we decided to work with integrated components. This approach also allows to maintain the advantages of the all-fiber front end. In a first step, the signal fiber is adapted from the initial 10/125 to a 25/250 LMA fiber, which is then combined with the 105/125 multimode (MM) pump fiber into a single 25/250 double-clad (DC) LMA fiber using a pump + signal combiner. Subsequently, the mode area of this fiber is matched to the 40/200 of the power amplifiers using a mode field adapter (MFA). These two components shown on the photo in fig. 4.6 where spliced to the fibers by Optical Engines.

Power Amplification

We use CW pump diodes provided by BWT operating at a wavelength of $\lambda_{\text{pump}} = 976\,\text{nm}$ and providing a power of up to 60 W. In order to avoid variations in the operation conditions of the power amplifiers, the pump wavelength is stabilized to $\Delta\lambda < 1\,\text{nm}$.

The power amplifiers, made of DC-200/40-PZ-Yb LMA photonic crystal fibers from NKT Photonics (see section 1.2.2 for more detail on this fiber), deliver up to 35 W average signal power. Based on simulations regarding the amplified signal power and the amount of nonlinear effects accumulated in the process, their length has been fixed to 1.6 m.

This fiber has been chosen since it is the commercially available PCF amplifier with the largest

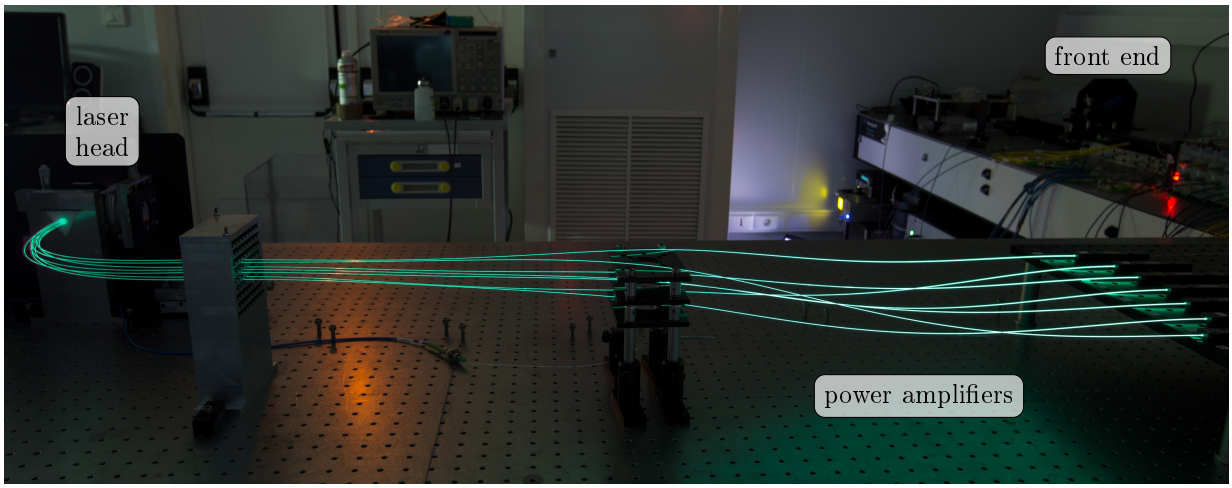

Figure 4.7: Picture of the seven power amplifiers in operation. Note the 90° bending near the laser head. The green color is due to florescence in the visible wavelength range.

MFD, thus providing highest peak powers. However, the specific properties of the fiber, such as the exact position of its core, may vary among different batches and depend on the actual working conditions.

One of the characteristics of this fiber is that it needs to be coiled in order to guarantee a stable monomode operation. As this entails a quite cumbersome fiber arrangement which is inconvenient for our purposes, we first operated the fibers without coiling. However, this lead to spatially modulated spectra, as shown in fig. 4.5c. This could be resolved by introducing a 90° curvature near the fiber end as can be seen in fig. 4.7. Nevertheless, the mode remains spatially sensitive to external perturbations, resulting in pointing instabilities on the individual beams, and therefore also on the combined beam. Since we observed that this effect is largely reduced if the fiber is coiled to at least one full circle, such a configuration is currently being implemented in the 61 fiber setup (cf fig. 5.1 on page 117). On the seven fiber setup, we decided to stay with the mostly uncoiled fibers in order to fully explore the advantages and limitations of this configuration.

4.2 Phase Noise Reduction

As explained in the previous section, the relative phase deviations of each channel must stay within a range of $\pm 18.4\,\lambda$ so that they can be compensated for by the fiber stretchers. If this requirement shall be fulfilled, a good passive noise reduction has to be ensured. In order to determine the main sources of noise in our laser system, numerous phase noise measurements have been performed under varying conditions on all critical elements of the front end. The setup used for these measurements, the main sources of noise which have been identified, and the measures taken to reduce their impact will be presented below.

A schematic of the setup used for the phase noise measurement is shown in fig. 4.8. The outputs of two channels are superposed using a slightly tilted beam splitter, thus creating interference patterns in the two resulting beams. In each path an aperture is positioned such that it selects one interference fringe whose power is recorded on a photodiode. The apertures are aligned such that one photodiode measures the quadrature of the signal of the other diode. The recorded signals are thus given by $I_1(t) \propto \cos\varphi(t)$ and $I_2(t) \propto \cos(\varphi(t) + \pi/2) = -\sin\varphi(t)$, respectively, where $\varphi(t)$ is the phase difference between the two beams. Hence, this phase difference can be determined by $\varphi(t) = \arctan(I_2(t)/I_1(t))$, and the phase noise is derived from the Fourier transform of this time-dependent phase.

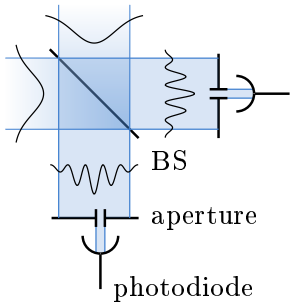

Figure 4.8: Schematic of the phase noise measurement setup.

The measurements presented below were recorded during 100 s, with a sample rate of 10kS/s. Although this allows to record frequency components of up to 5 kHz, the dynamic range of the photodiode reaches its limits already at ~ 1 kHz, resulting in a large noise floor at higher frequencies which overwrites the signal information.

These measurements allowed to identify the frequencies where the phase noise is most prominent. By changing the experimental conditions, these could be traced back to certain elements or components in the setup. Three typical curves of such measurements taken at the LMA pre-amplifier output are shown in fig. 4.9. While fig. 4.9a shows a measurement under normal conditions, in fig. 4.9b the air conditioning system of the laboratory was turned off, which leads to an overall decrease in phase noise, and to a disappearance of the broad peak at 5 Hz. Moreover, the bump at 100 Hz decreases considerably in intensity.

Given these observations, one can conclude that measures have to be taken to reduce the impact of the climate conditioning on the phase noise. The most obvious solution would consist in turning

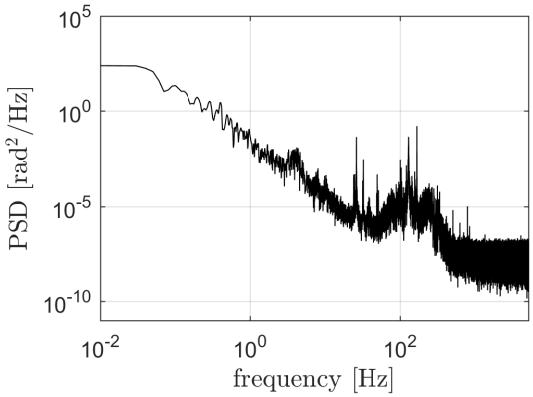

(a) With everything operating normally.

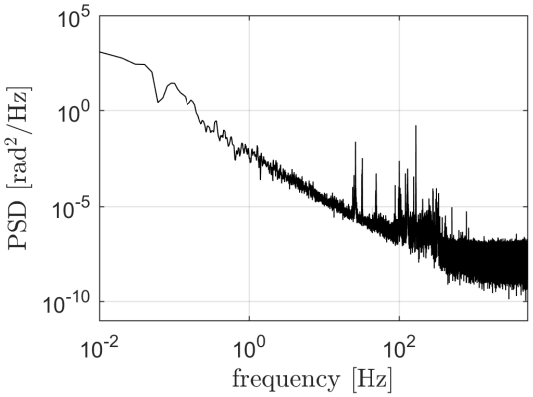

(b) Without air conditioning.

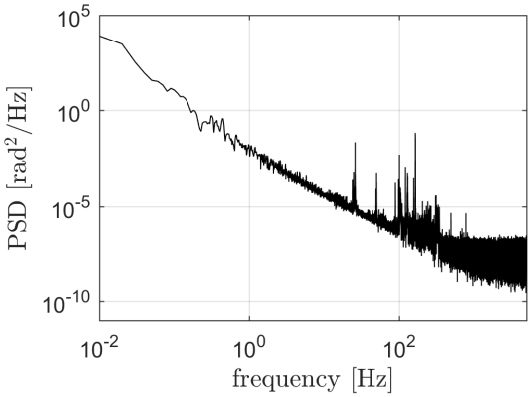

(c) Without air conditioning and pre-amplifier fans.

Figure 4.9: Phase noise spectra of the front end for different measurement conditions.

off the air conditioner during measurements. Under such conditions, a relatively stable operation could be achieved during the short time required to measure the phase noise of the free-running front end. However, coherent beam combining of the power amplifiers was not possible due to the excessive heating of the lab and the resulting ongoing phase changes in the amplifiers. Hence, it was impossible to run measurements with the air conditioning turned off. Therefore, several measures have been taken in order to reduce the impact of the air conditioning on the phase deviations of the amplifiers.

As a first action, enclosures have been installed over the optical tables, which shield the fiber amplifiers from air flows. However, they could not be closed completely since several fibers, cables and hoses had to be passed on the table. Furthermore, as can be seen in the photo of the front end (fig. 4.3), the pre-amplifiers are arranged underneath the optical table, so that they can not be shielded by the enclosure. In order to still provide a minimum of shielding, the pigtails were covered under a plastic tarpaulin. Furthermore, the fibers lying on the optical table were taped on the table in order to reduce their sensitivity to residual air flows.

A similar approach has been considered for the power amplifiers. However, in this case the situation is more complicated since the fibers dangle between 10 cm and 15 cm above the optical

table and their arrangement changes from adjacent at their inputs to hexagonal at the laser head. Hence, a suitable support would have to make up for the height difference and the changing arrangement of the amplifiers. Taping the fibers to a slightly tilted breadboard was tested, but proved to be difficult due to spatial constraints and the relative stiffness and fragility of the power amplifiers. Since on top of that the results were not convincing, this approach was not pursued any further.

A second component which has a considerable impact on the phase noise is the air cooling of the LMA pre-amplifiers. This can be seen by comparing fig. 4.9b and fig. 4.9c, which show phase noise spectra with these fans turned on and off, respectively. In the second case, several peaks, for instance the one at 31 Hz or those around 300 Hz, reduce in intensity or vanish completely. Since turning off the air cooling is not possible due to the heating of the pre-amplifiers, several fan models have been tested in order to find a good compromise between cooling capacity and phase noise increase. The curves shown in fig. 4.9 have been taken with the final fan version.

Similar observations have been made on the VODLs, which initially featured an air cooling system in order to prevent any heating of the motorized delay stages. However, the fans of this cooling system gave rise to considerable amounts of phase noise, whereas no heating could be detected even with the fans turned off. Therefore, and since the supplier confirmed that the fans are not necessarily required, but have rather been installed to be on the safe side, it was decided to simply turn them off for all future measurements.

Finally, also the water cooling of the pump lasers of the power amplifiers has an impact on the phase noise. As the chiller is dimensioned for the 61 fiber setup, its cooling capacity is much stronger than what is needed for operating the pump diodes of only seven power amplifiers. Hence, instead of constantly adjusting the temperature of the cooling water, the chiller waits until the temperature exceeds a certain critical value before reducing it. In consequence, the water temperature constantly fluctuates around a certain set point value. This in turn has an impact on the wavelength of the pump diodes, which depends on the water temperature and therefore fluctuates slightly within the stabilization range of $\Delta\lambda < 1\,\mathrm{nm}$. These fluctuations also affect the gain of the power amplifiers, which depends on the pump wavelength. Since the gain is related to the refractive index of the silica fiber via the Kramers-Kronig relations, a change in gain translates directly into a refractive index change. Hence, also the phase of the light traveling through the fiber changes, resulting in a phase shift of the power amplifiers which depends on the cooling characteristics of their pump lasers.

Since this behavior occurs on relatively long time scales of several seconds, it was observed as oscillations in the correction voltage of the fiber stretchers. In order to overcome these fluctuations, a set point water temperature was determined experimentally at which the wavelength of the pump diodes remains mostly stable, and the water flow of the chiller was largely reduced so that it needs to be cooled constantly.

All the measures described above contribute to the passive reduction of phase noise. However, occasionally the remaining phase differences still exceeded the $\pm 18.4\,\lambda$ allowed by the fiber stretchers, resulting in uncompensated relative delays between the channels. This is mainly due to the uncoiled and dangling power amplifiers, whose movements give rise to small local bendings

of the fibers. This leads not only to a direct change of the local refractive indices, but also to power losses due to local changes in the waveguiding properties, which impact the gain in the amplifier and therefore also the refractive index. These local refractive index variations translate directly into phase fluctuations.

This behavior will be remedied in the 61 fiber setup by taping the fibers to breadboards. Furthermore, in this upscaled setup the phase fluctuations caused by the pump diodes will be reduced, since the cooling system will be operating at its optimal working point, thus ensuring a better temperature stability. As these measures could not yet be taken in the seven fiber setup, the exceeding group delay was corrected manually by readjusting the VODLs whenever necessary.

4.3 Laser Head

The laser head is the structure where the individual fiber amplifiers are assembled in a hexagonal array. It has thus to meet the precisions stated in section 3.3, while also allowing for a safe and uncomplicated operation and maintenance.

In this section, the setup of our laser head and the associated fiber array alignment process will be introduced. Subsequently, an estimation of the imprecisions within the final fiber array will be presented.

4.3.1 Fiber Array Setup

We use a simple fiber stacking approach to assemble our hexagonal array. The principle is illustrated in fig. 4.10a. The basic part is a high precision 60° V-shape holder, in which high precision ceramic sleeves (green in the drawing) of an outer diameter of 3.2 mm are stacked so that they form a hexagonal array. They are hold in place by a top lid which is tightly screwed to the main part. A small foam layer (dark red) is integrated into the lid, which softens and equally spreads the mechanical pressure exerted on the sleeves. In order to insert the power amplifiers in this structure, a ferrule of suitable size is put near the end of the fibers, so that they can be easily slid into the sleeves. Finally, a second plate is slid onto the main part in order to define the ferrule longitudinal position. This plate has boreholes whose diameters are slightly larger than the endcaps of the power amplifiers. Thus, a part of the residual pump power which diverges largely in the endcaps exits through their lateral surfaces and is ultimately absorbed by this plate.

Nevertheless, there is still a non-negligible amount of pump light which propagates towards the microlens array. Due to its large divergence, the pump of one fiber impinges on several neighboring

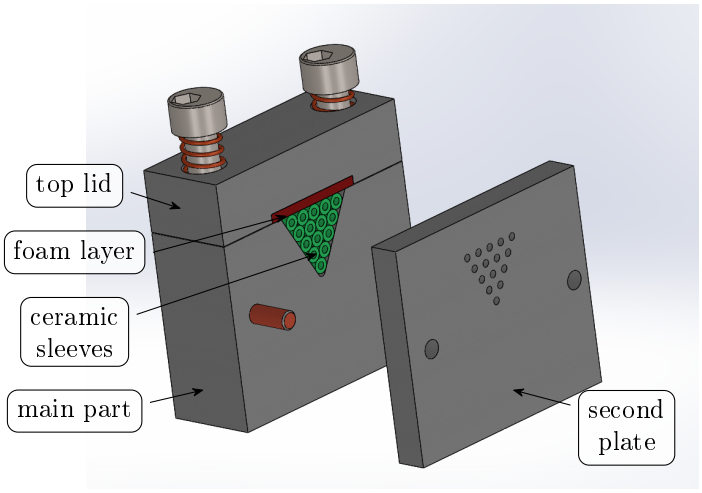

(a) Mechanical drawing of a small size test version of our laser head, illustrating the working principle. The fiber amplifiers are not shown.

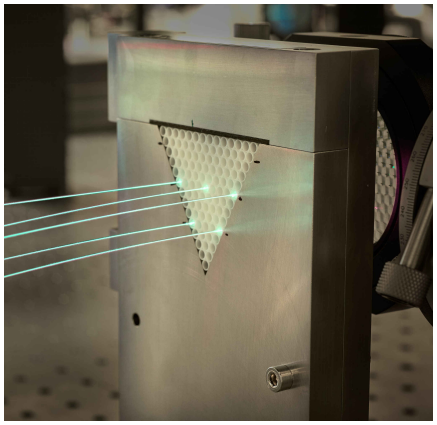

(b) Photo of the laser head with five fibers inserted. The large spacing between the fibers was chosen for preliminary tests.

Figure 4.10: Laser head.

microlenses. Hence, its light disperses into all directions, giving rise to a very large pattern of partly collimated unabsorbed pump beams just centimeters after the microlens array. In order to block this stray light, a metal blocking plate with a hole of the size of the composite seven beam array has been inserted in the beam path. However, some of the parasitic beams arisen in the first ring of the hexagon still pass through this plate, so that a second aperture has been included in order to block whatever stray light remains.

Figure 4.11a shows a photo of the laser head, the microlens array and the blocking plate. A false-color image of the same assembly taken with an infrared camera while operating the laser system at full power is shown in fig. 4.11b. While the microlens array and the blocking plate remain at a reasonable temperature, the ceramic sleeve array heats considerably. This is due to a heating of both the fibers themselves and the second plate which absorbs an important part of the residual pump power and whose heat radiates into the sleeve array. Furthermore, it has been noticed that the resulting temperature increase leads to a small change of the beam pointing, observable as a displacement of the far field. Since the heating of the fibers could not be remediated without changing the whole setup, it has been decided to implement a water cooling on the second plate. This allowed to reduce the temperature in the laser head from almost 80 °C to less than 50 °C, as can be seen in fig. 4.11c. However, the circulation of the water in the second plate gave rise to vibrations which for their part affected the pointing stability of the far field. Hence, the second plate was slightly pulled away from the main part. In this way, the mechanical motions of the two plates are decoupled and the beam pointing remains stable even at high power operation with active water cooling.

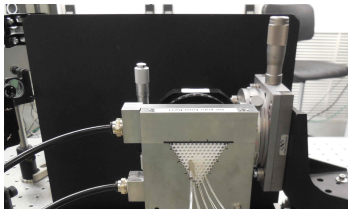

(a) Photo of the laser head assembly.

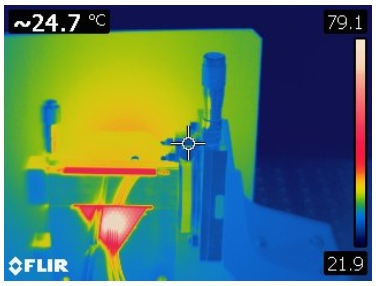

(b) Temperature without water cooling ($T_{\max} = 79.1\,°C$).

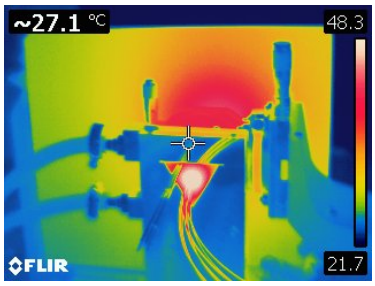

(c) Temperature with water cooling ($T_{\max} = 48.3\,°C$).

Figure 4.11: (a) Photo and (b), (c) false-color images of the laser head, the microlens array and the blocking plate, taken with an infrared camera. Note the different color scales.

However, as the second plate also serves as reference plane for the longitudinal alignment of the fiber array, it has to be joined to the first one for the insertion of the fibers. The separation of the two plates has to take place once the fiber array is properly aligned, so that the ferrules do not outreach the main part and are well decoupled from the water cooled shifted second plate.

Besides, the fiber ending including the ferrule and the endcap was carefully designed in order to guarantee a repeatable, break-safe fiber insertion into the ceramic sleeves and a safe removal in case of maintenance or damage. When adding the ferrule around the fiber, special care was taken that the fiber output mode was well centered with respect to the ferrule outer diameter. A

schematic of the final design and its insertion in the laser head is shown in fig. 4.12a, and a photo of a fiber ending in fig. 4.12b. The design has been developed in close collaboration with Optical Engines, who also took over its manufacturing.

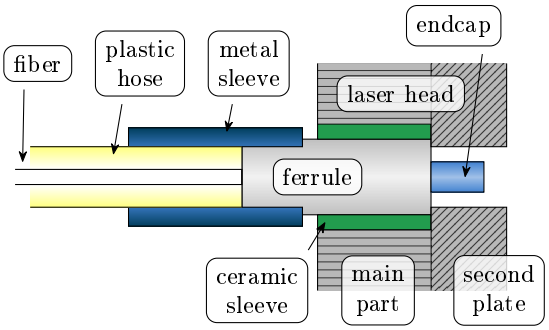

(a) Schematic of a fiber inserted in the laser head (not to scale).

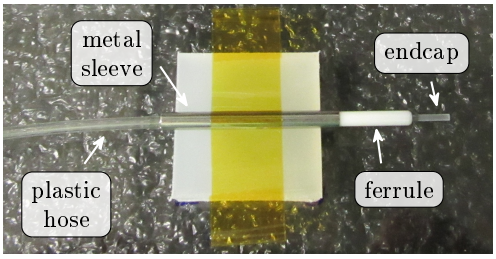

(b) Photo of a fiber ending, taped on a white plastic block.

Figure 4.12: Final fiber ending design.

A former version of the fiber ending did feature neither the metallic sleeve nor the plastic hose shown in fig. 4.12. However, it turned out that inserting the fibers by hand in a closely packed array with a pitch of only 3.2 mm was precarious, especially since the available space is very limited. Moreover, it was almost inevitable to touch the ferrules themselves during the insertion process, which might pollute them and thus reduce the precision of the alignment. Therefore, metal sleeves have been added around the ferrules. Touching these rather than the ferrule itself guarantees a safe and proper insertion. Moreover, as soon as two adjacent fibers have been inserted successfully, a third one can simply be put onto the metallic sleeves of the other two and is then slid into its respective ceramic sleeve. Although slight corrections of the fiber position and angle might be necessary, this mechanism largely facilitates the insertion process.

Furthermore, a plastic hose of a length of 10 cm surrounds the fiber at its ending in order to stabilize the fiber and make it less sensitive to mechanical vibrations. Moreover, it also provides a means to manipulate the amplifiers without touching the fibers themselves. This is necessary since there is only very little spacing between the metallic sleeves in the hexagonal array, so that grabbing an individual sleeve for removing or realigning the fiber would be almost impossible.

It should be noted, however, that this design is the result of an iterative process, which was completed in parallel with operation of the seven fiber setup. Therefore, the fibers used in this setup do not yet feature the metallic sleeves and the plastic hoses.

4.3.2 Fiber Array Assembly and Characterization

The assembly of the hexagonal fiber array starts with the stacking of the ceramic sleeves in the main part of the laser head. The fibers are then inserted simply by sliding their endings into these sleeves, so that only very minor adjustments can be performed on their positioning, and the precision of the fiber tilts and displacements is largely determined by the precision of the sleeve array. As these sleeves are rigid high precision components, imprecisions in their alignment arise

most probably due to dust which gets between the sleeves during their assembly. Another source of imprecisions might be dust which gets into the sleeves once the array is assembled, and which hinders the correct insertion of the fibers into the sleeves.

The polarization axis of the fiber amplifiers aligns automatically parallel to the coiling plane. Therefore, all the beams should be polarized horizontally. However, as the polarizing characteristic of the fibers is not perfect, there is a vertical component in each individual polarization direction. Due to the birefringence of the fiber, this component has a different group delay than the horizontal one, so that the two cannot combine coherently and the vertical component needs to be removed. Moreover, the polarization self-alignment procedure is not perfect, so that small individual deviations of the horizontal polarization may occur. These have to be filtered as well. For this purpose, the composite beam is sent through a half-wave plate and on a thin film polarizer (TFP, cf. fig. 4.17). The half wave plate is used to turn the polarization of the composite beam by 90° so that it is then vertical and reflected by the TFP. Moreover, as the exact polarization directions vary slightly among the individual beams, the wave plate allows to adjust the average polarization such that the sum of the power losses of each channel is minimized. Using this alignment procedure it was also possible to check that the differences in individual beam polarization are below the 7° stated in section 3.3.1, so that efficiency losses due to polarization mismatches are avoided.

As described in section 2.2.1, the output beams of the fiber amplifiers are collimated by a microlens array. In order to meet the precisions on the alignment of this array stated in section 3.3.2, it was inserted in a mount featuring precision mechanics on all six spatial degrees of freedom.

The alignment of the microlens array was performed both in the near field and the far field. In a first step, the lateral position of the microlens array was adjusted such that the beams were well centered within their respective microlenses. This was observed on a camera, and let to a near field as shown in fig. 4.13b. In a second step, the spot size of the incoherent far field was minimized by adjusting first the rotation of the microlens array, and second its focal distance.

This alignment procedure gave a first insight into the properties of the microlens array, the

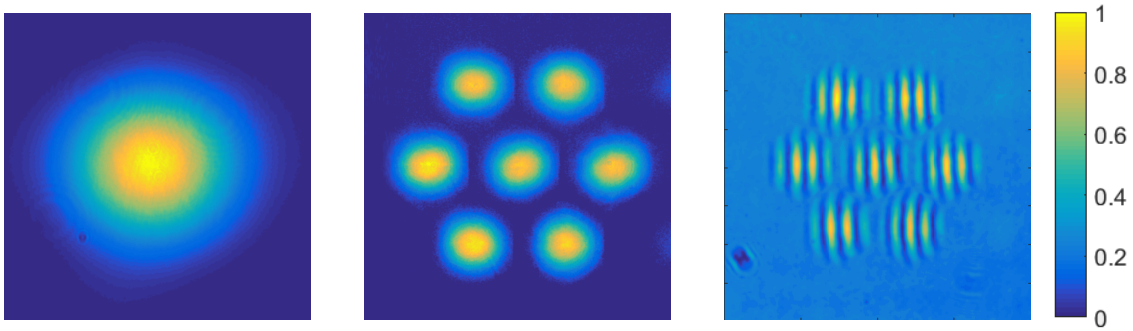

(a) Incoherent far field. (b) Near field. (c) Near field with interference fringes.

Figure 4.13: Fields used for the alignment of the fiber array and the characterization of the laser head.

relative precision between itself and the fiber array, and misalignments in the fiber array itself.

In the far field, the minimum spot size of each individual beam was not always obtained for the same longitudinal microlens position. Hence, the focal distances of some beams were not well matched, and a manual re-adjustment was performed. In order to do so, the microlens array position was fixed and the positions of the fibers in question were carefully corrected with respect to their focal spot sizes. The standard deviation of the remaining errors is as low as $\Delta f = 0.04\,\mathrm{mm}$, and has therefore a negligible impact on the combining efficiency.

Furthermore, it was observed that the far fields of some beams got somewhat distorted while scanning the longitudinal position of the microlens array (cf. fig. 4.14). This is an indication of an astigmatism which could arise due to either errors on the lateral fiber positioning, or production imprecisions on the microlens array. In the first case, correcting this aberration is difficult due to the very limited possibilities for realignments in the fiber array, whereas in the second case only a replacement of the microlens array could solve the problem. In consequence, these beam distortions needed to be tolerated in the seven fiber setup.

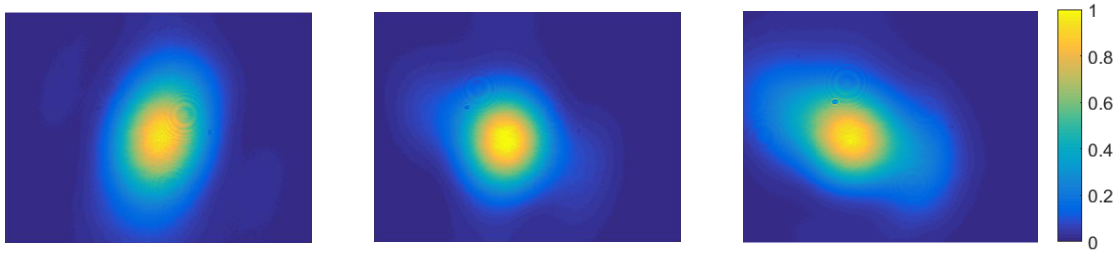

(a) Distance shorter than the microlens focal distance.

(b) Distance approximately the microlens focal distance.

(c) Distance larger than the microlens focal distance.

Figure 4.14: Example of the shape of a single beam at the position of the far field, while changing the distance between the microlens array and the laser head.

Finally, it was not possible to achieve a perfect overlap of the beams in the far field. This can be attributed to a slight pitch mismatch between the fiber and the microlens array. However, quantifying this mismatch proved to be difficult due to the very high precision required in the measurements.

The analysis of the near field image allowed first of all the measurement of the microlens fill factor. For this purpose, the relative diameter of the beams in the near field was evaluated, yielding a fill factor of $\tau_r = 0.7$. This result is significantly smaller than the ideal value of 0.93, which means that the microlens focal length has been chosen too small. This focal length was determined based on the theoretical M^2 and mode field diameter of the output beam of the power amplifiers. However, the divergence of the real beam is inferior to the upper limit stated in the datasheet, which entails a significant increase of the optimum microlens focal length. Hence, in the experimental setup using the smaller focal length, the beams have not yet reached their optimum size when they hit the microlens array. This reduced beam width results in an enhancement of the side lobes of the far field as shown in fig. 4.15b and a reduction of the maximum possible combining efficiency to $\eta(\tau_r = 0.7) = 0.61$.

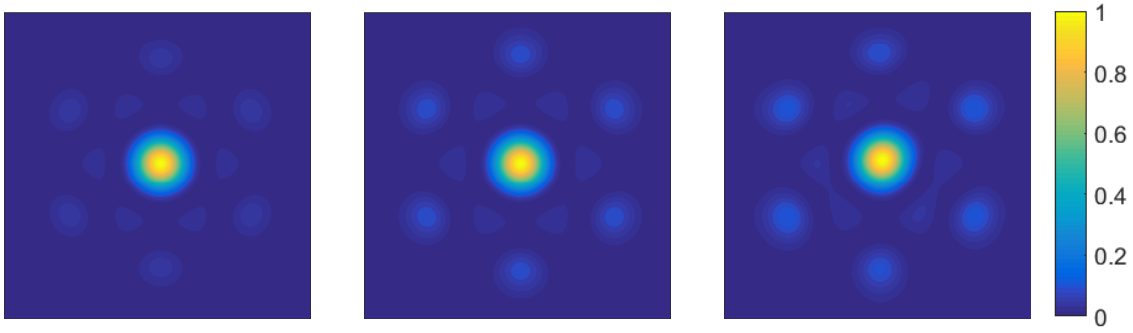

(a) Ideal far field.

(b) Far field for a microlens fill factor of $\tau_r = 0.7$.

(c) Far field including measured alignment errors.

Figure 4.15: Simulated far fields.

Besides, the low microlens fill factor leads to an increased microlens transmission of $t_{\mu\text{-lens}} = 0.98$. In consequence, microlens clipping due to a displacement of the beams on their respective microlenses is reduced. Such displacements correspond to misalignments in the fiber tilts, which can therefore tolerate larger errors than those calculated in section 3.3.1.

Measuring these fiber tilt errors in the near field image based on the displacement of the beams with respect to their microlenses has been attempted, but proved to be difficult due to the high precision which is required by this approach. Therefore, the uncertainties on the measurements were as large as the measured values themselves. Hence, this method gives only the order of magnitude of the tilt errors, which is about $\Delta\theta = 0.7\,\text{mrad}$. Given the low microlens fill factor stated above, this corresponds to efficiency losses of 0.5 %.

Furthermore, also the positioning errors in the fiber array have been estimated using the near field. For this purpose, the interference fringes between the beams and the reference plane wave were considered (cf. fig. 4.13c). Since a positioning error between a fiber and its microlens leads to a tilted wavefront, the corresponding fringe pattern has either a fringe period varying from the average one or is tilted as well. Errors in the individual fiber positioning can thus be inferred from deviations between the individual and the overall period or tilt angle of the interference fringes. Unfortunately, this method is not more precise than the one used for the fiber tilt estimation. The measured errors on the fiber positioning are on the order of $\Delta x = 2.6\,\mu\text{m}$ and lead to efficiency losses of 4 %.

Finally, it was attempted to measure the gap between the microlenses based on a near field image of the lenses. However, this is difficult since the imaging itself highly depends on the exact position of the camera on the optical axis, so that quite different gaps can be obtained for slightly varying camera positions. The best recorded picture is shown in fig. 4.16a, but has to be mistrusted since there are diffraction patterns clearly visible at the edges of the lenses. Hence, the imaging is probably not perfect, leading to a falsified estimate of the microlens gap. Also the measured value of $\sim 330\,\mu\text{m}$ supports this hypothesis, since it largely exceeds the upper limit of $200\,\mu\text{m}$ indicated by the manufacturer.

Given that this measurement was not satisfactory, a high precision photo of one microlens was

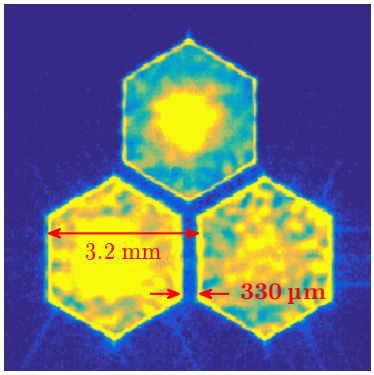

(a) Near field image of three lenses.

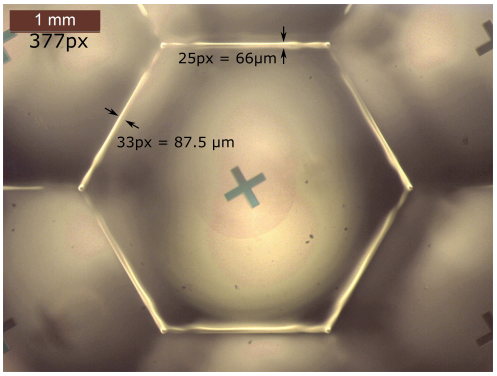

(b) High precision photo of one lens. The cross is a leftover of a mask applied during the manufacturing process.

Figure 4.16: Estimations of the gap between the microlenses.

taken (see fig. 4.16b) in order to directly measure the width of the contact zone between the lenses. However, this approach was not very precise either, as the results vary between 66 µm and 88 µm. Moreover, one can not be sure that the gap is really restricted to the bright lines visible on the photo, since it is highly possible that also the surrounding areas do not properly transmit the light.

Since neither of the two measurements presented above is in accordance with the manufacturer's specifications of 100 µm $\leq g \leq$ 200 µm, an intermediate value of 150 µm has been assumed for the microlens gap. This would lead to a decrease of combining efficiency of 3 %.

An overview of the efficiency losses due to the different misalignments is given in table 4.1. It can be seen that the most important losses are due to the reduced microlens fill factor, and a new microlens array with a longer focal length has been purchased in order to reduce these losses in the 61 fiber setup. Furthermore, also the gap between the microlenses has a noticeable impact on the combining efficiency. Since this gap is an artifact of the manufacturing process of the array, there is no immediate way to reduce its size and therefore the related efficiency losses.

Among the errors on the fiber array, only the displacement exceeds the one percentage point efficiency loss threshold fixed in chapter 3. Given that we inserted and removed all of the fibers

criterion	estimated errors	efficiency losses
microlens fill factor τ_r	0.7	6 %
microlens gap	150 µm	3 %
polarization	$< 7°$	negligible
defocus Δf	0.04 mm	negligible
fiber tilt $\Delta\theta$	0.7 mrad	0.5 %
fiber pitch Δx	2.6 µm	4 %

Table 4.1: Overview of the estimated errors of our laser head and the resulting losses in combining efficiency.

several times, this may be due to dust which got into the ceramic sleeves. A thorough cleaning and subsequent reassembly of the sleeve array might therefore be helpful to decrease the alignment errors, but was not performed during characterization of the seven fiber laser system since the current performance of the laser head was considered satisfactory.

The reduced microlens fill factor and the alignment errors on the fiber array were inserted into the simulations presented in chapter 3 in order to obtain an estimate of the far field which has to be expected in the experiments. The result is shown in fig. 4.15c and exhibits a combining efficiency of $\eta_{\mathrm{err}} = 0.56$. The microlens gap has not been included in these simulations because of the high uncertainty of the estimated values. For the gap of $g = 150\,\mu\mathrm{m}$ listed in table 4.1, the far field efficiency would reduce by 2.5 % due to an increase of the side lobes, whereas the decrease in microlens transmission corresponds to 0.5 % and is therefore negligible.

4.4 Laser Back End

The laser back end starts right after the assembly of laser head and microlens array and includes all optical components which are necessary for the coherent beam combining itself, the spatial filtering of the far field, and the temporal compression of the combined beam. A schematic of this back end is shown in fig. 4.17. It should be noted that the scheme is not to scale, where in particular the focal distances of the lenses are arbitrary. Moreover, several apertures and imaging lenses have been omitted in order to keep the schematic as simple as possible.

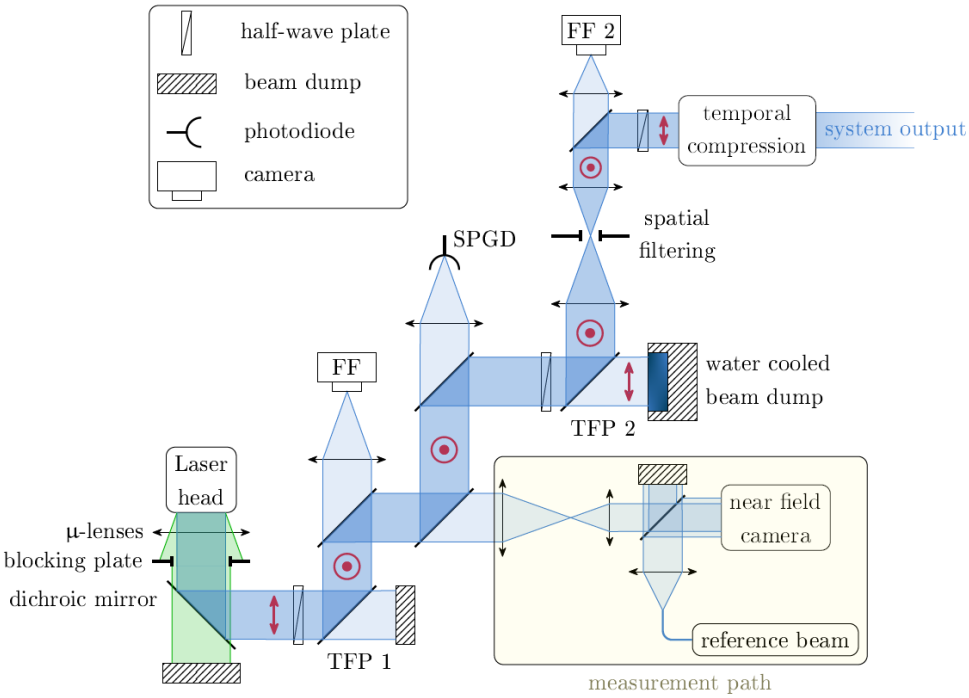

Figure 4.17: Schematic of the laser back end (not to scale). The red symbols indicate the polarization of the beam. The far field is located at the spatial filtering aperture, and the combined beam is found by truncating it at its first extinction.

The back end starts behind the assembly of laser head, microlens array and blocking plate which was described in the previous section. Since the emitted composite beam still consists of both pump (green in fig. 4.17) and signal (blue) light, the former one is removed with a dichroic mirror and blocked by a beam dump.

In a next step, it is assured that all subbeams exhibit one and the same polarization and orthogonal components are filtered by a half-wave plate and a first TFP, as described in section 4.3.2. However, the filtering of a single TFP is not strong enough to remove all the orthogonally polarized parts, so that a second TFP has been added later on in the back end.

Subsequently, three mirrors are used to separate small fractions of the beam, which are then used for various steps in the coherent beam combining process. Although the resulting beams are very faint, attenuators (not shown in fig. 4.17) had to be used in all three cases in order to avoid saturating the measurement devices. These attenuators consist of two sets of a half-wave

plate and a polarizing beam splitter (PBS). The first set is needed to remove remaining horizontal polarization components, so that the second set can be used to attenuate the beam without having to worry about the admixing of orthogonally polarized light.

Behind the first mirror, the far field of the composite beam is observed on a camera in the focal plane of a lens. This serves as a visual tool in the alignment process and gives a first idea of the quality of the coherent combining.

The second mirror is used to create the measurement path needed for the phase measurement of the phase correction algorithm. The composite near field is imaged on a 1 kHz fast camera and a 50/50 beam splitter is used to superpose it with a reference plane wave in order to create the interference fringes necessary for the phase measurement. Since the reference beam is not power amplified, a passive fiber of suitable length has been added into its path in order to compensate for the missing length of active fiber. At its output, the reference beam is collimated by a lens of a focal length of a few tens of centimeters and a diameter of two inches. Hence, the size of the resulting beam is much larger than the one of the camera screen, so that its intensity is fairly constant within the useful zone of the camera. Furthermore, as this camera is placed near the image focal plane of the lens, the wavefront of the collimated beam is approximately plane. The reference beam can thus be considered as a plane wave.

Behind the third mirror, another lens is used to create another far field, whose side lobes are removed with a pinhole (not shown in fig. 4.17). The power of the remaining central lobe is detected by a photodiode and fed to an SPGD algorithm which optimizes the static phase offsets of the individual beams (cf. section 2.2.2). In this way, the combining efficiency measured in the phase locked system is maximized.

Afterwards, the beam is passed through another set of a half-wave plate and a TFP. This allows not only to further filter the orthogonal polarization, but also provides a means of regulating the power in the subsequent part of the laser back end. For alignment purposes, it is often desirable to work with a beam of low average power. However, during the transition from low to high pump powers the relative phases and delays between the channels change due to the heating of the fiber amplifiers. Hence, they have to be adjusted in the high power regime once the whole setup is well thermalized. It is thus necessary to work with high output powers, but the polarization of the beam can be rotated such that most of the power traverses the TFP and is absorbed by a large, water cooled beam dump. The alignment of the subsequent components can thus be realized using only a part of the overall power, and the whole power is transmitted only in the final measurements.

This stage could have been included at an earlier point in the back end, so that the additional polarization filtering in the beam diagnostic paths described above could have been omitted. However, in this case a power adjustment in the main beam path would have implied a change of power in these secondary paths. Hence, a frequent readjustment of the power incident on the beam diagnostics would have been necessary. In order to avoid such complications and to keep the power in the secondary paths constant, it was preferred to place the large beam dump after these paths.

The next step in the laser back end is the spatial filtering of the far field, which is obtained

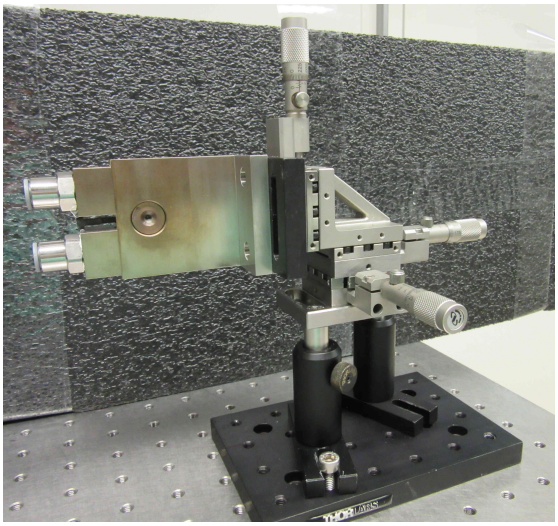

(a) Mount of the spatial filtering pinhole. The metallic adapters to the left can be used to connect the hoses for water cooling. The brownish color is due to excessive heating of an uncooled mount.

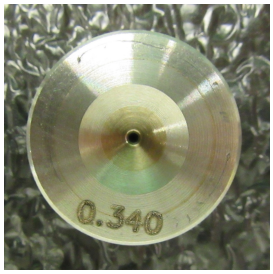

(b) Unused pinhole with aperture diameter marked on the piece.

(c) Filtering pinhole after use in the experiments. The impact of the six side lobes of the far field are visible on the discolored area near the hole itself.

Figure 4.18: Components used for the spatial filtering of the far field.

by passing the composite beam through a thin lens and a truncating aperture. This aperture is inserted in a water-cooled precision mount as shown in fig. 4.18a. In this way, its position can be exactly matched to the main lobe of the far field, and the water cooling avoids excessive heating of the mount.

Using a selection of lenses and pinholes with different diameters, the relative size of the filtering aperture in the far field can be adjusted arbitrarily. It is thus possible to obtain different truncated beam shapes, as was shown in the simulations in section 3.1 and will be demonstrated experimentally in section 4.5.4. However, in order to obtain the combined beam as defined in section 2.1.1 and to measure the combining efficiency, the far field has to be truncated at the first minimum next to the main lobe.

Besides, as the filtering pinholes are designed as the top of a cone carved in a small metal block, their edges are quite thin and therefore easily changed in shape by optical micro-machining. This is illustrated in fig. 4.18b and fig. 4.18c where an unused pinhole is compared to one which served as filtering aperture in measurements conducted at high power without water cooling. The impact of the side lobes of the far field is visible in the discolored area near the hole itself. In order to avoid such or similar damages of the pinhole, it is preferable to choose the position of the aperture such that there is not too much power incident on the edges of the pinhole. This implies that the aperture should be placed at a power minimum of the far field, for instance at the first extinction next to the main lobe (as shown in fig. 4.24a), or just before the secondary lobes (fig. 4.27a (top)).

Behind the spatial filtering, the transmission of another mirror is used to image the filtered far field on another camera. By adding a further lens, also the recovered near field can be imaged. This setup was also used to measure the beam quality factor M^2 of the combined beam.

The last element in the laser back end is the temporal compression stage, which relies on a

1760 l/mm multilayer dielectric reflection grating pair (see photo in fig. 4.19). A half-wave plate has to be added in front of the compressor in order to rotate the beam polarization back to horizontal, so that the light gets properly reflected by the gratings. The output of the compressor represents in the same time the output of the whole laser system.

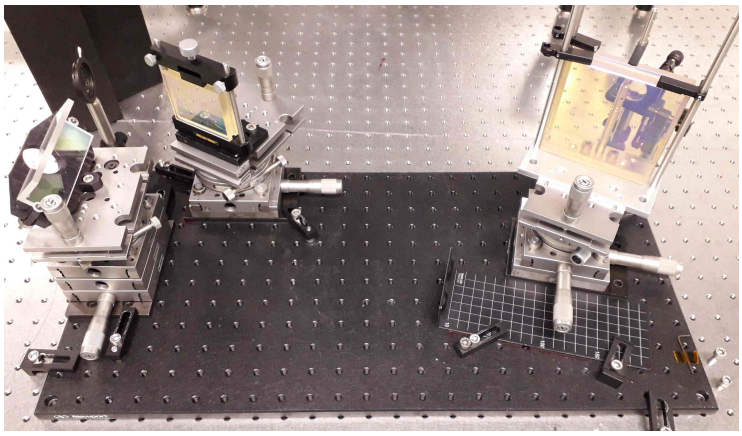

Figure 4.19: Photo of the compressor used in our laser system.

4.5 Experimental Results in Linear Regime

In this section, five different measurements which were taken in order to fully characterize the performance of the laser system operated at full power in linear regime at 55 MHz will be presented.

In this context, full power means that the output power of the power amplifiers is limited by the available pump power. Due to varying coupling and conversion efficiencies among the power amplifiers and slightly different polarization directions, similar signal output powers may be reached for quite different pump powers. Since one of the fibers was limited to an average power of 25.4 W at the position of the spatial filtering pinhole, the other amplifiers were adjusted accordingly, yielding an overall power of $P_{\mathrm{FF}} = 178\,\mathrm{W}$ in the far field.

4.5.1 Residual Phase Noise

The residual phase noise was measured between different sets of adjacent fibers. The coherent superposition of only two beams obtained at the focal plane of a lens leads to interference fringes in the far field, which allowed to measure the residual phase using a setup similar to the one described in the previous section and schematically shown in fig. 4.20a. A beam splitter separates the far field into two paths, so that the signal and its quadrature can be recorded on two independent photodiodes.

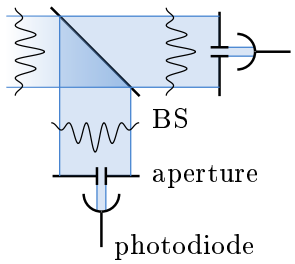

(a) Schematic of the phase noise measurement setup.

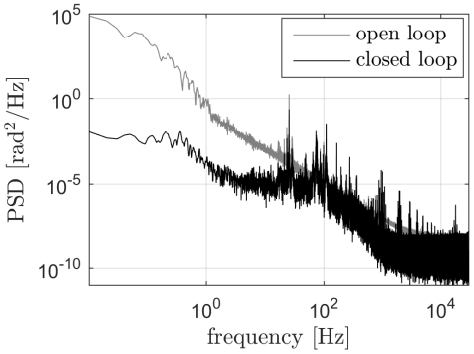

(b) Example phase noise power spectrum, taken between the two topmost fibers of the hexagonal array.

Figure 4.20: Phase noise measurement.

These measurements allow to access the relative phase between two fibers, $\varphi(t) = \varphi_1(t) - \varphi_2(t)$, where $\varphi_{1,2}(t)$ are the phases of the two individual fibers. From these results, the corresponding phase noise density has been be calculated. Additionally, the measurements in closed loop are characterized by the residual phase error between the two fibers, $\varphi_{\mathrm{res}} = \sigma[\varphi(t)]$, where σ denotes the standard deviation.

However, as the maximum tolerable phase deviation of $\lambda/38\,\mathrm{RMS}$ obtained in the simulations (cf. section 3.4.2.2) corresponds to the phase error of a single fiber, this parameter is much more relevant. Since all fibers are phase locked to a common reference beam, they all share the same rapidly changing phase offset. Given that a phase common to all beams has no impact

on the combining efficiency, it will be neglected in the following discussion. Besides, the phase of each single fiber deviates slightly from this global phase. This can be described by small individual phase changes $\varphi_i(t)$ and the corresponding residual phase error of an individual fiber of $\varphi_{\mathrm{res},i} = \sigma[\varphi_i(t)]$.

Since the residual phases of the individual fibers are not correlated with each other, the residual phase error between two fibers can be written as $\varphi_{\mathrm{res}} = \sqrt{\varphi_{\mathrm{res},1}^2 + \varphi_{\mathrm{res},2}^2}$. Assuming that both fibers are subject to the same noise and exhibit therefore the same individual residual phase error $\varphi_{\mathrm{res},1} = \varphi_{\mathrm{res},2} = \varphi_{\mathrm{res},i}$, the relative error between two fibers simplifies to $\varphi_{\mathrm{res}} = \sqrt{2}\varphi_{\mathrm{res},i}$. It is thus possible to calculate the residual phase error of a single fiber based on the value measured between two fibers.

Figure 4.20b shows a typical result of a phase noise measurement, in this case taken between the two topmost fibers of the hexagonal array. The open loop phase noise characterizes the impact of the noise present in the lab on the free-running fiber amplifiers. In closed loop, the active phase locking reduces the phase noise in the low frequency regime by up to five orders of magnitude.

Although the other curves resemble the one displayed above, the residual RMS phase deviation can vary for different fiber pairs. For instance, the measurement shown in fig. 4.20b yields a residual phase error of $\varphi_{\mathrm{res}} = \lambda/34\,\mathrm{RMS}$ between the two fibers, which corresponds to an error of $\varphi_i = \lambda/48\,\mathrm{RMS}$ on each fiber. Considering that in the seven fiber setup the phase of each channel needs to be stabilized to $\lambda/38\,\mathrm{RMS}$ in order to avoid losses in combining efficiency, this is a very satisfying result. However, under comparable experimental conditions, the two bottommost fibers of the hexagon exhibited a residual phase error of only $\varphi_{\mathrm{res}} = \lambda/55\,\mathrm{RMS}$. The reason for this unequal behavior can be found in the different positions and mountings of the fibers: the upper fibers are more exposed to the air flows of the lab's air conditioning system, whereas a part of one of the bottom fibers was taped to a breadboard, which stabilizes its position and phase by somehow reducing the impact of air flows.

Nevertheless, the results measured on the different fiber pairs remain comparable in a sense that they have no impact on the combining efficiency.

All in all, the demonstrated phase stabilization is more than adequate for the seven fiber setup. In contrast, for the upscaled version of 61 fibers, a residual phase error of $\lambda/48\,\mathrm{RMS}$ on a single fiber is required in order to avoid efficiency losses due to phase mismatches. Since this is exactly the value measured for the two topmost fibers in the seven fiber setup, the phase stabilization is sufficient even for the more severe requirements of the larger setup. Nevertheless, as the exact value of the residual phase noise highly depends on the day-to-day experimental conditions, a further reduction of the phase noise would be beneficial in order to ensure a stable operation even under varying and possibly less favorable conditions. Such a reduction will be achieved in the 61 fiber setup by fully closing the enclosure around the optical table, and by coiling each power amplifier to a full circle and taping it to a breadboard.

4.5.2 Combining Efficiency

Operating the laser system in closed loop, a far field as shown in fig. 4.21a has been obtained. The combining efficiency has been determined by truncating it at its first extinction and measuring the power contained in the remaining central lobe. It is given by $P_{\mathrm{ml}} = 87\,\mathrm{W}$, yielding a far field efficiency of $\eta_{\mathrm{FF}} = P_{\mathrm{ml}}/P_{\mathrm{FF}} = 0.49$. In order to obtain the overall combining efficiency η, this value has to be multiplied with the microlens transmission $t_{\mu\text{-lens}}$. In the simulations, $t_{\mu\text{-lens}} = 0.98$ is obtained for our fill factor $\tau_r = 0.7$. In the experiments, only the order of magnitude of this value could be confirmed. This lack in precision is due to the measurement range of our power meter which is inadequate for this task. We thus use the theoretical microlens transmission in order to calculate the overall combining efficiency $\eta = \eta_{\mathrm{FF}} \times t_{\mu\text{-lens}} = 0.48$.

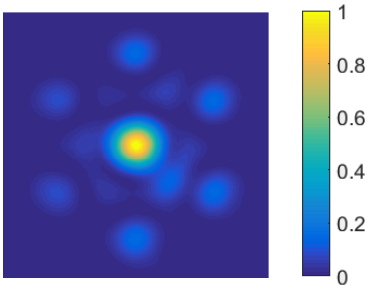

(a) Experimentally obtained far field.

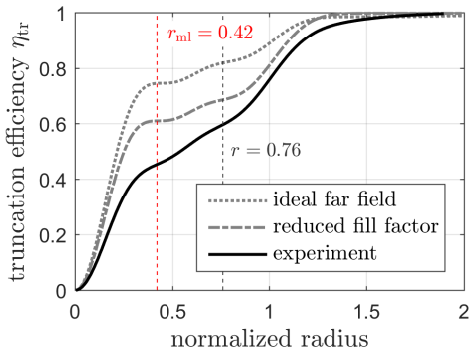

(c) Truncation efficiency of (gray, dotted) an ideal far field, (gray, dashed) a far field with reduced microlens fill factor, and (black, solid) the measured far field.

Figure 4.21: Characterization of the experimental far field.

This corresponds to 71 % of the simulated ideal efficiency of $\eta_{\mathrm{ideal}} = 0.67$, and to 79 % of the maximum possible efficiency for the experimental microlens fill factor, $\eta(\tau_r = 0.7) = 0.61$. This simulated value drops to $\eta_{\mathrm{err}} = 0.56$ when also the alignment errors on the fiber array are considered (see end of section 4.3.2), so that the measured combining efficiency corresponds to 86 % of the theoretical maximum.

The remaining differences between the simulated and the measured efficiencies might be due to errors on the microlens array which have not been considered in the simulations. In particular, the enhanced side lobes of the measured far field (cf. lineouts in fig. 4.22) might be an indication of both a gap between the individual microlenses and a mismatch between the microlens and the fiber array pitch. The supposed gap of $g = 150\,\mu\mathrm{m}$ would cause a decrease of 2.5 percentage points. If the remaining difference between the measured efficiency of $\eta = 0.48$ and the reduced simulated value $\eta'_{\mathrm{err}} = 0.56 - 0.025 = 0.535$ was solely due to a pitch difference between the microlens and the fiber array, this discrepancy would equal $\Delta p = 23\,\mu\mathrm{m}$. Since such a large mismatch between the high precision fiber assembly and the likewise high precision microlens array seems not realistic, other factors impacting the combining efficiency need to be considered.

In particular, the estimation of the spatial alignment errors within the fiber array is not very

accurate, so that the real misalignments might vary from those used in the simulations. This implies that the actual maximum possible efficiency might be inferior to the simulated one, which could partly explain the difference between the simulated and the measured value.

Finally, one needs to consider the impact of the spectral phase on the combining efficiency. As it has been stated in the previous subsection, the residual phase error of $\varphi_i = \lambda/48\,\mathrm{RMS}$ on a single fiber is low enough to avoid efficiency losses due to phase offset differences. The relative delays between the channels have been optimized with respect to the power in the main lobe of the far field. In this process, no changes in transmitted power could be detected over a range of path length differences of about $\pm 10\,\mu\mathrm{m}$. As this within the necessary precision of $\pm 10.5\,\mu\mathrm{m}\,\mathrm{RMS}$ stated in section 3.4.2.2, delay mismatches should not give rise to losses in combining efficiency superior to one percentage point. Finally, mismatches of spectral phase of order two or higher are precluded by the matching of the fiber lengths of all the channels to $\pm 3\,\mathrm{cm}$, as described in section 4.1. In conclusion, it is unlikely that spectral phase mismatches give rise to losses of combining efficiency of more than one percentage point.

From the recorded far field, the truncation efficiency curve shown in fig. 4.21c was calculated. For comparison, also the curves of an ideal far field, and of one with the reduced microlens fill factor $\tau_r = 0.7$ are shown. Clearly, the experimental curve is smoother than the theoretical ones, which indicates less clear extinctions between the different lobes, and a larger amount of power concentrated outside of the main lobe. These characteristics can also be seen in the lineouts of the far fields shown in fig. 4.22, and are due to the misalignments discussed above.

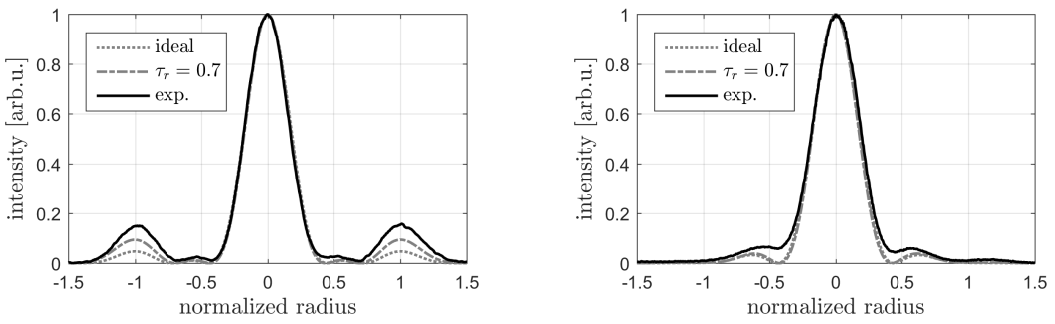

(a) Vertical lineouts.

(b) Horizontal lineouts.

Figure 4.22: Lineouts of (gray, dotted) an ideal far field, (gray, dashed) a far field with reduced microlens fill factor, and (black, solid) the measured far field. The peak intensities of all lineouts are normalized to one.

As indicated in fig. 4.21c, the relative radius of the main lobe for a seven fiber system is $r_{\mathrm{ml}} = 0.42$. Hence, the truncation efficiency $\eta_{\mathrm{tr}}(r_{\mathrm{ml}}) = 0.45$ corresponding to this radius should also correspond to the measured $\eta_{\mathrm{FF}} = 0.48$. For a number of reasons, this is only approximately the case. First and most importantly, the efficiency measurement based on the camera image is highly sensitive to the background noise of the camera and is therefore less accurate than the efficiency calculated from the measured power of the truncated beam. Furthermore, the normalization of the radius of the measured truncation efficiency curve is based on the position of

the side lobes in the far field. Since the measured far field is slightly asymmetric, there are small differences among the radial distances between each side lobe and the center of the main lobe. Hence, the normalization should be performed with respect to the average position of the six side lobes. However, since the precision of the truncation efficiency curve is intrinsically limited by the noise of the camera, it was decided that it would be sufficient to perform the normalization with respect to the average position of the two side lobes of the vertical lineout. Nevertheless, there might be a small discrepancy between this two-side-lobe average radial position and the overall average of the six side lobes, which would give rise to a slight shifting of the truncation efficiency curve. Moreover, different pixel sizes in the experimental and theoretical far field images can lead to slightly different truncation efficiencies for same aperture radii. Finally, it is not sure that the experimental truncation has been performed exactly at the first minimum of the far field. A slight difference between the ideal and the actual size of the main lobe of the far field with respect to the truncating aperture would also result in differences between the measured efficiency and the one deduced from the truncation efficiency curve.

Given all these uncertainties, the experimental truncation efficiency curve shown in fig. 4.21c should not be considered as a precise measurement, but rather as an approximative characterization of the general shape of the far field.

4.5.3 Power Stability

The power stability of the combined beam has been measured by focusing it on a photodiode and recording the power signal over 100 s. The power variations are as low as 1.7 % RMS, and the power noise spectrum obtained from the signal is shown in fig. 4.23. It should be noted that the power fluctuations are not only due to residual phase fluctuations, but are also caused by pointing instabilities of the far field. Such instabilities result in small changes of the position of the far field with respect to the spatial filtering aperture, which leads to small fluctuations in the transmitted power and reduces thus the overall power stability of the combined beam.

As such pointing instabilities can also be observed on a single beam, they are not due to the CBC system, but are rather caused by vibrations in the spatial mode of each individual beam

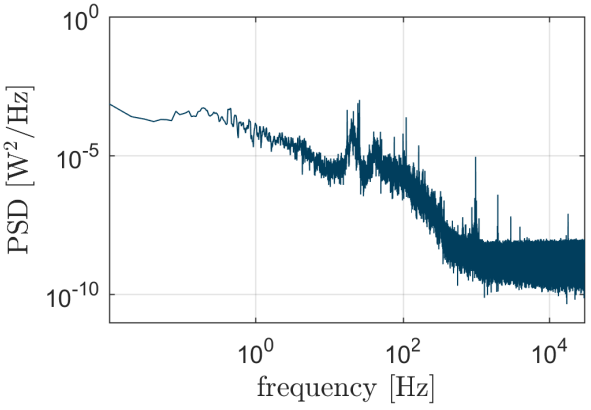

Figure 4.23: Power noise spectrum of the combined beam.

which are transmitted in the combined one. These vibrations can be due to either instabilities in the mode emitted by the fiber amplifiers, or to vibrations in the optomechanics used in the laser back end. Indeed, due to the long overall free space beam path of about 3 m, already minor pointing instabilities can become large enough to impact the power transmitted through the spatial filtering aperture which has a diameter of only 630 µm.

In order to reduce such instabilities, more adequate optomechanics will be used in the 61 fiber setup. Furthermore, the stability of the modes emitted by the fiber amplifiers will be increased by properly coiling them and taping them on breadboards.

4.5.4 Spatial Beam Shape

As described in section 3.1, the shape of the truncated beam highly depends on the relative size of the spatial filtering aperture. This behavior has been observed experimentally for two different aperture sizes, the first corresponding to a truncation at the first extinction at a relative radius of $r = r_{\mathrm{ml}} = 0.42$, and the second to one at the second extinction at $r \approx 0.76$*. For our experimental conditions, this corresponds to aperture diameters of 630 µm and 1.2 mm, respectively. In the following, the spatial characteristics of the truncated beam are described for these two cases.

Tight Filtering

Figure 4.24a shows the position of the filtering aperture in the experimental far field for a truncation at the first extinction. The filtered beam is thus equivalent to the combined beam, and the picture of it shown in fig. 4.24b confirms the neat filtering and the very clean shape of the combined beam. Since this beam is the main lobe of the far field, its shape can be described by an Airy pattern which is clipped at its first zero. The very good agreement between the lineout of the measured far field and the fitted function is shown in fig. 4.25a and confirmed by the correlation coefficient of the two curves which equals $\rho = 0.9999$.

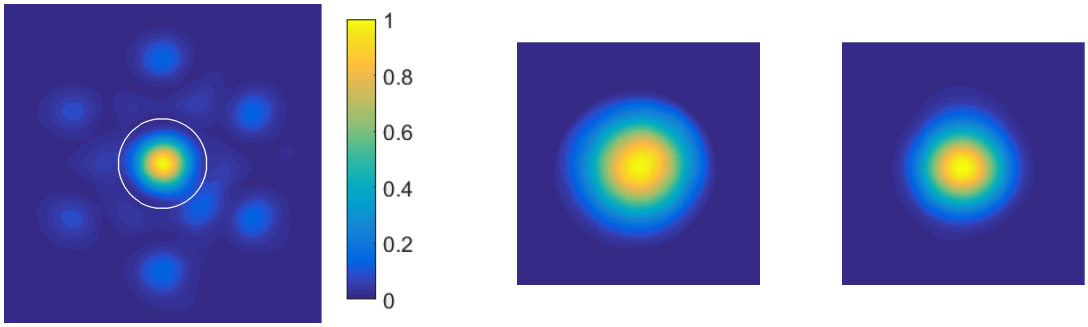

(a) Position of the filtering aperture in the far field.

(b) Truncated far field.

(c) Corresponding recovered near field.

Figure 4.24: Measured fields for spatial filtering at the first extinction.

As explained near the end of section 4.4, the recovered near field has been observed in the image focal plane of a lens. The beam conserves its good spatial properties (see fig. 4.24c), but recovers

*In the seven fiber configuration, the is equivalent to a truncation just before the secondary lobes.

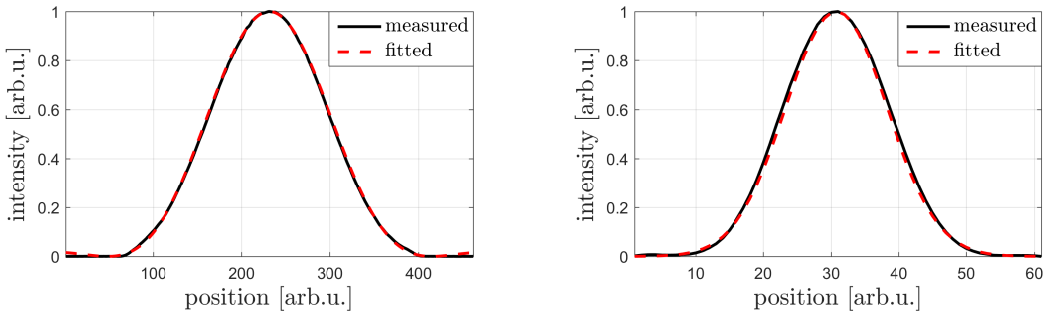

(a) Far field. (b) Recovered near field.

Figure 4.25: Lineouts of the measured (a) far and (b) recovered near field of the combined beam, and fitted (a) Airy and (b) Gaussian functions.

a Gaussian-like shape. Indeed, the lineout in fig. 4.25b shows that the agreement between the measured beam shape and the Gaussian curve is slightly less good than the one obtained in the far field, but still very high. This is confirmed by the correlation coefficient of $\rho = 0.9995$.

The beam quality factor M^2 has been determined by strongly focusing the combined beam and measuring the beam width as a function of distance around the position of the recovered near field. Since the beam shape changes from a truncated Airy pattern to approximately Gaussian, the beam width has been evaluated using the second moment method. The result is shown in fig. 4.26. By fitting the ideal beam width $w(z)$ to the measured curves, both the beam waist w_0 and divergence θ are obtained from this graph. These values allow to calculate the beam quality factor $M^2 = w_0\theta$ for both axes, given by $M_x^2 = M_y^2 = 1.10$. These very good results confirm the high spatial beam quality already claimed above.

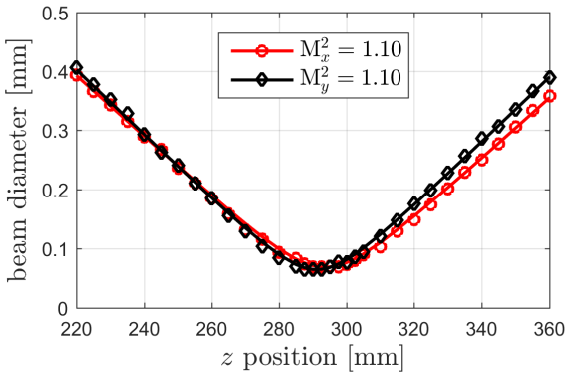

Figure 4.26: Beam diameter as a function of distance, and corresponding M^2-values.

Loose Filtering

A larger filtering aperture of a relative diameter of $r = 0.76$ has been used in order to observe the resulting shape of the truncated beam, and the related truncation efficiency η_{tr}. Based on the curve shown in fig. 4.21c, a value of $\eta_{\mathrm{tr}}(r = 0.76) \approx 0.59$ should be expected. The measured

truncation efficiency $\eta_{\mathrm{tr}} = 0.58$ is in good agreement with this value. Furthermore, it corresponds to 89 % of the efficiency expected from the simulations including alignment errors, and to 71 % of the ideal case.

By comparing these results to the ones obtained by measuring the combining efficiency (in tight filtering configuration), one notices that both measured efficiencies correspond to 71 % of their respective simulated ideal values. This confirms the correct predictions of the simulations. At the same time, η_{tr} measured in loose filtering configuration corresponds to 89 % of the simulated value including alignment errors, whereas the tightly filtered η amounts to only 86 % of the respective simulation. This might indicate that the estimation of the misalignments in the fiber array is somehow imprecise, so that the simulated field does not exactly correspond to the measured one.

As discussed in section 3.1, the larger filtering aperture lets pass higher spatial frequencies, so that the beam partially recovers its initial hexagonal shape in the near field. A simulation of this behavior based on an ideal beam array and the experimental microlens fill factor of $\tau_r = 0.7$ can be found in the upper line of fig. 4.27. The left image shows the complete far field and where it will be truncated (white circle), the middle one illustrates an intermediate step in the beam propagation, and the right image displays the recovered near field.

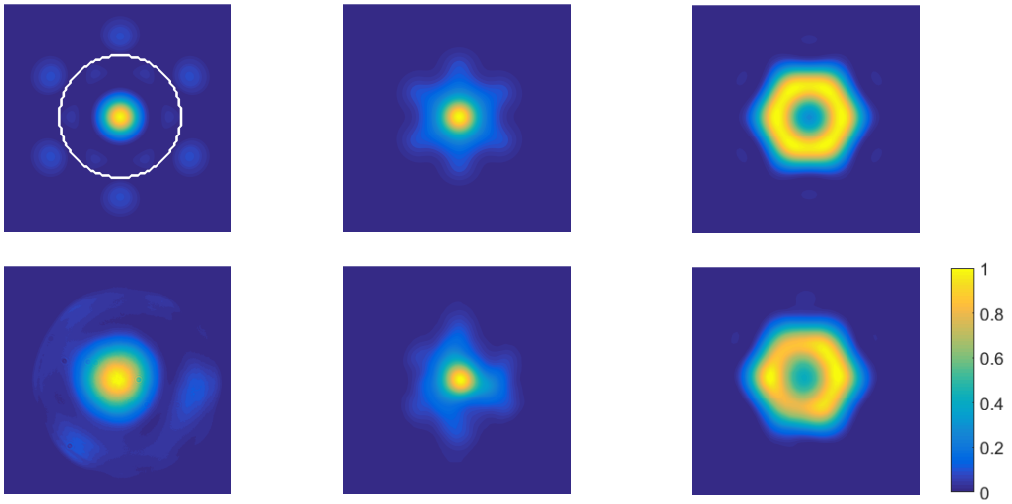

(a) Truncated far field. (b) During beam propagation. (c) Recovered near field.

Figure 4.27: (Top line) Simulation and (bottom line) measurement of the truncated beam (a) in the far field, (b) during beam propagation, and (c) in the recovered near field, for a large filtering aperture.

The lower line of this figure shows the corresponding measured fields. The overall agreement between the simulations and the measurements is quite good, although misalignments in the initial near field lead to distortions in the recovered fields, which are particularly well visible during beam propagation.

These measurements confirm that it is indeed possible to create donut-shaped beams by truncating the far field at its second extinction. Once scaled to higher powers, such beams could be

of interest for certain applications in particle acceleration [75, 76].

4.5.5 Temporal Compression

The tightly filtered combined beam has been temporally compressed and send to an autocorrelator for temporal pulse shape characterization. The resulting autocorrelation trace is shown in fig. 4.28a, where the blue curve shows the measurement and the red curve is a simulated autocorrelation. This latter one has been obtained by Fourier transforming the measured spectrum (cf. fig. 4.28b), and calculating the autocorrelation trace which corresponds to the resulting temporal pulse shape. In this way, also the factor of deconvolution between the autocorrelation and the temporal pulse shape could be determined. Based on the autocorrelation FWHM of 293 fs and the minimum pulse duration of 212 fs derived from the measured spectrum, this factor is given by 1.38. Since the simulated and the measured curve are highly similar, this very factor has been used to determine the pulse duration of the combined beam based on its autocorrelation, yielding a value of $\Delta t = 216\,\mathrm{fs}$. Considering the spectrum with a FWHM of $\Delta\lambda = 8.76\,\mathrm{nm}$, this corresponds to an experimental time-bandwidth product of 0.53. Given that in the simulation one finds a value of 0.52, this result confirms that the compression is almost Fourier transform limited.

The compressed beam has an average power of 71 W, corresponding to a compression efficiency of 82 %.

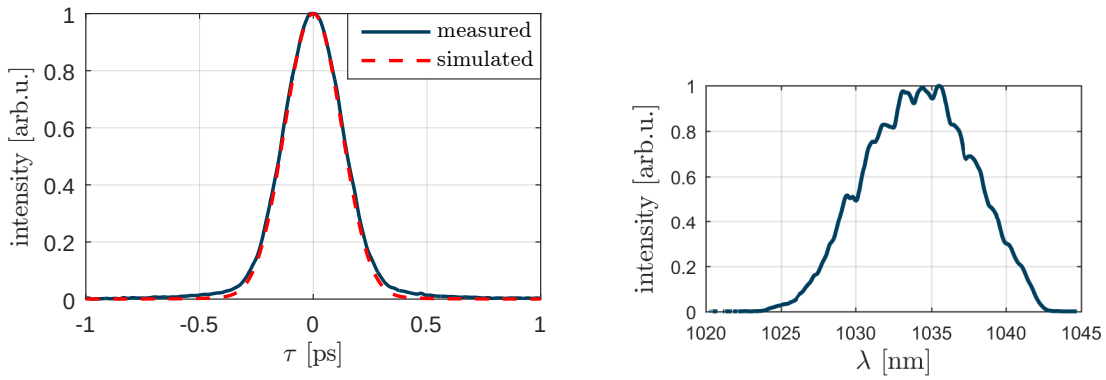

(a) (Blue) measured and (red) simulated autocorrelation trace.

(b) Spectrum of the combined beam.

Figure 4.28: Temporal compression of the combined beam.

4.5.6 Summary

In this section, experimental results obtained with the seven fiber setup operated in linear regime have been presented. In a first step, the quality of the phase locking was checked by measuring the residual phase noise. The result of $\varphi_i = \lambda/48\,\mathrm{RMS}$ on a single fiber is low enough to ensure a stable operation not only in the seven fiber setup, but even in the upscaled version with 61 channels. In a next step, the combining efficiency η was determined. The measured value of

$\eta = 0.48$ corresponds to 71 % of the maximum possible combining efficiency of an ideal far field, and to 86 % of the one simulated by including misalignments in the fiber array. The remaining difference might be due to the inaccuracy in the estimation of the errors in the fiber array, or to errors on the microlens array, such as the gap between the individual lenses.

The combined beam was obtained by spatially filtering the far field at the first extinction next to the main lobe. It exhibits a power stability of 1.7 % RMS, and an excellent spatial beam quality of $M^2 = 1.10$ on both axes. Finally, the temporal compression of the combined beam resulted in an almost Fourier transform limited pulse with a duration of 216 fs.

4.6 Experimental Results in Nonlinear Regime

In order to evaluate the performance of our laser system in the presence of nonlinear effects, it was operated at a constant average power of 25.4 W per fiber, but at reduced pulse repetition rates between 2 MHz and 0.75 MHz, corresponding to B-integrals between approx. 5 rad and 13 rad. Among these values, $B = 5$ rad is the nominal working point of the laser system, and has been chosen since at this level of nonlinearity, a temporally compressed pulse of reasonable quality can be obtained. As this is hardly possible for higher B-integrals, the measurements under these conditions have been taken in order to evaluate the behavior of the CBC system under the impact of large amounts of nonlinear phase.

The results of these measurements are presented in this section. They include the characterization of both the residual phase noise and the combining efficiency for different levels of nonlinearities. Furthermore, we study the power stability and the spatial quality of the combined beam in comparison to the linear regime. Finally, the combined beam was temporally compressed at each pulse repetition rate, revealing the impact of increasing B-integral on the temporal pulse shape.

4.6.1 Residual Phase Noise

The residual phase noise has been measured between different fiber pairs for a pulse repetition rate of 2 MHz and 1 MHz using the same setup as presented in section 4.5.1. An example curve of the resulting phase noise power spectrum is shown in fig. 4.29, in this case recorded between the two topmost fibers of the hexagonal array operated at 2 MHz. Comparing this curve to the one shown in fig. 4.20b, one immediately notices that the open loop phase noise densities are very similar. Hence, the onset of nonlinear effects has no impact on the overall noise present in the system, so that the phase locking algorithm operates under the same conditions as in linear regime. Therefore, differences in the closed loop phase noise densities can be attributed to changing environmental conditions between the measurements. Indeed, the residual phase error of

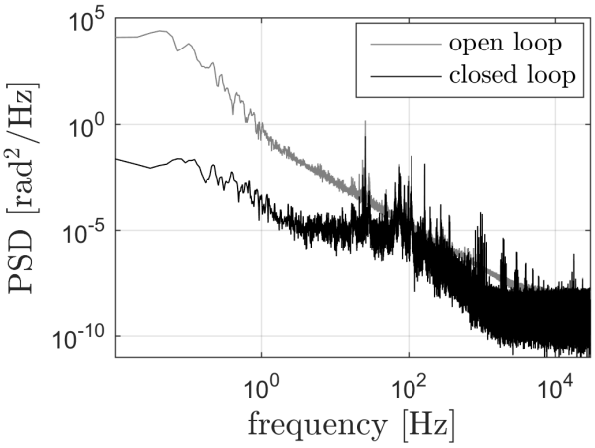

Figure 4.29: Phase noise power spectrum between the two topmost fibers operated at 2 MHz.

$\varphi_{\mathrm{res,NL}} = \lambda/32\,\mathrm{RMS}$ deduced from the curve in fig. 4.29 is almost the same as the $\varphi_{\mathrm{res}} = \lambda/34\,\mathrm{RMS}$ found in linear regime. Similar results are obtained for other fiber pairs and at a pulse repetition rate of 1 MHz. It has thus been concluded that the B-integral has no impact on the performance of the phase locking algorithm.

4.6.2 Combining Efficiency

As for the measurements in linear regime, the system was operated in closed loop and the combining efficiency has been measured by truncating the resulting far fields at their first extinction. These measurements have been performed for the four pulse repetition rates of 2 MHz, 1.5 MHz, 1 MHz and 0.75 MHz. The corresponding far fields are shown in fig. 4.31a, where a far field recorded in linear regime has been included for comparison. It can be seen that the increasing amount of nonlinear effects leads to an increased speckle pattern around the main lobe. In consequence, the combining efficiency decreases, as shown in fig. 4.30.

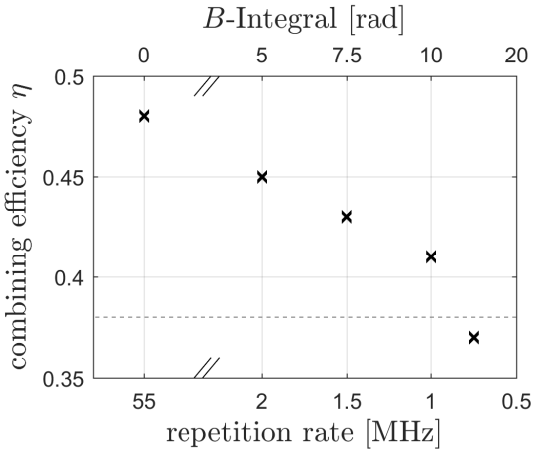

Figure 4.30: Combining efficiencies as a function of pulse repetition rate. The dashed line indicates the theoretical lower limit.

At the working point of 2 MHz, the combining efficiency $\eta = 0.45$ is only three percentage points below the one obtained in linear regime. From the simulations presented in section 3.4.2.2 it can be deduced that this efficiency loss corresponds to B-integral mismatches of $\Delta B = 0.8\,\mathrm{rad}$, which is consistent with the overall B-integral of 5 rad, the specific amplification conditions and the fact that the average output power of the amplifiers has been matched rather than their B-integrals. However, it should be noted that in this nonlinear regime the quality of the matching of the delays between the channels decreases due to the different chirps that the pulses obtain in their respective amplification conditions. Hence, it is highly possible that a certain part of the overall efficiency loss is due to a delay mismatch, and that the differences in B-integral are inferior to the value stated above.

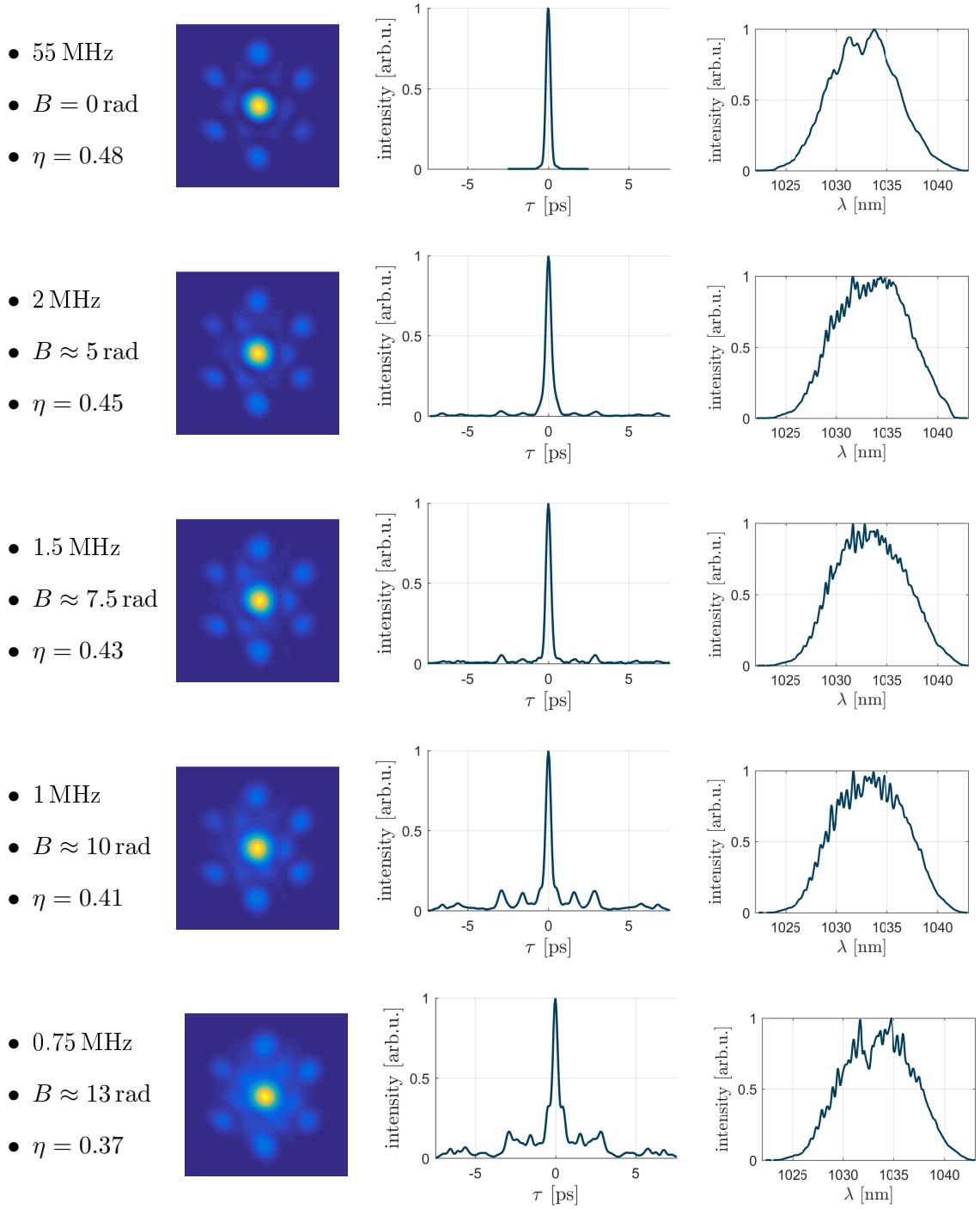

(a) Far fields. (b) Autocorrelation traces. (c) Spectra.

Figure 4.31: Comparison of the main results at increasing levels of nonlinearity. To the left, the different working points and the corresponding measured combining efficiencies η are specified. Next to it, the recorded far fields are represented. The color scale is the same as in the other figures of this chapter. The remaining two columns show the autocorrelation traces and the spectra of the temporally compressed combined beams. An overall decrease in system performance can be observed for increasing B-integrals.

More pronounced drops in combining efficiency occur at very high B-integrals of 10 rad or 13 rad. Indeed, for the latter value, the measured efficiency drops below the theoretical limit deduced in section 3.4.2.1, although the far field (bottom line in fig. 4.31a) still shows the basic structure of one central lobe and six side lobes. This discrepancy is probably due to the fact that the overlap of the individual beams in the far field is not perfect, so that the resulting experimental incoherent efficiency is reduced.

4.6.3 Power Stability

The power stability of the combined beam depends both on its pointing stability and on residual phase fluctuations. The former one is subject to instabilities due to the environmental conditions, as explained in section 4.5.3. It is thus independent of the spectral phase, and remains the same as in linear regime. Furthermore, the phase noise power spectra of the linear and nonlinear regime are very similar both in open and closed loop. Hence, the phase matching algorithm operates under the same conditions, leading to the same quality of phase matching.

In consequence, considering that the two main factors which have an impact on the power stability of the combined beam remain unaffected by the nonlinear effects, it is safe to assume that also the power stability itself does not change with respect to the one observed in linear regime. However, the corresponding measurement could not be performed due to constraints in the schedule of the experiments.

4.6.4 Spatial Beam Shape

As pointed out in section 4.5.4, the spatial shape of the truncated beam depends on the spatial filtering aperture radius. For a tight filtering, only the main lobe of the far field is conserved, so that only very minor parts of the speckle pattern close to it might be transmitted. These could have a slight impact on the spatial beam shape, but are unlikely to lead to major distortions, so that the clean shape of the combined beam is essentially conserved.

In contrast, if a loose filtering was applied, some of the speckle would be conserved. This speckle is due to both the nonlinear phase differences and the spatial alignment errors in the fiber array. These latter ones have already been present in linear regime, and have let to a slight distortion of the experimentally recovered near field (see bottom line of fig. 4.27). In nonlinear regime, the contribution of the nonlinear phase would add up to these distortions, making the near field more arbitrary and therefore less usable for any experiments. Furthermore, as described in section 3.4.2 the spectral content of the truncated beam could become spatially modulated.

At the same time, due to the larger filtering radius the spectral narrowing would be reduced, so that a larger spectrum could be conserved. However, this would not necessarily increase the spectral quality of the truncated beam, since also the larger spectral phases related to the frequencies closer to the edges of the spectrum would be transmitted.

In conclusion, it is probably unadvisable to apply a loose filtering to a beam which exhibits non-negligible amounts of nonlinear phase.

4.6.5 Temporal Compression

As in linear regime, the tightly filtered combined beam has been temporally compressed and characterized with an autocorrelator. It should be emphasized here that the phase of the spatially filtered combined beam corresponds to the mean of the phases of the individual beams. Hence, even if disparities among the nonlinear phases of the individual beams are removed in a CBC setup, the average B-integral is conserved. Hence, for increasing levels of nonlinearity, a degradation in the temporal pulse quality has to be expected. This is indeed the case, as can be seen in the autocorrelation traces of the combined beams at the five different pulse repetition rates shown in fig. 4.31b. Figure 4.31c represents the corresponding spectra, which exhibit oscillating features of increasing intensity, as had to be expected from the increasing secondary pulses in the autocorrelation traces.

At the working point of 2 MHz, the intensity of the secondary pulses remains at a reasonable level, and an autocorrelation FWHM of 350 fs has been measured. The corresponding pulse duration of 253 fs is somewhat larger than in linear regime, where the broadening is due to the nonlinear effects. However, the result remains acceptable.

4.6.6 Summary

In this section, the performances of our laser system have been characterized in nonlinear regime. It was pointed out that neither the spatial quality of the combined beam, nor its phase or power stability change with respect to the linear regime. Furthermore, at the intended working point of 2 MHz or $B \sim 5$ rad, both the combining efficiency and the temporal shape of the compressed beam are somewhat degraded with respect to the linear regime, but remain at reasonable levels. If the repetition rate is further decreased, the degradation increases.

However, the temporal distortion of the combined beam seems to be more detrimental to the overall system performance than the reduced combining efficiency. Hence, the limiting factor in our setup is the temporal compression, just as for any conventional short pulse laser system. Moreover, as the combining efficiencies remain at reasonable levels even for increased amounts of nonlinearities, it could be considered to work at higher B-integrals in order to obtain higher peak powers, at the expense of the temporal pulse quality. Obviously, this is only possible if the presence of pre- or post-pulses can be tolerated.

4.7 Conclusion

In this chapter, the setup and characterization of a tiled aperture CBC system consisting of seven high power fiber amplifiers have been presented. The aim of building this setup was most importantly to confirm the correct operation of all components, and to identify and solve possible problems before scaling the system to 61 fibers. Indeed, it has been observed that it is absolutely indispensable to coil the power amplifiers to a full circle and to implement a good shielding of the whole setup from air flows in order to avoid phase and pointing instabilities in the beams. At the same time, the assembly of a hexagonal fiber array in the laser head by using a simple

fiber stacking approach worked well, and provided precisions close to the ones required in order to avoid losses in combining efficiency. The careful design of a suitable fiber ending allowed to make the fiber insertion process easy and fail-safe.

Once assembled, the laser system was operated both in linear and nonlinear regime. The obtained results are highly satisfying, with combining efficiencies of $\eta = 0.48$ and $\eta = 0.45$, respectively, and very good spatial and spectral beam properties.

The insights gained in these experiments provide valuable information for the design and assembly of the 61 fiber system. Together with the very promising results obtained on the seven fiber setup, they pave the way for a straightforward and fail-safe setup and operation of the upscaled CBC laser system.

5 Conclusion and Outlook

In this thesis, a seven high power fiber amplifier coherent beam combining system in tiled aperture configuration has been presented.

This work has been performed within the scope of the XCAN project, which aims at demonstrating the scalability of CBC setups by implementing an upscaled version of this seven fiber system consisting of 61 amplifiers. Such highly scalable architectures are of particular interest since potential applications such as laser-based particle acceleration would require the coherent combination of up to 10 000 fibers.

It was therefore necessary to identify a system design which could theoretically support such a high number of fibers and still guarantee a good combining efficiency. A review of different architectures and phase matching techniques has shown that a tiled aperture configuration and an interferometric phase measurement method are best suited for this purpose. In such a setup, the beams are arranged in a hexagonal array and collimated with a microlens array to form the initial near field distribution, and the combined beam is given as the main lobe of the corresponding far field. The quality of the beam combining can then be evaluated via the combining efficiency, given as the ratio between the average power contained in the combined beam and the overall average output power of the fiber amplifiers.

It has then been simulated at which point the combining efficiency is sensitive to misalignments in the fiber or the microlens array. It has been shown that a precision on the order of a micrometer is necessary on the lateral alignment of the fibers in order to limit losses in combining efficiency to less than one percentage point below the optimum value. In a similar way, misalignments on the fiber tilts and the focal distances need to be limited to some milliradians and tens of micrometers, respectively. On the microlens array alignment, the requirements are less severe, but still on the order of a few micrometers on the lateral alignment, and only $\sim 0.1\,\mathrm{mm}$ on the focal distance. Most importantly, the rotation of the microlens array with respect to the fiber array needs to be matched to less than $0.2\,\mathrm{mrad}$.

Furthermore, disparities in the spectral properties of the beams have been modeled. It has been shown that especially for low numbers of emitters, the losses in combining efficiency significantly depend on the number of fibers, with higher losses for larger channel numbers. For the case of $N = 61$ fibers, the residual phase error needs to be as low as $\lambda/48\,\mathrm{RMS}$ in order to limit the decrease in combining efficiency to one percentage point. Moreover, the first and second order spectral phase mismatches should not exceed 10 % of the pulse duration or the square of this value, respectively. Last but not least, differences in nonlinear phase should be limited to B-integral discrepancies of $0.32\,\mathrm{rad}$.

These requirements pose high demands on the design of the CBC system. In order to meet

the spatial accuracies stated above, a fiber stacking approach has been implemented, where the fiber endings are slid into high precision ferrules which are stacked into a V-shape holder. This approach yielded the requested precisions on the fiber tilts and focal distances, whereas the errors on the lateral alignment of the fibers are estimated to about 2.6 µm and will give rise to a decrease in combining efficiency of about 4 %.

In the spectral domain, phase differences of second order or higher are corrected for by matching the fiber lengths of all the channels to ±3 cm. Path length differences inferior to this value are adjusted with free space variable optical delay lines within a range of ∼ ±10 µm, which cancels any disparities of the first order spectral phase. The remaining zeroth order is adjusted in real time using piezomechanical fiber stretchers controlled by a phase matching algorithm.

When the system was operated in closed loop, a residual phase error of $\lambda/48$ RMS was measured on a single fiber. Hence, the phase matching algorithm works well enough to avoid losses in combining efficiency even in the upscaled version of our laser system. The combining efficiency was measured to be $\eta = 0.48$, corresponding to 71 % of the efficiency which could be reached in an ideal system, and to 86 % of the maximum efficiency simulated by including the misalignments present in our setup. Furthermore, we measured a power stability of the combined beam of 1.7 % RMS and an M^2 of 1.10 on both axis. Finally, the combined beam was temporally compressed, yielding a nearly Fourier transform limited pulse width of 216 fs, and a time-bandwidth product of 0.53.

In a last series of measurements, we studied the impact of nonlinear effects on the combining efficiency. Indeed, for B-integrals between 5 rad and 13.5 rad, η drops from 0.45 to 0.37. This decrease can be attributed to an increase of the discrepancies among the B-integrals of the different channels, which is a consequence of an increase of nonlinearities. However, at the intended working point of our laser system at $B = 5$ rad, the combining efficiency is only slightly lower than in linear regime, whereas the temporal pulse profile starts to get degraded by the appearance of secondary pulses. Hence, this is the limiting factor of a further increase in peak power of our seven fiber laser setup, just as it is the case for conventional systems.

However, the coherent beam combining architecture allows to overcome this limitation by including additional fiber amplifiers in the beam array. Indeed, the upscaling of the current seven fiber setup to the final 61 fiber amplifier CBC system is an essential part of the XCAN project. In anticipation of this increase in channel number the seven fiber setup has been designed such that it can easily be expanded to host all 61 fibers. The implementation of this upscaled version is currently being realized. First photos taken during the assembly are shown in fig. 5.1.

The immediate next step within the XCAN project will be the finishing of this setup and subsequently its characterization. The main difference between this larger setup and the seven fiber one will be that in the latter case, it was possible to manipulate each individual fiber in order to obtain best results. In the 61 fiber setup, this will not be possible due to the large number of fibers and the inaccessibility of the completely assembled fiber array. It is therefore necessary to perform the initial alignment as carefully as possible in order to minimize alignment errors. Afterwards, no correction of misalignments will be possible, and the system will be characterized by the error distribution present on every parameter.

The finished 61 fiber demonstrator could be involved in different tasks. First, XCAN is part

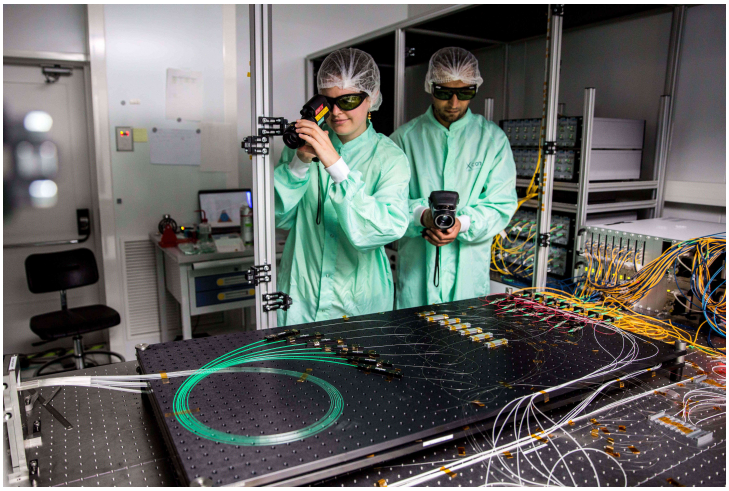

(a) An artist's impression of me and my collegue working on a partially assembled 61 fiber setup.

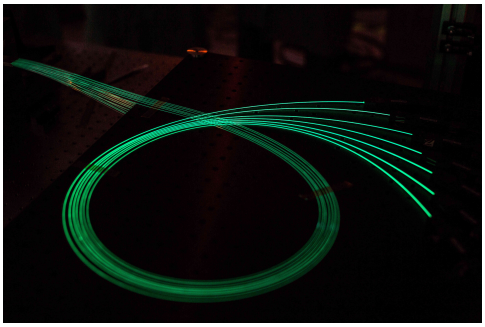

(b) The first 18 fibers in operation.

Figure 5.1: Impressions of the 61 fiber setup.

of the 4F-project ("Filière Française de Fibres optiques pour les lasers de l'industrie du Futur" - French sector of optical fibers for the industrial lasers of the future), which aims at the development of new photonic crystal fibers for use in scientific and industrial applications. As the performance of the XCAN laser system highly depends on the fiber amplifiers in use, it would be instructive to test newly developed fibers in the XCAN setup.

Second, it is intended to implement a post-compression setup at the output of the current laser system. Indeed, reducing the pulse duration from the current $\sim 220\,\mathrm{fs}$ to about $30\,\mathrm{fs}$ or even $3\,\mathrm{fs}$ would adapt the laser system to fields of applications such as high harmonics generation. The post-compression will be performed by passing the compressed laser pulses through a gas-filled capillary, so that the pulse spectrum gets significantly broadened by self-phase modulation. In a subsequent compression stage the accumulated second order spectral phase is removed, so that the pulse duration is reduced close to the new Fourier transform limit. For the post-compression to $3\,\mathrm{fs}$, a stabilization of the carrier-envelope phase of the combined pulses would need to be implemented in order to ensure that the maxima of the carrier wave and the envelope are well synchronized.

Moreover, it is also considered to increase the combining efficiency by implementing one or two phase plates, as has been demonstrated in [73].

A further upscaling of the performances of the laser system is currently not scheduled, but would be easily possible. Measures which could be taken for this purpose involve increasing the number of channels by including additional rings of fibers in the hexagonal array, or by increasing the average output power by adding a second pump diode to each amplifier. Moreover, it could be studied whether it is possible to implement a tiled aperture configuration with rod-type fibers, which could considerably increase both the peak and average powers of the laser system. Finally, new fiber architectures are also investigated in order to enable a backwards pumping scheme in tiled aperture configuration. Due to the close proximity of the fibers in the laser head, this is technically challenging. However, there exist promising approaches which consist in putting small

dichroic mirrors at the output of the amplifiers in order to couple the pump beam in the fiber. An implementation of this technique could reduce the nonlinear effects in the system and thus increase the maximum possible peak powers.

Such an upscaling would approach the system to the requirements imposed by applications such as particle acceleration, and could thus pave the way to a new generation of high peak power and high average power ultrafast laser systems.

Publications

Journal Articles

A. Heilmann, J. Le Dortz, L. Daniault, I. Fsaifes, S. Bellanger, J. Bourderionnet, C. Larat, E. Lallier, M. Antier, E. Durand, C. Simon-Boisson, A. Brignon, and J.-C. Chanteloup. "Coherent beam combining of seven fiber chirped-pulse amplifiers using an interferometric phase measurement". In: *Opt. Express* 26.24 (2018), pp. 31542–31553. DOI: 10.1364/OE.26.031542.

J. Le Dortz, A. Heilmann, M. Antier, J. Bourderionnet, C. Larat, I. Fsaifes, L. Daniault, S. Bellanger, C. Simon-Boisson, J.-C. Chanteloup, E. Lallier, and A. Brignon. "Highly scalable femtosecond coherent beam combining demonstrated with 19 fibers". In: *Opt. Lett.* 42.10 (2017), pp. 1887–1890. DOI: 10.1364/OL.42.001887.

Conferences

A. Heilmann, J. Le Dortz, L. Daniault, I. Fsaifes, S. Bellanger, J. Bourderionnet, C. Larat, E. Lallier, M. Antier, E. Durand, C. Simon-Boisson, A. Brignon, and J.-C. Chanteloup. "Highly Scalable Coherent Beam Combining of Femtosecond Fiber Chirped-Pulse Amplifiers". In: *Laser Congress 2018 (ASSL)*. Optical Society of America, 2018, AM2A.8. DOI: 10.1364/ASSL.2018.AM2A.8.

A. Heilmann, J. Le Dortz, L. Daniault, I. Fsaifes, S. Bellanger, J. Bourderionnet, C. Larat, E. Lallier, M. Antier, E. Durand, C. Simon-Boisson, A. Brignon, and J.-C. Chanteloup. "XCAN: a highly scalable femtosecond coherent amplification network". In: *8th Conference of the International Commitee on Ultrahigh Intensity Lasers*. ICUIL 2018.

A. Heilmann, J. Le Dortz, L. Daniault, I. Fsaifes, S. Bellanger, M. Antier, J. Bourderionnet, E. Durand, C. Simon-Boisson, C. Larat, E. Lallier, A. Brignon, and J.-C. Chanteloup. "Femtosecond coherent beam combining of seven fiber amplifiers in tiled-aperture configuration". In: *8th EPS-QEOD Europhoton Conference*. 2018, paper TuM1.3.

A. Heilmann, J. Le Dortz, S. Bellanger, L. Daniault, I. Fsaifes, M. Antier, J. Bourderionnet, C. Larat, E. Lallier, A. Brignon, E. Durand, C. Simon-Boisson, and J.-C. Chanteloup. "Coherent beam combining of seven femtosecond chirped-pulse fiber amplifiers using an interferometric phase measurement technique". In: *Conference on Lasers and Electro-Optics*. Optical Society of America, 2018, SM2N.8. DOI: 10.1364/CLEO_SI.2018.SM2N.8.

A. Heilmann, J. Le Dortz, L. Daniault, I. Fsaifes, S. Bellanger, M. Antier, A. Brignon, J. Bourderionnet, E. Durand, E. Lallier, C. Larat, C. Simon-Boisson, and J.-C. Chanteloup. "XCAN: a laser program dedicated at exploring Coherent Beam Combination of femtosecond fiber amplifiers". In: *The 3rd International Symposium on High Power Laser Science and Engineering*. HPLSE 2018, paper TuI3–4.

A. Heilmann, J. Le Dortz, L. Daniault, I. Fsaifes, S. Bellanger, M. Antier, A. Brignon, J. Bourderionnet, E. Lallier, C. Larat, C. Simon-Boisson, and J.-C. Chanteloup. "Coherent Beam Combining of Femtosecond Fiber Amplifiers: A Path Towards High Peak and Average Power Lasers". In: *International High Power Laser Ablation*. HPLA 2018.

A. Heilmann, J. Le Dortz, L. Daniault, I. Fsaifes, S. Bellanger, M. Antier, A. Brignon, J. Bourderionnet, E. Lallier, C. Larat, C. Simon-Boisson, and J.-C. Chanteloup. "Femtosecond coherent beam combining of fiber amplifiers". In: *OPTRO-2018*, paper no. 33.

A. Heilmann, J. Le Dortz, L. Daniault, I. Fsaifes, S. Bellanger, M. Antier, J. Bourderionnet, C. Larat, E. Lallier, E. Durand, A. Brignon, C. Simon-Boisson, and J.-C. Chanteloup. "Towards coherent combination of 61 fiber amplifiers". In: *Proc.SPIE*. Vol. 10512. 2018, pp. 10512 – 10512 –6. DOI: 10.1117/12.2287862.

A. Heilmann, J. Le Dortz, S. Bellanger, L. Daniault, I. Fsaifes, M. Antier, J. Bourderionnet, C. Larat, E. Lallier, A. Brignon, C. Simon-Boisson, and J.-C. Chanteloup. "Towards Coherent Combination of 61 Fiber Amplifiers". In: *Laser Congress 2017 (ASSL, LAC)*. Optical Society of America, 2017, JM5A.14. DOI: 10.1364/ASSL.2017.JM5A.14.

J.-C. Chanteloup, A. Heilmann, J. Le Dortz, M. Antier, S. Bellanger, J. Bourderionnet, A. Brignon, L. Daniault, I. Fsaifes, E. Lallier, C. Larat, and C. Simon-Boisson. "XCAN, Ecole Polytechnique-Thales Coherent Beam Combination joint laser program". In: *International Symposium Topical Poblems of Nonlinear Wave Physics*, NWP–2017, plenary talk 8.

J. Le Dortz, A. Heilmann, M. Antier, J. Bourderionnet, C. Larat, I. Fsaifes, L. Daniault, S. Bellanger, C. Simon-Boisson, J.-C. Chanteloup, E. Lallier, and A. Brignon. "Highly scalable femtosecond coherent beam combining". In: *2017 Conference on Lasers and Electro-Optics Europe European Quantum Electronics Conference (CLEO/Europe-EQEC)*. 2017, pp. 1–1. DOI: 10.1109/CLEOE-EQEC.2017.8087022.

J. Le Dortz, A. Heilmann, M. Antier, J. Bourderionnet, C. Larat, I. Fsaifes, L. Daniault, S. Bellanger, C. Simon-Boisson, J.-C. Chanteloup, E. Lallier, and A. Brignon. "Femtosecond coherent beam combining of a large number of fiber amplifiers: first results". In: *SPIE Photonics West*. 2017, Paper 10083–6.

J.-C. Chanteloup, A. Heilmann, J. Le Dortz, M. Antier, S. Bellanger, J. Bourderionnet, A. Brignon, L. Daniault, I. Fsaifes, E. Lallier, C. Larat, and C. Simon-Boisson. "XCAN: A Laser Coherent Beam Combining Project". In: *7th International Commitee on Ultrahigh Intensity Lasers*. ICUIL 2016, paper M–P28.

J. Le Dortz, M. Antier, J. Bourderionnet, C. Larat, A. Heilmann, I. Fsaifes, L. Daniault, S. Bellanger, C. Simon-Boisson, J.-C. Chanteloup, E. Lallier, and A. Brignon. "Coherent beam combining of 19 fibers in femtosecond regime". In: *Lasers Congress 2016 (ASSL, LSC, LAC)*. Optical Society of America, 2016, JTu2A.39. DOI: 10.1364/ASSL.2016.JTu2A.39.

A. Heilmann, J. Le Dortz, S. Bellanger, L. Daniault, I. Fsaifes, J.-C. Chanteloup, M. Antier, A. Brignon, E. Lallier, J. Bourderionnet, C. Larat, and C. Simon-Boisson. "The XCAN project: A Coherent Amplification Network of femtosecond fiber lasers". In: *High Power Laser Systems and Applications*, HPLS&A 2016, paper 9.

M. Antier, J. Le Dortz, J. Bourderionnet, C. Larat, E. Lallier, L. Daniault, I. Fsaifes, A. Heilmann, S. Bellanger, C. Simon-Boisson, J.-C. Chanteloup, and A. Brignon. "XCAN project : coherent beam combining of large number fibers in femtosecond regime (Conference Presentation)". In: *Proc.SPIE*. Vol. 9992. 2016, pp. 9992 –9992 –1. DOI: 10.1117/12.2240473.

J. Le Dortz, A. Heilmann, M. Antier, J. Bourderionnet, C. Larat, E. Lallier, L. Daniault, I. Fsaifes, S. Bellanger, C. Simon-Boisson, J.-C. Chanteloup, and A. Brignon. "Coherent beam combining of 19 fibers in the femtosecond regime". In: *7th EPS-QEOD Europhoton Conference*. 2016, paper FWG–1.3.

J. Le Dortz, M. Antier, J. Bourderionnet, C. Larat, A. Heilmann, I. Fsaifes, L. Daniault, S. Bellanger, C. Simon-Boisson, J.-C. Chanteloup, E. Lallier, and A. Brignon. "Coherent beam combining of 19 fibers in femtosecond regime". In: *Journées Nationales d'Optique Guidée*. JNOG 2016, no 397.

J. Le Dortz, M. Antier, J. Bourderionnet, C. Larat, A. Heilmann, I. Fsaifes, L. Daniault, S. Bellanger, C. Simon-Boisson, J.-C. Chanteloup, E. Lallier, and A. Brignon. "Coherent beam combining of 19 fibers in femtosecond regime". In: *Conference on Lasers and Electro-Optics*. Optical Society of America, 2016, STu1M.1. DOI: 10.1364/CLEO_SI.2016.STu1M.1.

J.-C. Chanteloup, A. Heilmann, J. Le Dortz, L. Daniault, I. Fsaifes, S. Bellanger, M. Antier, A. Brignon, E. Lallier, J. Bourderionnet, C. Larat, and C. Simon-Boisson. "XCAN, a coherent amplification network of femtosecond fiber lasers". In: *The 2nd International Symposium on High Power Laser Science and Engineering*. HPLSE 2016, paper C–22.

J. Le Dortz, M. Antier, J. Bourderionnet, C. Larat, E. Lallier, L. Daniault, S. Bellanger, I. Fsaifes, A. Heilmann, C. Simon-Boisson, J.-C. Chanteloup, and A. Brignon. "Femtosecond coherent beam combination for X-CAN". In: *OPTRO-2016*, paper no. 104.

Bibliography

[1] National Academies of Sciences, Engineering, and Medicine. *Opportunities in Intense Ultrafast Lasers: Reaching for the Brightest Light*. Washington, DC: The National Academies Press, 2018. DOI: 10.17226/24939.

[2] W. Sibbett, A. A. Lagatsky, and C. T. A. Brown. "The development and application of femtosecond laser systems". In: *Opt. Express* 20.7 (2012), pp. 6989–7001. DOI: 10.1364/OE.20.006989.

[3] H. Huang, L.-M. Yang, and J. Liu. "Micro-hole drilling and cutting using femtosecond fiber laser". In: *Optical Engineering* 53 (2014), pp. 53 –53 –9. DOI: 10.1117/1.OE.53.5.051513.

[4] T. M. P. Callou, R. Garcia, A. Mukai, N. Giacomin, R. Souza, and S. Bechara. "Advances in femtosecond laser technology". In: *Clinical Ophtalmology* 10 (2016), pp. 697 –703. DOI: https://doi.org/10.2147/OPTH.S99741.

[5] W. Rudolph, P. Dorn, X. Liu, N. Vretenar, and R. Stock. "Microscopy with femtosecond laser pulses: applications in engineering, physics and biomedicine". In: *Applied Surface Science* 208-209 (2003). Physics and Chemistry of Advanced Laser Materials Processing, pp. 327 –332. DOI: https://doi.org/10.1016/S0169-4332(02)01388-0.

[6] M. Dantus and P. Gross. "Ultrafast Spectroscopy". In: *Encyclopedia of Applied Physics*. Wiley-VCH Verlag GmbH, 1998.

[7] R. Holzwarth, T. Udem, T. W. Hänsch, J. C. Knight, W. J. Wadsworth, and P. S. J. Russell. "Optical Frequency Synthesizer for Precision Spectroscopy". In: *Phys. Rev. Lett.* 85 (11 2000), pp. 2264–2267. DOI: 10.1103/PhysRevLett.85.2264.

[8] P. Salières and M. Lewenstein. "Generation of ultrashort coherent XUV pulses by harmonic conversion of intense laser pulses in gases: towards attosecond pulses". In: *Measurement Science and Technology* 12.11 (2001), p. 1818.

[9] M. Tonouchi. "Cutting-edge terahertz technology". In: *Nature Photonics* 1 (2007). Review Article, 97 EP –.

[10] P. A. Norreys. "Laser-driven particle acceleration". In: *Nature Photonics* 3 (2009), 423 EP –.

[11] U. Linz and J. Alonso. "Laser-driven ion accelerators for tumor therapy revisited". In: *Phys. Rev. Accel. Beams* 19 (12 2016), p. 124802. DOI: 10.1103/PhysRevAccelBeams.19.124802.

[12] R. Soulard, M. N. Quinn, T. Tajima, and G. Mourou. "ICAN: A novel laser architecture for space debris removal". In: *Acta Astronautica* 105.1 (2014), pp. 192 –200. DOI: https://doi.org/10.1016/j.actaastro.2014.09.004.

[13] D. Strickland and G. Mourou. "Compression of amplified chirped optical pulses". In: *Optics Communications* 56.3 (1985), pp. 219 –221. DOI: https://doi.org/10.1016/0030-4018(85)90120-8.

[14] T. Y. Fan. "Laser beam combining for high-power, high-radiance sources". In: *IEEE Journal of Selected Topics in Quantum Electronics* 11.3 (2005), pp. 567–577. DOI: 10.1109/JSTQE.2005.850241.

[15] M. Kienel, M. Müller, A. Klenke, J. Limpert, and A. Tünnermann. "12 mJ kW class ultrafast fiber laser system using multidimensional coherent pulse addition". In: *Opt. Lett.* 41.14 (2016), pp. 3343–3346. DOI: 10.1364/OL.41.003343.

[16] M. Müller, A. Klenke, H. Stark, J. Buldt, T. Gottschall, A. Tünnermann, and J. Limpert. "1.8-kW 16-channel ultrafast fiber laser system". In: *Proc.SPIE* 10512 (2018), pp. 10512 –10512 –6. DOI: 10.1117/12.2287683.

[17] J. Rothhardt, S. Hädrich, Y. Shamir, M. Tschnernajew, R. Klas, A. Hoffmann, G. K. Tadesse, A. Klenke, T. Gottschall, T. Eidam, J. Limpert, A. Tünnermann, R. Boll, C. Bomme, H. Dachraoui, B. Erk, M. D. Fraia, D. A. Horke, T. Kierspel, T. Mullins, A. Przystawik, E. Savelyev, J. Wiese, T. Laarmann, J. Küpper, and D. Rolles. "High-repetition-rate and high-photon-flux 70 eV high-harmonic source for coincidence ion imaging of gas-phase molecules". In: *Opt. Express* 24.16 (2016), pp. 18133–18147. DOI: 10.1364/OE.24.018133.

[18] G. K. Tadesse, W. Eschen, R. Klas, V. Hilbert, D. Schelle, A. Nathanael, M. Zilk, M. Steinert, F. Schrempel, T. Pertsch, A. Tünnermann, J. Limpert, and J. Rothhardt. "High resolution XUV Fourier transform holography on a table top". In: *Scientific Reports* 8.1 (2018), p. 8677. DOI: 10.1038/s41598-018-27030-y.

[19] G. Mourou, B. Brocklesby, T. Tajima, and J. Limpert. "The future is fibre accelerators". In: *Nature Photonics* 7 (2013). DOI: 10.1038/nphoton.2013.75.

[20] M. Antier, J. Bourderionnet, C. Larat, E. Lallier, E. Lenormand, J. Primot, and A. Brignon. "kHz Closed Loop Interferometric Technique for Coherent Fiber Beam Combining". In: *IEEE Journal of Selected Topics in Quantum Electronics* 20.5 (2014), pp. 182–187. DOI: 10.1109/JSTQE.2014.2302444.

[21] J. Le Dortz, A. Heilmann, M. Antier, J. Bourderionnet, C. Larat, I. Fsaifes, L. Daniault, S. Bellanger, C. Simon-Boisson, J.-C. Chanteloup, E. Lallier, and A. Brignon. "Highly scalable femtosecond coherent beam combining demonstrated with 19 fibers". In: *Opt. Lett.* 42.10 (2017), pp. 1887–1890. DOI: 10.1364/OL.42.001887.

[22] B. E. A. Saleh and M. C. Teich. *Fundamentals of Photonics*. John Wiley & Sons, Inc, 1991.

[23] F. Träger, ed. *Springer Handbook of Lasers and Optics*. Springer Science + Business Media, LLC New York, 2007.

[24] J. D. McMullen. "Chirped-pulse compression in strongly dispersive media*". In: *J. Opt. Soc. Am.* 67.11 (1977), pp. 1575–1578. DOI: 10.1364/JOSA.67.001575.

[25] G. P. Agrawal. *Nonlinear Fiber Optics*. 4th ed. Academic Press, 2007.

[26] R. W. Boyd. *Nonlinear Optics*. 3rd ed. Academic Press, 2007.

[27] D. N. Schimpf, E. Seise, J. Limpert, and A. Tünnermann. "The impact of spectral modulations on the contrast of pulses of nonlinear chirped-pulse amplification systems". In: *Opt. Express* 16.14 (2008), pp. 10664–10674. DOI: 10.1364/OE.16.010664.

[28] https://www.thorlabs.com/tutorials.cfm?tabID=789B6970-20AC-47C3-81A9-838CD7594644. July 2018.

[29] Polarization Maintaining 980 nm Telecommunication Fibers. *Datasheet*. Nufern, 2015.

[30] L. Thévanaz, ed. *Advanced Fiber Optics. Concepts and Technology*. 1st ed. EPFL Press, 2011.

[31] https://www.fiberlabs-inc.com/glossary/fiber-laser/. July 2018.

[32] J. Limpert, F. Stutzki, F. Jansen, H.-J. Otto, T. Eidam, C. Jauregui, and A. Tünnermann. "Yb-doped large-pitch fibres: effective single-mode operation based on higher-order mode delocalisation". In: *Light: Science & Applications* 1 (2012).

[33] P. Russell. "Photonic Crystal Fibers". In: *Science* 299.5605 (2003), pp. 358–362. DOI: 10.1126/science.1079280.

[34] T. A. Birks, J. C. Knight, and P. S. J. Russell. "Endlessly single-mode photonic crystal fiber". In: *Opt. Lett.* 22.13 (1997), pp. 961–963. DOI: 10.1364/OL.22.000961.

[35] J. Limpert, A. Liem, M. Reich, T. Schreiber, S. Nolte, H. Zellmer, A. Tünnermann, J. Broeng, A. Petersson, and C. Jakobsen. "Low-nonlinearity single-transverse-mode ytterbium-doped photonic crystal fiber amplifier". In: *Opt. Express* 12.7 (2004), pp. 1313–1319. DOI: 10.1364/OPEX.12.001313.

[36] Modal properties of the DC-200/40-PZ-Yb LMA fiber. *Whitepaper*. NKT Photonics, 2013.

[37] K. Saitoh and S. Matsuo. "Multicore Fiber Technology". In: *J. Lightwave Technol.* 34.1 (2016), pp. 55–66.

[38] L. P. Ramirez, M. Hanna, G. Bouwmans, H. E. Hamzaoui, M. Bouazaoui, D. Labat, K. Delplace, J. Pouysegur, F. Guichard, P. Rigaud, V. Kermène, A. Desfarges-Berthelemot, A. Barthélémy, F. Prévost, L. Lombard, Y. Zaouter, F. Druon, and P. Georges. "Coherent beam combining with an ultrafast multicore Yb-doped fiber amplifier". In: *Opt. Express* 23.5 (2015), pp. 5406–5416. DOI: 10.1364/OE.23.005406.

[39] S. Jain, C. Castro, Y. Jung, J. Hayes, R. Sandoghchi, T. Mizuno, Y. Sasaki, Y. Amma, Y. Miyamoto, M. Bohn, K. Pulverer, M. Nooruzzaman, T. Morioka, S. Alam, and D. J. Richardson. "32-core erbium/ytterbium-doped multicore fiber amplifier for next generation space-division multiplexed transmission system". In: *Opt. Express* 25.26 (2017), pp. 32887–32896. DOI: 10.1364/OE.25.032887.

[40] https://www.thorlabs.com/newgrouppage9.cfm?objectgroup_id=1785. July 2018.

[41] R. Paschotta, J. Nilsson, A. C. Tropper, and D. C. Hanna. "Ytterbium-doped fiber amplifiers". In: *IEEE Journal of Quantum Electronics* 33.7 (1997), pp. 1049–1056. DOI: 10.1109/3.594865.

[42] E. Desurvire. *Erbium-doped fiber amplifiers. Principles and applications.* John Wiley & Sons, Inc, 2002.

[43] P. Parvin, M. Ilchi-Ghazaani, A. Bananej, and Z. Lali-Dastjerdi. "Small signal gain and saturation intensity of a Yb:Silica fiber MOPA system". In: *Optics & Laser Technology* 41.7 (2009), pp. 885 –891. DOI: https://doi.org/10.1016/j.optlastec.2009.02.006.

[44] E. Desurvire. "Analysis of gain difference between forward- and backward-pumped erbium-doped fiber amplifiers in the saturation regime". In: *IEEE Photonics Technology Letters* 4.7 (1992), pp. 711–714. DOI: 10.1109/68.145247.

[45] T. Eidam, C. Wirth, C. Jauregui, F. Stutzki, F. Jansen, H.-J. Otto, O. Schmidt, T. Schreiber, J. Limpert, and A. Tünnermann. "Experimental observations of the threshold-like onset of mode instabilities in high power fiber amplifiers". In: *Opt. Express* 19.14 (2011), pp. 13218–13224. DOI: 10.1364/OE.19.013218.

[46] C. Manzoni, O. D. Mücke, G. Cirmi, S. Fang, J. Moses, S.-W. Huang, K.-H. Hong, G. Cerullo, and F. X. Kärtner. "Coherent pulse synthesis: towards sub-cycle optical waveforms". In: *Laser & Photonics Reviews* 9.2 (2015), pp. 129–171. DOI: 10.1002/lpor.201400181.

[47] V. Leshchenko, V. Vasiliev, N. Kvashnin, and E. Pestryakov. "Coherent combining of relativistic-intensity femtosecond laser pulses". In: *Applied Physics B* 118 (Mar. 2015). DOI: 10.1007/s00340-015-6047-7.

[48] A. Brignon, ed. *Coherent Laser Beam Combining*. Wiley-VCH Verlag GmbH & Co. KGaA, 2013.

[49] G. D. Goodno, C.-C. Shih, and J. E. Rothenberg. "Perturbative analysis of coherent combining efficiency with mismatched lasers". In: *Opt. Express* 18.24 (2010), pp. 25403–25414. DOI: 10.1364/OE.18.025403.

[50] V. E. Leshchenko. "Coherent combining efficiency in tiled and filled aperture approaches". In: *Opt. Express* 23.12 (2015), pp. 15944–15970. DOI: 10.1364/OE.23.015944.

[51] A. Klenke. "Performance scaling of laser amplifiers via coherent combination of ultrashort pulses". PhD thesis. Friedrich-Schiller-Universität Jena, Jan. 2016.

[52] L. Daniault, M. Hanna, L. Lombard, Y. Zaouter, E. Mottay, D. Goular, P. Bourdon, F. Druon, and P. Georges. "Coherent beam combining of two femtosecond fiber chirped-pulse amplifiers". In: *Opt. Lett.* 36.5 (2011), pp. 621–623. DOI: 10.1364/OL.36.000621.

[53] M. Müller, M. Kienel, A. Klenke, T. Gottschall, E. Shestaev, M. Plötner, J. Limpert, and A. Tünnermann. "1 kW 1 mJ eight-channel ultrafast fiber laser". In: *Opt. Lett.* 41.15 (2016), pp. 3439–3442. DOI: 10.1364/OL.41.003439.

[54] T. Zhou, Q. Du, T. Sano, R. Wilcox, and W. Leemans. "Two-dimensional combination of eight ultrashort pulsed beams using a diffractive optic pair". In: *Opt. Lett.* 43.14 (2018), pp. 3269–3272. DOI: 10.1364/OL.43.003269.

[55] T. Zhou, T. Sano, and R. Wilcox. "Coherent combination of ultrashort pulse beams using two diffractive optics". In: *Opt. Lett.* 42.21 (2017), pp. 4422–4425. DOI: 10.1364/OL.42.004422.

[56] J. Bourderionnet, C. Bellanger, J. Primot, and A. Brignon. "Collective coherent phase combining of 64 fibers". In: *Opt. Express* 19.18 (2011), pp. 17053–17058. DOI: 10.1364/OE.19.017053.

[57] M. Kienel, A. Klenke, T. Eidam, S. Hädrich, J. Limpert, and A. Tünnermann. "Energy scaling of femtosecond amplifiers using actively controlled divided-pulse amplification". In: *Opt. Lett.* 39.4 (2014), pp. 1049–1052. DOI: 10.1364/OL.39.001049.

[58] S. Zhou, F. W. Wise, and D. G. Ouzounov. "Divided-pulse amplification of ultrashort pulses". In: *Opt. Lett.* 32.7 (2007), pp. 871–873. DOI: 10.1364/OL.32.000871.

[59] Y. Zaouter, F. Guichard, L. Daniault, M. Hanna, F. Morin, C. Hönninger, E. Mottay, F. Druon, and P. Georges. "Femtosecond fiber chirped- and divided-pulse amplification system". In: *Opt. Lett.* 38.2 (2013), pp. 106–108. DOI: 10.1364/OL.38.000106.

[60] T. Zhou, J. Ruppe, C. Zhu, I.-N. Hu, J. Nees, and A. Galvanauskas. "Coherent pulse stacking amplification using low-finesse Gires-Tournois interferometers". In: *Opt. Express* 23.6 (2015), pp. 7442–7462. DOI: 10.1364/OE.23.007442.

[61] H. Pei, J. Ruppe, S. Chen, M. Sheikhsofla, J. Nees, Y. Yang, R. Wilcox, W. Leemans, and A. Galvanauskas. "Near-complete stored energy extraction from fiber amplifiers in ultrashort >10mJ energy pulses using coherent pulse stacking amplification (Conference Presentation)". In: *Proc.SPIE* 10512 (2018). DOI: 10.1117/12.2291303.

[62] M. Hanna, F. Guichard, Y. Zaouter, D. N. Papadopoulos, F. Druon, and P. Georges. "Coherent combination of ultrafast fiber amplifiers". In: *Journal of Physics B: Atomic, Molecular and Optical Physics* 49.6 (2016), p. 062004.

[63] S. J. Augst, T. Y. Fan, and A. Sanchez. "Coherent beam combining and phase noise measurements of ytterbium fiber amplifiers". In: *Opt. Lett.* 29.5 (2004), pp. 474–476. DOI: 10.1364/OL.29.000474.

[64] L. Daniault, M. Hanna, D. N. Papadopoulos, Y. Zaouter, E. Mottay, F. Druon, and P. Georges. "Passive coherent beam combining of two femtosecond fiber chirped-pulse amplifiers". In: *Opt. Lett.* 36.20 (2011), pp. 4023–4025. DOI: 10.1364/OL.36.004023.

[65] H. K. Ahn and H. J. Kong. "Cascaded multi-dithering theory for coherent beam combining of multiplexed beam elements". In: *Opt. Express* 23.9 (2015), pp. 12407–12413. DOI: 10.1364/OE.23.012407.

[66] A. Klenke, M. Müller, H. Stark, A. Tünnermann, and J. Limpert. "Sequential phase locking scheme for a filled aperture intensity coherent combination of beam arrays". In: *Opt. Express* 26.9 (2018), pp. 12072–12080. DOI: 10.1364/OE.26.012072.

[67] D. Kabeya, V. Kermène, M. Fabert, J. Benoist, A. Desfarges-Berthelemot, and A. Barthélémy. "Active coherent combining of laser beam arrays by means of phase-intensity mapping in an optimization loop". In: *Opt. Express* 23.24 (2015), pp. 31059–31068. DOI: 10.1364/OE.23.031059.

[68] D. Kabeya, V. Kermène, M. Fabert, J. Benoist, J. Saucourt, A. Desfarges-Berthelemot, and A. Barthélémy. "Efficient phase-locking of 37 fiber amplifiers by phase-intensity mapping in an optimization loop". In: *Opt. Express* 25.12 (2017), pp. 13816–13821. DOI: 10.1364/OE.25.013816.

[69] C. Bellanger, B. Toulon, J. Primot, L. Lombard, J. Bourderionnet, and A. Brignon. "Collective phase measurement of an array of fiber lasers by quadriwave lateral shearing interferometry for coherent beam combining". In: *Opt. Lett.* 35.23 (2010), pp. 3931–3933. DOI: 10.1364/OL.35.003931.

[70] F. Prevost, L. Lombard, J. Primot, L. P. Ramirez, L. Bigot, G. Bouwmans, and M. Hanna. "Coherent beam combining of a narrow-linewidth long-pulse Er3+-doped multicore fiber amplifier". In: *Opt. Express* 25.9 (2017), pp. 9528–9534. DOI: 10.1364/OE.25.009528.

[71] C. Bellanger, A. Brignon, B. Toulon, J. Primot, F. Bouamrane, T. Bouvet, S. Megtert, L. Quetel, and T. Allain. "Design of a fiber-collimated array for beam combining". In: *Optical Engineering* 50 (2011), pp. 50 –50 –7. DOI: 10.1117/1.3537968.

[72] M. Antier-Murgey. "Mesure interférométrique de phase et application à la combinaison cohérente d'un grand nombre de fibres amplificatrices." PhD thesis. Université Paris Sud - Paris XI, Nov. 2014.

[73] J. L. Dortz. "Mise en phase active de fibres laser en régime femtoseconde par méthode interférométrique". PhD thesis. Université Paris-Saclay, Sept. 2018.

[74] Y. Cui, Y.-Q. Gao, Z.-X. Zhao, Z.-Y. Xu, N. An, D.-W. Li, J.-W. Yu, T. Wang, G. Xu, W.-X. Ma, and Y.-P. Dai. "Spectral phase effects and control requirements of coherent beam combining for ultrashort ultrahigh intensity laser systems". In: *Appl. Opt.* 55.35 (2016), pp. 10124–10132. DOI: 10.1364/AO.55.010124.

[75] C. Brabetz, S. Busold, T. Cowan, O. Deppert, D. Jahn, O. Kester, M. Roth, D. Schumacher, and V. Bagnoud. "Laser-driven ion acceleration with hollow laser beams". In: *Physics of Plasmas* 22.1 (2015), p. 013105. DOI: 10.1063/1.4905638.

[76] J. Vieira and J. T. Mendonça. "Nonlinear Laser Driven Donut Wakefields for Positron and Electron Acceleration". In: *Phys. Rev. Lett.* 112 (21 2014), p. 215001. DOI: 10.1103/PhysRevLett.112.215001.

Résumé de la thèse en français

Architecture évolutive de combinaison cohérente femtoseconde pour amplificateurs à fibre de puissance

Les lasers ultrarapides de haute puissance sont utilisés dans des domaines variés tels que les sciences fondamentales, l'industrie ou le médical. Pourtant, certaines applications, comme l'accélération de particules, restent aujourd'hui inaccessibles car l'état de l'art actuel des systèmes lasers femtoseconde ne permet pas d'allier à la fois les hautes puissances moyennes et crêtes requises par ces applications. Tandis que les lasers Ti:Sa sont bien adaptés aux hautes puissances crêtes, leurs puissances moyennes restent limitées par les effets thermiques. En revanche, les amplificateurs à fibre sont capables de délivrer de hautes puissances moyennes grâce au rapport élevé entre leur surface refroidie et leur volume amplificateur. Par contre, leurs puissances crêtes sont limitées par des effets non-linéaires qui dégradent les qualités spectrales des impulsions et peuvent dans le pire des cas endommager la fibre.

Plusieurs techniques sont couramment utilisées pour contourner ces effets. D'une part, il est possible de diminuer l'intensité dans l'amplificateur par l'utilisation de fibres à large aire modale. D'autre part, l'amplification à dérive de fréquence permet d'étirer temporellement l'impulsion avant l'amplification, ce qui réduit sa puissance crête et, par conséquent, les effets non-linéaires qui lui sont proportionnels. Néanmoins, ces deux techniques atteignent leurs limites en termes d'augmentation de la puissance crête des impulsions ultracourtes.

Il apparaît donc nécessaire d'explorer de nouveaux concepts pour augmenter les puissances crêtes des systèmes lasers à fibre. Une méthode ayant déjà fait ses preuves est la combinaison cohérente de faisceaux. Avec cette technique, un faisceau est séparé spatialement en N sous-faisceaux avant amplification, puis recombiné de façon cohérente à haute puissance. Pour que cette recombinaison soit efficace, il est indispensable que toutes les caractéristiques spectrales et spatiales des faisceaux à combiner soient parfaitement en accord. Il est ainsi possible d'augmenter simultanément la puissance crête et la puissance moyenne d'un facteur N, tandis que les effets non-linéaires et thermiques restent à un niveau constant.

Etant donné que des applications comme l'accélération de particules nécessiteraient la combinaison cohérente d'environ 10 000 fibres, il est nécessaire d'étudier des architectures de combinaison extrapolables à un très grand nombre de faisceaux. Dans le cadre du projet XCAN, une telle architecture a été identifiée et, dans un premier temps, implémentée en utilisant 19 fibres non amplificatrices. Ensuite, un prototype comprenant sept fibres actives a été mis en place afin d'étudier l'impact de l'amplification sur la combinaison cohérente. La dernière étape consistera en l'assemblage d'un démonstrateur de 61 fibres amplificatrices qui illustrera le potentiel de mise à l'échelle

du système.

Les travaux de cette thèse s'inscrivent dans le cadre du deuxième point du projet, c'est-à-dire l'assemblage et la caractérisation du prototype à sept fibres amplificatrices. En premier lieu, des simulations ont été effectuées afin d'évaluer les désaccords entre les faisceaux qui peuvent être tolérés sans entraîner une dégradation importante de l'efficacité de combinaison. Ces résultats ont permis de définir notamment les contraintes spatiales et spectrales à imposer au système expérimental.

Celui-ci a ensuite été caractérisé. L'erreur résiduelle de phase sur une fibre individuelle est inférieure à $\lambda/38$, ce qui indique une très bonne stabilité en phase. Une efficacité de combinaison de 48 % a été mesurée en régime linéaire, ce qui correspond à 86 % de ce qui est théoriquement accessible compte tenu des défauts de l'assemblage expérimental. De plus, une excellente qualité spatiale du faisceau recombiné a été mesurée, avec $M^2 = 1.10$ sur les deux axes. Finalement, l'impulsion combinée a été comprimée à une durée temporelle de 216 fs, ce qui est très proche de la limite par transformée de Fourier. En régime non-linéaire, les distorsions engendrées sur les sept faisceaux n'ont qu'un impact modéré sur l'efficacité de combinaison (qui se réduit à 45 % à un intégral B de 5 rad), démontrant la robustesse du système dans des conditions moins favorables à haute énergie.

En conclusion, les résultats présentés ci-dessus montrent que le système de combinaison cohérente auparavant implémenté avec 19 fibres passives est bien adapté au fonctionnement en régime actif. Le dispositif conçu, mis en place et caractérisé dans le cadre de cette thèse a donc parfaitement rempli son rôle de prototype exploratoire et est maintenant prêt à accueillir 61 fibres, ouvrant ainsi la voie à une nouvelle génération de lasers à hautes puissances crête et moyenne.

Titre : Architecture évolutive de combinaison cohérente femtoseconde pour amplificateurs à fibre de puissance

Mots clés : Combinaison cohérente de faisceaux, lasers femtoseconde, amplificateurs à fibre

Résumé : Allier de fortes puissances moyennes et crêtes donne accès à un champ applicatif très large pour un système laser ultrarapide. Une technique qui s'est avérée capable de satisfaire ces exigences est la combinaison cohérente de faisceaux (CBC). Elle permet de séparer spatialement les faisceaux avant l'amplification pour les recombiner ensuite d'une manière cohérente en un unique faisceau. Afin d'obtenir une recombinaison efficace, les propriétés spatiales et spectrales de tous les faisceaux doivent être parfaitement en accord.
Pour des applications comme l'accélération de particules, le recours à plusieurs milliers de fibres doit être envisagé. Il est donc nécessaire d'étudier des architectures CBC fortement évolutives en termes de canaux amplificateurs.
Le projet XCAN vise à une première démonstration d'un tel système en réalisant la combinaison cohérente de 61 fibres amplificatrices. Afin d'étudier les défis scientifiques et techniques d'une telle architecture, une version de taille réduite comprenant sept fibres a été mise en place.
La conception et la réalisation de ce prototype sont le sujet de cette thèse.
Dans un premier temps, des simulations ont été effectués afin d'estimer les désaccords tolérables entre les propriétés spatiales et spectrales des différents faisceaux.
Basé sur ce travail de modélisation, un système laser de combinaison cohérente de sept fibres a été ensuite assemblé et caractérisé. Les résultats obtenus sont très prometteurs et montrent que notre architecture est bien adaptée pour accueillir les 61 fibres du démonstrateur final XCAN.

Title : Highly Scalable Femtosecond Coherent Beam Combining System of High Power Fiber Amplifiers

Keywords : Coherent beam combining, femtosecond lasers, fiber amplifiers

Abstract : Future applications of high power ultrafast laser systems require simultaneously high average and peak powers. A technique which has proved to be capable of meeting these demands is coherent beam combining (CBC).
In this technique, the beam is spatially split prior to amplification, and coherently recombined in one single beam afterwards. In order to achieve an efficient recombination, the spatial and spectral properties of all beams need to be perfectly matched.
For applications such as particle acceleration, the coherent combining of several thousands of fibers needs to be considered. It is thus necessary to investigate highly scalable CBC architectures.
The XCAN project aims at a first demonstration of such a scalable setup by coherently combining 61 fiber amplifiers. In order to study the scientific and technical challenges of such a system, a downscaled version consisting of seven fibers has been implemented.
The design and characterization of this prototype is the subject of this thesis.
As a starting point, numerical simulations have been performed in order to estimate the maximum tolerable mismatches between the spatial and spectral properties of the beams.
Based on this modeling work, a seven fiber CBC system has been assembled and characterized. The obtained results are very promising and imply that our setup is well suited for the accommodation of all 61 fibers of the final XCAN demonstrator.